INTERNATIONAL JOURNAL OF
NUMERICAL ANALYSIS AND MODELING
Volume 20, Number 2, Pages 267–312

doi: 10.4208/ijnam2023-1011

MONOLITHIC AND PARTITIONED FINITE ELEMENT SCHEMES FOR FSI BASED ON AN ALE DIVERGENCE-FREE HDG FLUID SOLVER AND A TDNNS STRUCTURAL SOLVER

GUOSHENG FU

Abstract. We present novel (high-order) finite element schemes for the fluid-structure interaction (FSI) problem based on an arbitrary Lagrangian-Eulerian divergence-free hybridizable discontinuous Gakerkin (ALE divergence-free HDG) incompressible flow solver, a Tangential-Displacement-Normal-Normal-Stress (TDNNS) nonlinear elasticity solver, and a generalized Robin interface condition treatment. Temporal discretization is performed using the high-order backward difference formulas (BDFs). Both monolithic and strongly coupled partitioned fully discrete schemes are obtained. Numerical convergence studies are performed for the flow and elasticity solvers, and the coupled FSI solver, which verify the high-order space-time convergence of the proposed schemes. Numerical results on classical two dimensional benchmark problems also showed good performance of our proposed methods.

Key words. Divergence-free HDG, ALE, FSI, TDNNS, generalized Robin condition, partitioned scheme.

1. Introduction

Fluid-structure interaction (FSI) describes a multi-physics phenomenon that involves the highly non-linear coupling between a deformable or moving structure and a surrounding or internal fluid. There has been intensive interest in numerically solving FSI problems due to its wide applications in biomedical, engineering and architecture fields [18, 32, 48].

Based on different temporal discretization strategies, the numerical procedure to solve FSI problems can be broadly classified into two approaches, see, e.g., [76]: the *monolithic approach* and the *partitioned approach*. The monolithic approach [5, 40, 49, 65, 73, 95] solves for the fluid flow and structural dynamics simultaneously by a unified algorithm. Since the interfacial conditions are *automatically* satisfied in the solution procedure, monolithic schemes allow for more rigorous analysis of discretization and solution techniques, and are usually more robust than partitioned schemes. On the other hand, the partitioned approach [30, 34, 66] gains computational efficiency over the monolithic approach by solving the fluid and structure sub-problems separately in a sequential manner, usually with the help of a proper *explicit* coupling condition on the fluid-structure interface to separate the fluid and structure solvers. But the design of efficient partitioned schemes that produce stable and accurate results remains a challenge, especially when the fluid and structure have comparable densities, as it happens in hemodynamic applications, due to numerical instabilities known as *the added mass effect* [17]. The design and analysis of partitioned numerical methods that address the added mass effect remains an active research area in the past decade, see, e.g., [1, 3, 4, 10, 14, 39] and references cited therein.

The finite element method is one of the most popular choices for the numerical simulation of FSI problems [6, 11, 12, 86]. Of particular relevance to the current

Received by the editors July 19, 2022 and, in revised form, November 19, 2022.
1991 *Mathematics Subject Classification.* 65N30, 65N12, 76S05, 76D07.

contribution is the class of discontinuous Galerkin (DG) finite element schemes, which has gained increased interest in the computational fluid dynamics community [21,27,29] due to their distinctive features, such as the ability to achieve high-order accuracy on complex geometries using unstructured meshes and meshes with general polygonal/polyhedral elements, the flexibility in performing h- and p-adaptivity, the local conservation property, and the upwinding stabilization mechanism for stabilizing dominant convection effects.

One of the major difficulties in nonlinear FSI problems stems from the movement of the fluid domain, which makes these problems computationally very challenging, where the major bottleneck is a robust fluid flow solver on deforming domains. Various techniques have been introduced for fluid problems with moving boundaries and interfaces, which include the interface-tracking approaches, e.g., the arbitrary Lagrangian-Eulerian (ALE) method [31, 50] and the space-time method [59, 85, 89] where the computational mesh tracks and fits with the moving interfaces, and the interface-capturing approaches, e.g., the immersed boundary method [60, 72], the immersed finite element method [57,94], the fictitious domain method [46], and the extended/generalized finite element method [19,41], where the computational mesh is static and does not fit to the moving interfaces. The current work focuses on the ALE approach for the fluid solver; see, e.g., [38, 58, 70] for ALE-DG schemes for compressible flow problems, and [36, 90] for incompressible flow problems.

There have been a few ALE-DG fluid solver based schemes for FSI problems, see, e.g., [37, 42, 71] where the nonlinear structure equations were discretized using the standard conforming Galerkin (CG) method, and [54, 90] where the structure equations were also discretized using DG methodologies. We also cite the related work [2] on space-time DG FSI solvers. One major criticism of DG schemes for problems involve linear system solvers is their associated high computational cost when compared to standard CG schemes, mainly due to a larger number of (element-based) degrees of freedom (DOFs) and the element-element DOFs couplings in the resulting linear system problem. The hybridizable discontinuous Galerkin (HDG) methods [20, 25, 64] were introduced to try to address this criticism. Basically, HDG schemes introduce facet-based DOFs on the mesh skeleton so that element-element DOFs couplings in the standard DG schemes are replaced by facet-element couplings, which result in a reduced globally coupled linear system involves facet-based DOFs only after a *static condensation* procedure that locally eliminates the (local) element-based DOFs. Hence the computational cost of HDG schemes are usually much lower than that of the DG schemes, especially for high-order approximations [53, 93]. Besides being computationally cheaper, the HDG methods also produce more accurate approximations than DG methods for certain problems due to their superconvergence property [22–24, 74].

The first HDG scheme for FSI problems was introduced in [81], where the authors combined the HDG incompressible flow and elasticity solvers [64] with a monolithic ALE formulation. The method was further improved in [82] with a reduced computational cost that uses a more efficient elasticity HDG solver and a linear finite element approximate for the ALE map. More recently, an ALE partitioned scheme [55] based on an HDG formulation for the compressible fluid and a CG formulation for the structure has been proposed for FSI problems with a weakly compressible fluid.

For incompressible flow problems, numerical discretizations that yield point-wise divergence-free velocity approximations have attracted increased attention [51], due

to their exact mass conservation property. DG schemes with strongly mass conservative velocity approximations were initially introduced in [26], where the key idea is to use an $H(\mathrm{div})$-conforming velocity approximation that guarantees a point-wise divergence-free velocity approximation. The $H(\mathrm{div})$-conforming DG schemes has been extended to $H(\mathrm{div})$-conforming HDG schemes [28, 45, 56], where additional DOFs on the mesh skeleton (facets) are used to approximate the *tangential* component of velocity field. Very recently, the $H(\mathrm{div})$-conforming HDG scheme for incompressible flows has been applied to moving domain problems [43,61] and to FSI problems [63] using the ALE framework. In particular, in [63] the authors discussed in details the first realization of ALE formulation within $H(\mathrm{div})$-conforming finite elements that use the Piola mapping. Therein, the structure solver was discretized using the standard CG method. We also mention two recent publications [16, 52] that promote the use of strongly mass conserving fluid solvers for FSI problems within the *immersogeometric analysis* framework.

In this contribution, we present a novel HDG-based scheme to solve the nonlinear FSI problem modeled by the incompressible Navier-Stokes equations in the fluid domain and the equations for nonlinear hyperelasticity in the structure domain. The fluid problem is discretized on the moving domain with an ALE divergence-free HDG scheme, and the structure problem is discretized using a hybridized tangential-velocity-normal-normal-stress (TDNNS) scheme recently introduced in [62]. The interface coupling is treated via a generalized Robin condition following [8,13,15,79], and both monolithic and partitioned fully discrete schemes are presented. We further use high-order backward difference formulas (BDFs) for the temporal discretization. Salient features of the the proposed scheme include

- Guaranteed exactly divergence-free fluid velocity approximation throughout on the moving mesh with the use of the ALE divergence-free HDG solver for the fluid sub-problem.
- First realization of TDNNS structure solvers for FSI problems.
- First application of the generalized Robin interface condition in combination with the proposed advanced finite element discretizations, which lead to a robust monolithic scheme and a robust strongly coupled partitioned scheme.
- A reduced global linear system problem for facet-based DOFs only in each linearization step, resulted from the static condensation procedure that eliminates all element-based DOFs.
- High-order spatial and temporal accuracy.

The rest of the paper is organized as follows. In Section 2, we introduce the ALE divergence-free HDG scheme for the moving domain incompressible Navier-Stokes equations. In Section 3, we introduce TDNNS scheme for the equations of nonlinear elasticity. In Section 4, we introduce the fully discrete monolithic and partitioned schemes for the FSI problem by combing the spatial discretizations in the previous two sections, where special attentions are paid to the interface treatment and ALE mapping construction. Numerical results are presented in Section 5. We conclude in Section 6.

2. The ALE divergence-free HDG scheme for incompressible Navier-Stokes

In this section, we introduce the ALE divergence-free HDG scheme for the incompressible Navier-Stokes equations. We largely follow the work [43,63] to derive the method.

2.1. The ALE-Navier-Stokes equations. Consider the Navier-Stokes equations on a moving domain $\Omega_t^f \subset \mathbb{R}^d$, $d \in \{2,3\}$, for $t \in [0,T]$, given by a continuous ALE map [65, 75]:

$$\boldsymbol{\phi}_t : \Omega_0^f \subset \mathbb{R}^d \longrightarrow \Omega_t^f, \qquad \mathbf{x}(\mathbf{x}_0, t) = \boldsymbol{\phi}_t(\mathbf{x}_0), \quad \forall t \in [0,T], \tag{1}$$

where Ω_0^f is the initial (bounded) fluid domain at time $t = 0$ with possibly curved boundaries. In this section we assume that the ALE map $\boldsymbol{\phi}_t$ in (1) is *apriori* given to simplify the presentation.

The Navier-Stokes equations in ALE non-conservative form [65, 75] are given as follows:

$$\rho^f \left.\frac{\partial \boldsymbol{u}^f}{\partial t}\right|_{\mathbf{x}_0} + \rho^f(\boldsymbol{u}^f - \boldsymbol{\omega}^f)\cdot\nabla_{\mathbf{x}}\boldsymbol{u}^f - \mathrm{div}_{\mathbf{x}}(2\mu^f\mathbf{D}_{\mathbf{x}}(\boldsymbol{u}^f) - p^f\boldsymbol{I}) = \rho^f\boldsymbol{f}^f, \quad \text{in } \Omega_t^f \times [0,T] \tag{2a}$$

$$\mathrm{div}_{\mathbf{x}}\boldsymbol{u}^f = 0, \qquad \text{in } \Omega_t^f \times [0,T] \tag{2b}$$

where $\mathbf{D}_{\mathbf{x}}$ is the symmetric strain rate tensor

$$\mathbf{D}_{\mathbf{x}}(\boldsymbol{u}) = \frac{1}{2}(\nabla_{\mathbf{x}}\boldsymbol{u} + (\nabla_{\mathbf{x}}\boldsymbol{u})^T),$$

$\boldsymbol{I}$ is the identity tensor, $\boldsymbol{u}^f(\mathbf{x},t)$ is the fluid velocity field, $p^f(\mathbf{x},t)$ is the pressure, ρ^f is the (constant) fluid density, μ^f is the (constant) coefficient of dynamic viscosity, $\boldsymbol{f}^f$ is the body forces, and

$$\boldsymbol{\omega}^f(\mathbf{x},t) = \left.\frac{\partial \mathbf{x}}{\partial t}\right|_{\mathbf{x}_0} = \frac{\partial \boldsymbol{\phi}_t}{\partial t}\circ\boldsymbol{\phi}_t^{-1}(\mathbf{x}) \tag{3}$$

is the domain velocity. We assume the Navier-Stokes equations (2) are further equipped with the following homogeneous Dirichlet boundary condition:

$$\boldsymbol{u}^f(\mathbf{x},t) = 0, \quad \forall \mathbf{x} \in \partial\Omega^t, \quad t \in [0,T]. \tag{4}$$

2.2. Mesh and finite element spaces.

2.2.1. Mesh and mappings. Let $\mathcal{T}_h^{f,0} := \{K^0\}$ be a conforming simplicial triangulation of the initial fluid domain $\Omega_0^f \subset \mathbb{R}^d$, where the element $K^0 = \Phi_K^0(\widehat{K})$ is a mapped simplex from the reference simplex element

$$\widehat{K} := \{\widehat{\mathbf{x}} = (\widehat{x}_1, \cdots, \widehat{x}_d) : \quad \widehat{x}_i \geq 0,\ \forall 1 \leq i \leq d, \quad \sum_{i=1}^d \widehat{x}_i \leq 1.\}$$

We assume the mapping $\Phi_K^0 \in [\mathcal{P}^m(\widehat{K})]^d$, where $\mathcal{P}^m(\widehat{K})$ is the space of polynomials of degree at most $m \geq 1$ on the reference element $\widehat{K}$. Moreover, let $\mathcal{T}_h^{f,t} := \{K^t = \boldsymbol{\phi}_t(K^0)\}$ be the mapped triangulation of the deformed domain Ω_t^f at time t, where $\boldsymbol{\phi}_t$ is the ALE map given in (1). Denoting the composite mapping $\Phi_K^t = \boldsymbol{\phi}_t \circ \Phi_K^0 : \widehat{K} \to K^t$, we have $K^t = \Phi_K^t(\widehat{K})$. We assume the mesh $\mathcal{T}_h^{f,t}$ is regular in the sense that no elements with a degenerated or negative Jacobian determinant exist. Without loss of generality, we further assume the ALE map (1) is a continuous piecewise polynomial of degree m:

$$\boldsymbol{\phi}_t \in \boldsymbol{S}_h^m := \{\boldsymbol{v} \in [H^1(\Omega_0^f)]^d : \quad \boldsymbol{v}\circ\Phi_K^0(\widehat{\mathbf{x}}) \in [\mathcal{P}^m(\widehat{K})]^d, \quad \forall K^0 \in \mathcal{T}_h^{f,0}\}. \tag{5}$$

For the reference d-dimensional simplex element $\widehat{K}$, we denote $\partial\widehat{K}$ as its boundary, which consists of $(d+1)$ boundary facet $\{\widehat{E}_l := \widehat{\Psi}_l(\widehat{E})\}_{l=1}^{d+1}$, where $\widehat{\Psi}_l$ is the

affine mapping from the reference $(d-1)$-dimensional simplex element $\widehat{E}$ to the boundary facet $\widehat{E}_l$, where

$$\widehat{E} := \{\widehat{\mathbf{z}} = (\widehat{z}_1, \cdots, \widehat{z}_{d-1}) : \quad \widehat{z}_i \geq 0,\ \forall 1 \leq i \leq d-1, \quad \sum_{i=1}^{d-1} \widehat{z}_i \leq 1.\}$$

We need the following Jacobian matrices and their determinants:

$$F_K^t := \nabla_{\widehat{\mathbf{x}}} \Phi_K^t \in \mathbb{R}^{d\times d}, \quad J_K^t := \det(F_K^t), \tag{6a}$$

$$F_0^t := \nabla_{\mathbf{x}_0} \boldsymbol{\phi}_t \in \mathbb{R}^{d\times d}, \quad J_0^t := \det(F_0^t), \tag{6b}$$

$$\widehat{F}_l := \nabla_{\widehat{\mathbf{z}}} \widehat{\Psi}_l \in \mathbb{R}^{d\times (d-1)}, \quad \widehat{J}_l := \sqrt{\det\left((\widehat{F}_l)^T \widehat{F}_l\right)}. \tag{6c}$$

A simple application of the chain rule implies that

$$F_K^t = F_0^t\, F_K^0, \quad J_K^t = J_0^t J_K^0.$$

We denote $\partial \mathcal{T}_h^{f,t} := \{\partial K^t\}$ as the collection of element boundaries of the mesh $\mathcal{T}_h^{f,t}$, where $\partial K^t = \{E_{K,l}^t\}_{l=1}^{d+1}$ is the boundary of element K^t, with $E_{K,l}^t := \Phi_K^t(\widehat{E}_l)$ being the mapped facet. Let $\widehat{\boldsymbol{n}}_l$ be the normal direction of the reference boundary facet $\widehat{E}_l$, and $\boldsymbol{n}_{K,l}^t$ be the normal direction of the physical boundary facet $E_{K,l}^t$. There holds

$$\boldsymbol{n}_{K,l}^t \circ (\Phi_K^t)^{-1} = \frac{(F_K^t)^{-T}\, \widehat{\boldsymbol{n}}_l}{\|(F_K^t)^{-T}\, \widehat{\boldsymbol{n}}_l\|}.$$

We denote $\mathcal{E}_h^{f,t} := \{E^t\}$ as the mesh skeleton of $\mathcal{T}_h^{f,t}$, which consists of all the facets. Here $E^t := \Psi_E^t(\widehat{E})$ with the mapping Φ_E^t constructed by composition: for a facet $E^t = E_{T,l}^t$ that is the l-th boundary facet of an element K^t, we denote $\Psi_E^t : \widehat{E} \to E^t$ as

$$\Psi_E^t := \Phi_K^t \circ \widehat{\Psi}_l.$$

We note that if the facet E^t happens to be an interior facet which is also the m-th boundary facet of another element $\widetilde{K}$, then there holds

$$\Psi_E^t = \Phi_K^t \circ \widehat{\Psi}_l = \Phi_{\widetilde{K}}^t \circ \widehat{\Psi}_m.$$

Hence, the facet mapping Ψ_E^t is uniquely determined as it does not depend on which associated volume element of E^t is used. We now denote the following surface Jacobian matrix, its Moore-Penrose pseudo inverse and determinant for the mapping Ψ_E^t:

$$F_E^t := \nabla_{\widehat{\mathbf{z}}} \Psi_E^t \in \mathbb{R}^{d\times(d-1)},\ (F_E^t)^{-1} := \left((F_E^t)^T F_E^t\right)^{-1} (F_E^t)^T \in \mathbb{R}^{(d-1)\times d},$$
$$J_E^t := \sqrt{\det\left((F_E^t)^T F_E^t\right)}.$$

2.2.2. The finite element spaces. We first introduce the following (discontinuous) finite element spaces on the mesh $\mathcal{T}_h^{f,t}$:

$$W_h^{k,f} := \{w \in L^2(\Omega_t^f) :\ w|_{K^t} = \widehat{w} \circ (\Phi_K^t)^{-1},\ \widehat{w} \in \mathcal{P}^k(\widehat{K}),\ \forall K^t \in \mathcal{T}_h^{f,t}\}, \tag{7a}$$

$$\boldsymbol{V}_h^{k,f} := \{\boldsymbol{v} \in [L^2(\Omega_t^f)]^d :\ \boldsymbol{v}|_{K^t} = \frac{1}{J_K^t} F_K^t \left(\widehat{\boldsymbol{v}} \circ (\Phi_K^t)^{-1}\right),\ \widehat{\boldsymbol{v}} \in [\mathcal{P}^k(\widehat{K})]^d, \tag{7b}$$
$$\forall K^t \in \mathcal{T}_h^{f,t}\},$$

$$\boldsymbol{\Sigma}_h^{k,f} := \{\boldsymbol{\sigma} \in [W_h^{k,f}]^{d\times d} :\ \boldsymbol{\sigma} \text{ is symmetric}\}. \tag{7c}$$

Note that the standard pull-back mapping is used to define the scalar finite element space $W_h^{k,f}$ and the symmetric tensor finite element space $\mathbf{\Sigma}_h^{k,f}$, which will be used to approximate the pressure field p^f, and the strain rate tensor $\mathbf{D}_{\mathbf{x}}(\boldsymbol{u}^f)$, respectively. While the Piola mapping is used to define the vector finite element space $\boldsymbol{V}_h^{k,f}$, which will be used to approximate the fluid velocity $\boldsymbol{u}^f$. The use of Piola mapping in $\boldsymbol{V}_h^{k,f}$ ensures a strong mass conservation for the HDG scheme (9) on curved meshes, see Lemma 2.1 below.

We also need the following (hybrid) finite element spaces on the mesh skeleton $\mathcal{E}_h^{f,t}$:

$$\text{(7d)}\quad \widetilde{W}_h^{k,f} := \{\widetilde{w} \in L^2(\mathcal{E}_h^{f,t}) :\ \widetilde{w}|_{E^t} = \widehat{w} \circ (\Psi_E^t)^{-1},\ \widehat{w} \in \mathcal{P}^k(\widehat{E}),\ \forall E^t \in \mathcal{E}_h^{f,t}\},$$

$$\text{(7e)}\quad \widetilde{\boldsymbol{V}}_h^{k,f} := \{\widetilde{\boldsymbol{v}} \in [L^2(\mathcal{E}_h^{f,t})]^d :\ \widetilde{\boldsymbol{v}}|_{E^t} = \mathsf{tng}\left((F_E^t)^{-T}\,\widehat{\boldsymbol{v}} \circ (\Psi_E^t)^{-1}\right),\ \widehat{\boldsymbol{v}} \in [\mathcal{P}^k(\widehat{E})]^d,\ \forall E^t \in \mathcal{E}_h^{f,t}\},$$

where $\mathsf{tng}(\boldsymbol{v})|_E := \boldsymbol{v} - (\boldsymbol{v}\cdot\boldsymbol{n}_E)\boldsymbol{n}_E$ denotes the tangential component of the vector $\boldsymbol{v}$ on the facet E, whose normal direction is $\boldsymbol{n}_E$. Note that the normal component of functions in $\widetilde{\boldsymbol{V}}_h^{k,f}$ vanishes on the whole mesh skeleton. Here the standard pull-back mapping is used for the scalar skeleton space $\widetilde{W}_h^{k,f}$, which will be used to approximate the normal-normal component of the stress, $\boldsymbol{n}\cdot(2\mu_f\mathbf{D}_{\mathbf{x}}(\boldsymbol{u}^f) - p^f\mathbf{I})\boldsymbol{n}$, on the mesh skeleton, and the covariant mapping is used for the vector skeleton space $\widetilde{\boldsymbol{V}}_h^{k,f}$, which preserves tangential continuity and will be used to approximate the tangential component of fluid velocity, $\mathsf{tng}(\boldsymbol{u}^f)$, on the mesh skeleton.

2.3. The divergence-free HDG scheme: spatial discretization. In this subsection, we focus on the spatial discretization of the equations (2). We work on the physical deformed domain Ω_t^f at a fixed time $t \in [0,T]$. To introduce the scheme, we first reformulate the equations (2) to the following first-order system:

$$\text{(8a)}\qquad \rho^f \left.\frac{\partial \boldsymbol{u}^f}{\partial t}\right|_{\mathbf{x}_0} + \rho^f(\mathrm{div}_{\mathbf{x}}\boldsymbol{\omega}^f)\boldsymbol{u}^f + \mathrm{div}_{\mathbf{x}}(\rho^f(\boldsymbol{u}^f - \boldsymbol{\omega}^f)\otimes\boldsymbol{u}^f - \boldsymbol{\sigma}^f) = \rho^f\boldsymbol{f}^f,$$

$$\text{(8b)}\qquad \boldsymbol{\sigma}^f - (2\mu^f\boldsymbol{\epsilon}^f - p^f\mathbf{I}) = 0,$$

$$\text{(8c)}\qquad \boldsymbol{\epsilon}^f - \mathbf{D}_{\mathbf{x}}(\boldsymbol{u}^f) = 0,$$

$$\text{(8d)}\qquad \mathrm{div}_{\mathbf{x}}\boldsymbol{u}^f = 0.$$

Three local variables (defined on the mesh $\mathcal{T}_h^{f,t}$), namely, the pressure p_h^f, velocity $\boldsymbol{u}_h^f$, and strain rate tensor $\boldsymbol{\epsilon}_h^f$, and two global variables (defined on the mesh skeleton $\mathcal{E}_h^{f,t}$), namely the normal-normal component of the stress $\widetilde{\sigma}_h^f$, and the tangential component of the velocity $\widetilde{\boldsymbol{u}}_h^f$ will be used in our scheme. We use polynomials of degree $k-1$ for the pressure approximation, and polynomials of degree $k \geq 1$ for the other variables, i.e.,

$$p_h^f \in W_h^{k-1,f},\ \ \boldsymbol{\epsilon}_h^f \in \mathbf{\Sigma}_h^{k,f},\ \ \boldsymbol{u}_h^f \in \boldsymbol{V}_h^{k,f},\ \ \widetilde{\sigma}_h^f \in \widetilde{W}_h^{k,f},\ \ \widetilde{\boldsymbol{u}}_h^f \in \widetilde{\boldsymbol{V}}_h^{k,f},$$

The spatial discretization of our HDG scheme for the equations (8) with homogeneous Dirichlet boundary conditions (4) reads as follows: Find $(p_h^f, \boldsymbol{\epsilon}_h^f, \boldsymbol{u}_h^f, \widetilde{\sigma}_h^f, \widetilde{\boldsymbol{u}}_h^f) \in$

$W_h^{k-1,f} \times \boldsymbol{\Sigma}_h^{k,f} \times \boldsymbol{V}_h^{k,f} \times \widetilde{W}_h^{k,f} \times \widetilde{\boldsymbol{V}}_h^{k,f}$ with $\widetilde{\boldsymbol{u}}_h^f|_{\Gamma_h^f} = 0$ such that

$$\left(\rho^f \left.\frac{\partial \boldsymbol{u}_h^f}{\partial t}\right|_{\mathbf{x}_0}, \boldsymbol{v}_h^f\right)_{\mathcal{T}_h^{f,t}} + \left(\rho^f (\mathrm{div}_{\mathbf{x}} \boldsymbol{\omega}^f)\boldsymbol{u}_h^f, \boldsymbol{v}_h^f\right)_{\mathcal{T}_h^{f,t}} \tag{9a}$$
$$- \left(\rho^f (\boldsymbol{u}_h^f - \boldsymbol{\omega}^f) \otimes \boldsymbol{u}_h^f, \nabla_{\mathbf{x}} \boldsymbol{v}_h^f\right)_{\mathcal{T}_h^{f,t}} + 2\mu^f \left(\boldsymbol{\epsilon}_h^f, \nabla_{\mathbf{x}} \boldsymbol{v}_h^f\right)_{\mathcal{T}_h^{f,t}}$$
$$- \left(p_h^f, \mathrm{div}_{\mathbf{x}} \boldsymbol{v}_h^f\right)_{\mathcal{T}_h^{f,t}} - \left\langle \widetilde{\boldsymbol{Flux}}_{\mathrm{v}} - \widetilde{\boldsymbol{Flux}}_{\mathrm{c}},\ \boldsymbol{v}_h^f \right\rangle_{\partial \mathcal{T}_h^{f,t}} = \left(\rho^f \boldsymbol{f}^f, \boldsymbol{v}_h^f\right)_{\mathcal{T}_h^{f,t}},$$

$$2\mu^f \left(\boldsymbol{\epsilon}_h^f - \mathbf{D}_{\mathbf{x}}(\boldsymbol{u}_h^f), \boldsymbol{G}_h^f\right)_{\mathcal{T}_h^{f,t}} + 2\mu^f \left\langle \mathsf{tng}(\boldsymbol{u}_h^f - \widetilde{\boldsymbol{u}}_h^f), \boldsymbol{G}_h^f \boldsymbol{n} \right\rangle_{\partial \mathcal{T}_h^{f,t}} = 0, \tag{9b}$$

$$\left(\mathrm{div}_{\mathbf{x}} \boldsymbol{u}_h^f, q_h^f\right)_{\mathcal{T}_h^{f,t}} = 0, \tag{9c}$$

$$\left\langle \boldsymbol{u}_h^f \cdot \boldsymbol{n}, \widetilde{\tau}_h^f \right\rangle_{\partial \mathcal{T}_h^{f,t}} = 0, \tag{9d}$$

$$\left\langle \widetilde{\boldsymbol{Flux}}_{\mathrm{v}} - \widetilde{\boldsymbol{Flux}}_{\mathrm{c}},\ \mathsf{tng}(\widetilde{\boldsymbol{v}}_h^f) \right\rangle_{\partial \mathcal{T}_h^{f,t}} = 0, \tag{9e}$$

for all $(q_h^f, \boldsymbol{G}_h^f, \boldsymbol{v}_h^f, \widetilde{\tau}_h^f, \widetilde{\boldsymbol{v}}_h^f) \in W_h^{k-1,f} \times \boldsymbol{\Sigma}_h^{k,f} \times \boldsymbol{V}_h^{k,f} \times \widetilde{W}_h^{k,f} \times \widetilde{\boldsymbol{V}}_h^{k,f}$ with $\widetilde{\boldsymbol{v}}_h^f|_{\Gamma_h^f} = 0$, where we write $(\eta, \xi)_{\mathcal{T}_h^{f,t}} := \sum_{K^t \in \mathcal{T}_h^{f,t}} \int_{K^t} \eta \cdot \xi \mathrm{dx}$ as the volume integral, and $\langle \eta, \xi \rangle_{\partial \mathcal{T}_h^{f,t}} := \sum_{K^t \in \mathcal{T}_h^{f,t}} \int_{\partial K^t} \eta \cdot \xi \mathrm{ds}$ as the element-boundary integral. Here the *viscous* and *convective* numerical fluxes are defined as follows:

$$\widetilde{\boldsymbol{Flux}}_{\mathrm{v}} := \widetilde{\sigma}_h^f \boldsymbol{n} + 2\mu^f \mathsf{tng}(\boldsymbol{\epsilon}_h^f \boldsymbol{n}) - \alpha^f\ \mathsf{tng}(\boldsymbol{u}_h^f - \widetilde{\boldsymbol{u}}_h^f), \tag{9f}$$

$$\widetilde{\boldsymbol{Flux}}_{\mathrm{c}} := \rho^f (\boldsymbol{u}_h^f - \boldsymbol{\omega}^f) \cdot \boldsymbol{n} \left((\boldsymbol{u}_h^f \cdot \boldsymbol{n}) \boldsymbol{n} + \mathsf{tng}(\check{\boldsymbol{u}}_h^{f,up}) \right), \tag{9g}$$

where $\mathsf{tng}(\boldsymbol{u}_h^{f,up})$ is the following upwinding flux in the tangential direction:

$$\mathsf{tng}(\check{\boldsymbol{u}}_h^{f,up}) := \begin{cases} \mathsf{tng}(\boldsymbol{u}_h^f) & \text{if } (\boldsymbol{u}_h^f - \boldsymbol{w}^f) \cdot \boldsymbol{n} > 0, \\ \\ \mathsf{tng}(\widetilde{\boldsymbol{u}}_h^f) & \text{if } (\boldsymbol{u}_h^f - \boldsymbol{w}^f) \cdot \boldsymbol{n} \le 0, \end{cases}$$

and the (positive) stabilization parameter α^f is taken to be $\alpha^f = 2\mu^f$.

The following result shows that the fluid velocity approximation is globally divergence free.

Lemma 2.1. *The semi-discrete scheme* (9) *produces a globally divergence-free velocity approximation which has a vanishing normal component on the domain boundary, i.e.,* $\boldsymbol{u}_h^f \in H_0(\mathrm{div}; \Omega_t^f)$*, and* $\mathrm{div}_{\mathbf{x}}\, \boldsymbol{u}_h^f = 0$.

Proof. To simplify the notation, we suppress the superscript t in the following derivation. Since functions in the finite element space $\boldsymbol{V}_h^{k,f}$ are transformed via the Piola mapping, we have $\boldsymbol{u}_h^f|_K = \frac{1}{J_K} F_K \left(\widehat{\boldsymbol{u}} \circ (\Phi_K)^{-1}\right)$ for some function $\widehat{\boldsymbol{u}} \in [\mathcal{P}^k(\widehat{K})]^d$. It is well-known [7] that the following property holds for Poila transformations:

$$\mathrm{div}_{\mathbf{x}}(\boldsymbol{u}_h^f) \circ \Phi_K = \frac{1}{J_K} \mathrm{div}_{\widehat{\mathbf{x}}}(\widehat{\boldsymbol{u}}),$$

which implies that

$$\int_K \mathrm{div}_{\mathbf{x}}(\boldsymbol{u}_h^f)\, \widehat{q} \circ (\Phi_K)^{-1} \mathrm{dx} = \int_{\widehat{K}} \mathrm{div}_{\widehat{\mathbf{x}}}(\widehat{\boldsymbol{u}}) \widehat{q}\, \mathrm{d\widehat{x}},$$

for any function $\widehat{q}$ on the reference element $\widehat{K}$. Since we have $\mathrm{div}_{\widehat{\mathbf{x}}}(\widehat{\boldsymbol{u}}) \in \mathcal{P}^{k-1}(\widehat{K})$, by the definition of the scalar finite element space $W_h^{k-1,f}$, we can take the test function $q_h^f \in W_h^{k-1,f}$ in (9c) such that $q_h^f|_K = \mathrm{div}_{\widehat{\mathbf{x}}}(\widehat{\boldsymbol{u}}) \circ (\Phi_K)^{-1}$ and $q_h^f = 0$ elsewhere, which leads to

$$0 = \int_K \mathrm{div}_{\mathbf{x}}(\boldsymbol{u}_h^f)\, \mathrm{div}_{\widehat{\mathbf{x}}}(\widehat{\boldsymbol{u}}) \circ (\Phi_K)^{-1}\, \mathrm{dx} = \int_{\widehat{K}} (\mathrm{div}_{\widehat{\mathbf{x}}}(\widehat{\boldsymbol{u}}))^2\, \mathrm{d\widehat{x}}.$$

Hence,

$$\mathrm{div}_{\mathbf{x}}(\boldsymbol{u}_h^f)|_K = \frac{1}{J_K} \mathrm{div}_{\widehat{\mathbf{x}}}(\widehat{\boldsymbol{u}}) \circ (\Phi_K)^{-1} = 0. \tag{10}$$

Next, let us prove normal continuity of $\boldsymbol{u}_h^f$ across interior element boundaries. Let $E_{ij} \in \mathcal{E}_h^{f,t}$ be an interior facet which is the l-th facet, $E_{K_i,l}$, of element K_i, and the m-th facet, $E_{K_j,m}$, of element K_j. Restricting the equation (9d) to the facet E_{ij}, we have

$$\int_{E_{K_i,l}} (\boldsymbol{u}_h^f \cdot \boldsymbol{n}_{K_i,l}) \widehat{\tau} \circ (\Psi_{E_{ij}})^{-1} \mathrm{ds} + \int_{E_{K_j,m}} (\boldsymbol{u}_h^f \cdot \boldsymbol{n}_{K_j,m}) \widehat{\tau} \circ (\Psi_{E_{ij}})^{-1} \mathrm{ds} = 0, \quad \forall \widehat{\tau} \in \mathcal{P}^k(\widehat{E}). \tag{11}$$

Let $\widehat{\boldsymbol{u}}_i$ and $\widehat{\boldsymbol{u}}_j$ be functions in $[\mathcal{P}^k(\widehat{K})]^d$ such that

$$\boldsymbol{u}_h^f|_{K_i} = \frac{1}{J_{K_i}} F_{K_i} \widehat{\boldsymbol{u}}_i, \quad \boldsymbol{u}_h^f|_{K_j} = \frac{1}{J_{K_j}} F_{K_j} \widehat{\boldsymbol{u}}_j.$$

A simple calculation yields

$$(\boldsymbol{u}_h^f \cdot \boldsymbol{n}_{K_i,l}) \circ \Phi_{K_i} = \frac{1}{J_{K_i} \|(F_{K_i})^{-T} \widehat{\boldsymbol{n}}_l\|} \widehat{\boldsymbol{u}}_i \cdot \widehat{\boldsymbol{n}}_l \quad \text{on } \widehat{E}_l, \tag{12}$$

where $J_{K_i} \|(F_{K_i})^{-T} \widehat{\boldsymbol{n}}_l\| = |E_{ij}|/|\widehat{E}_l|$ is the ratio of facet measures. Hence, we have

$$\int_{E_{K_i,l}} (\boldsymbol{u}_h^f \cdot \boldsymbol{n}_{K_i,l}) \widehat{\tau} \circ (\Psi_{E_{ij}})^{-1} \mathrm{ds} = \int_{\widehat{E}_l} (\widehat{\boldsymbol{u}}_i \cdot \widehat{\boldsymbol{n}}_l) \widehat{\tau} \circ (\widehat{\Psi}_l)^{-1}\, \mathrm{d\widehat{s}} = \int_{\widehat{E}} \left(\widehat{J}_l (\widehat{\boldsymbol{u}}_i \cdot \widehat{\boldsymbol{n}}_l) \circ \widehat{\Psi}_l \right) \widehat{\tau}\, \mathrm{d\widehat{s}}.$$

Substituting the above equation back to (11), we get

$$\int_{\widehat{E}} \left(\widehat{J}_l (\widehat{\boldsymbol{u}}_i \cdot \widehat{\boldsymbol{n}}_l) \circ \widehat{\Psi}_l + \widehat{J}_m (\widehat{\boldsymbol{u}}_j \cdot \widehat{\boldsymbol{n}}_m) \circ \widehat{\Psi}_m \right) \widehat{\tau}\, \mathrm{d\widehat{s}} = 0, \quad \forall \widehat{\tau} \in \mathcal{P}^k(\widehat{E}).$$

Since $\widehat{J}_l (\widehat{\boldsymbol{u}}_i \cdot \widehat{\boldsymbol{n}}_l) \circ \widehat{\Psi}_l + \widehat{J}_m (\widehat{\boldsymbol{u}}_j \cdot \widehat{\boldsymbol{n}}_m) \circ \widehat{\Psi}_m \in \mathcal{P}^k(\widehat{E})$, it must be *zero*. Finally, by equation (12) and the fact that $\widehat{J}_l = |\widehat{E}_l|/|\widehat{E}|$, we have

$$\left((\boldsymbol{u}_h^f \cdot \boldsymbol{n}_{K_i,l})|_{K_i} + (\boldsymbol{u}_h^f \cdot \boldsymbol{n}_{K_i,l})|_{K_j} \right) \circ \Psi_{E_{ij}} = \frac{|\widehat{E}|}{|\widehat{E}_{ij}|} (\widehat{J}_l (\widehat{\boldsymbol{u}}_i \cdot \widehat{\boldsymbol{n}}_l) \circ \widehat{\Psi}_l + \widehat{J}_m (\widehat{\boldsymbol{u}}_j \cdot \widehat{\boldsymbol{n}}_m) \circ \widehat{\Psi}_m) = 0 \tag{13}$$

Similarly, we can prove $\boldsymbol{u}_h^f \cdot \boldsymbol{n}|_{\Gamma_h^f} = 0$ by working on the equation (9d) on the domain boundary. Combining the results (10) and (13), we readily get $\boldsymbol{u}_h^f \in H_0(\mathrm{div}; \Omega)$ and $\mathrm{div}_{\mathbf{x}} \boldsymbol{u}_h^f = 0$. This completes the proof. □

To further simplify the notation, we denote the compound space and variables

$$\begin{aligned} \underline{\boldsymbol{X}}_h^{k,f} &:= W_h^{k-1,f} \times \boldsymbol{\Sigma}_h^{k,f} \times \boldsymbol{V}_h^{k,f} \times \widetilde{W}_h^{k,f} \times \widetilde{\boldsymbol{V}}_h^{k,f}, \\ \underline{U}_h^f &:= (p_h^f, \boldsymbol{\epsilon}_h^f, \boldsymbol{u}_h^f, \widetilde{\sigma}_h^f, \widetilde{\boldsymbol{u}}_h^f) \in \underline{\boldsymbol{X}}_h^{k,f}, \quad \underline{V}_h^f := (q_h^f, \boldsymbol{G}_h^f, \boldsymbol{v}_h^f, \widetilde{\tau}_h^f, \widetilde{\boldsymbol{v}}_h^f) \in \underline{\boldsymbol{X}}_h^{k,f}, \end{aligned}$$

and introduce the following operators associated with the scheme (9):

(14a)
$$\mathcal{M}_h^f(\underline{U}_h^f,\underline{V}_h^f) := \left(\rho^f \boldsymbol{u}_h^f, \boldsymbol{v}_h^f\right)_{\mathcal{T}_h^{f,t}},$$

(14b)
$$\begin{aligned}\mathcal{C}_h^f\left(\boldsymbol{w}^f;\underline{U}_h^f,\underline{V}_h^f\right) :=& \left(-\rho^f(\mathrm{div}_{\mathbf{x}}\boldsymbol{w}^f)\boldsymbol{u}_h^f,\boldsymbol{v}_h^f\right)_{\mathcal{T}_h^{f,t}} - \left(\rho^f\boldsymbol{w}^f\otimes\boldsymbol{u}_h^f,\nabla_{\mathbf{x}}\boldsymbol{v}_h^f\right)_{\mathcal{T}_h^{f,t}}\\ &+\left\langle\widetilde{\boldsymbol{Flux}}_{\mathrm{c}},\mathsf{tng}(\boldsymbol{v}_h^f-\widetilde{\boldsymbol{v}}_h^f)\right\rangle_{\partial\mathcal{T}_h^{f,t}} + \left\langle\rho^f\boldsymbol{w}^f\cdot\boldsymbol{n}(\boldsymbol{u}_h^f\cdot\boldsymbol{n}),\boldsymbol{v}_h^f\cdot\boldsymbol{n}\right\rangle_{\partial\mathcal{T}_h^{f,t}},\end{aligned}$$

(14c)
$$\begin{aligned}\mathcal{A}_h^f\left(\underline{U}_h^f,\underline{V}_h^f\right) :=& 2\mu^f\left(\boldsymbol{\epsilon}_h^f,\nabla_{\mathbf{x}}\boldsymbol{v}_h^f\right)_{\mathcal{T}_h^{f,t}} - \left(p_h^f,\mathrm{div}_{\mathbf{x}}\boldsymbol{v}_h^f\right)_{\mathcal{T}_h^{f,t}} - \left\langle\widetilde{\boldsymbol{Flux}}_{\mathrm{v}},\ \mathsf{tng}(\boldsymbol{v}_h^f-\widetilde{\boldsymbol{v}}_h^f)\right\rangle_{\partial\mathcal{T}_h^{f,t}}\\ &+2\mu^f\left(\boldsymbol{\epsilon}_h^f-\mathbf{D}_{\mathbf{x}}(\boldsymbol{u}_h^f),\boldsymbol{G}_h^f\right)_{\mathcal{T}_h^{f,t}} + 2\mu^f\left\langle\mathsf{tng}(\boldsymbol{u}_h^f-\widetilde{\boldsymbol{u}}_h^f),\boldsymbol{G}_h^f\boldsymbol{n}\right\rangle_{\partial\mathcal{T}_h^{f,t}}\\ &-\left\langle\widetilde{\sigma}_h^f,\boldsymbol{v}_h^f\cdot\boldsymbol{n}\right\rangle_{\partial\mathcal{T}_h^{f,t}} + \left(\mathrm{div}_{\mathbf{x}}\boldsymbol{u}_h^f,q_h^f\right)_{\mathcal{T}_h^{f,t}} + \left\langle\boldsymbol{u}_h^f\cdot\boldsymbol{n},\widetilde{\tau}_h^f\right\rangle_{\partial\mathcal{T}_h^{f,t}},\end{aligned}$$

(14d)
$$\mathcal{F}_h^f(\underline{V}_h^f) := \left(\rho^f\boldsymbol{f}^f,\boldsymbol{v}_h^f\right)_{\mathcal{T}_h^{f,t}}.$$

Then the scheme (9) can be expressed as the following compact form: find $\underline{U}_h^f\in\underline{\boldsymbol{X}}_h^{k,f}$ with $\widetilde{\boldsymbol{u}}_h^f|_{\Gamma_h^f}=0$ such that

$$\mathcal{M}_h^f(\frac{\partial\underline{U}_h^f}{\partial t}\Big|_{\mathbf{x}_0},\underline{V}_h^f) + \mathcal{C}_h^f\left(\boldsymbol{u}_h^f-\boldsymbol{\omega}^f;\underline{U}_h^f,\underline{V}_h^f\right) + \mathcal{A}_h^f\left(\underline{U}_h^f,\underline{V}_h^f\right) = \mathcal{F}_h^f(\underline{V}_h^f), \tag{15}$$

for all $\underline{V}_h^f\in\underline{\boldsymbol{X}}_h^{k,f}$ with $\widetilde{\boldsymbol{v}}_h^f|_{\Gamma_h^f}=0$.

Energy stability of the semi-discrete scheme is given below.

Theorem 2.1. *Let $(p_h^f,\boldsymbol{\epsilon}_h^f,\boldsymbol{u}_h^f,\widetilde{\sigma}_h^f,\widetilde{\boldsymbol{u}}_h^f)\in W_h^{k-1,f}\times\boldsymbol{\Sigma}_h^{k,f}\times\boldsymbol{V}_h^{k,f}\times\widetilde{W}_h^{k,f}\times\widetilde{\boldsymbol{V}}_h^{k,f}$ be the solution to the scheme (9). The following energy identity holds:*

$$\frac{1}{2}\frac{d}{dt}\left(\rho^f\boldsymbol{u}_h^f,\boldsymbol{u}_h^f\right)_{\mathcal{T}_h^{f,t}} + 2\mu^f\left(\boldsymbol{\epsilon}_h^f,\boldsymbol{\epsilon}_h^f\right)_{\mathcal{T}_h^{f,t}} + \left\langle\gamma_h\left|\mathsf{tng}(\boldsymbol{u}_h^f-\widetilde{\boldsymbol{u}}_h^f)\right|^2,1\right\rangle_{\partial\mathcal{T}_h^{f,t}} = \left(\rho^f\boldsymbol{f}^f,\boldsymbol{v}_h^f\right)_{\mathcal{T}_h^{f,t}},$$

where the parameter $\gamma_h := \alpha^f + \rho^f|(\boldsymbol{u}_h^f-\boldsymbol{\omega}_h^f)\cdot\boldsymbol{n}|$ is positive.

Proof. Taking test functions in equations (9) as the trial functions, we get

$$T_1+T_2+T_3 = \mathcal{F}_h^f(\boldsymbol{v}_h^f), \tag{16}$$

where

$$T_1 = \mathcal{M}_h^f(\frac{\partial\boldsymbol{u}_h^f}{\partial t}\Big|_{\mathbf{x}_0},\boldsymbol{u}_h^f),\qquad T_2 = \mathcal{C}_h^f\left(\boldsymbol{u}_h^f-\boldsymbol{\omega}^f;(\boldsymbol{u}_h^f,\widetilde{\boldsymbol{u}}_h^f),(\boldsymbol{u}_h^f,\widetilde{\boldsymbol{u}}_h^f)\right),$$
$$T_3 = \mathcal{A}_h^f\left((p_h^f,\boldsymbol{\epsilon}_h^f,\boldsymbol{u}_h^f,\widetilde{\sigma}_h^f,\widetilde{\boldsymbol{u}}_h^f),(p_h^f,\boldsymbol{\epsilon}_h^f,\boldsymbol{u}_h^f,\widetilde{\sigma}_h^f,\widetilde{\boldsymbol{u}}_h^f)\right).$$

Using the well-known identity $\frac{\partial}{\partial t}J_0^t = J_0^t\,\mathrm{div}_{\mathbf{x}}\boldsymbol{\omega}^f$, we get

$$\begin{aligned}T_1 &= \frac{1}{2}\frac{d}{dt}\left(J_0^t\rho^f\boldsymbol{u}_h^f,\boldsymbol{u}_h^f\right)_{\mathcal{T}_h^{f,0}} - \frac{1}{2}\left(J_0^t(\mathrm{div}_{\mathbf{x}}\boldsymbol{\omega}^f)\rho^f\boldsymbol{u}_h^f,\boldsymbol{u}_h^f\right)_{\mathcal{T}_h^{f,0}}\\ &= \frac{1}{2}\frac{d}{dt}\left(\rho^f\boldsymbol{u}_h^f,\boldsymbol{u}_h^f\right)_{\mathcal{T}_h^{f,t}} - \frac{1}{2}\left(\rho^f(\mathrm{div}_{\mathbf{x}}\boldsymbol{\omega}^f)\boldsymbol{u}_h^f,\boldsymbol{u}_h^f\right)_{\mathcal{T}_h^{f,t}},\end{aligned}$$

Integration by parts yields that

$$\begin{aligned}
&\left(\rho^f(\boldsymbol{u}_h^f-\boldsymbol{\omega}^f)\otimes\boldsymbol{u}_h^f,\nabla_{\mathbf{x}}\boldsymbol{u}_h^f\right)_{\mathcal{T}_h^{f,t}}\\
=\;&-\frac{1}{2}\left(\rho^f\mathrm{div}(\boldsymbol{u}_h^f-\boldsymbol{\omega}^f)\boldsymbol{u}_h^f,\boldsymbol{u}_h^f\right)_{\mathcal{T}_h^{f,t}}+\frac{1}{2}\left\langle\rho^f(\boldsymbol{u}_h^f-\boldsymbol{\omega}^f)\cdot\boldsymbol{n}\,\boldsymbol{u}_h^f,\boldsymbol{u}_h^f\right\rangle_{\partial\mathcal{T}_h^{f,t}}\\
=\;&\frac{1}{2}\left(\rho^f(\mathrm{div}\boldsymbol{\omega}^f)\boldsymbol{u}_h^f,\boldsymbol{u}_h^f\right)_{\mathcal{T}_h^{f,t}}+\frac{1}{2}\left\langle\rho^f(\boldsymbol{u}_h^f-\boldsymbol{\omega}^f)\cdot\boldsymbol{n}\,\mathsf{tng}(\boldsymbol{u}_h^f),\mathsf{tng}(\boldsymbol{u}_h^f)\right\rangle_{\partial\mathcal{T}_h^{f,t}},
\end{aligned}$$

where we used the fact that $\boldsymbol{u}_h^f\in H_0(\mathrm{div};\Omega_f^t)$ and $\mathrm{div}_{\mathbf{x}}\boldsymbol{u}_h^f=0$ in the last step. Combining the above identity with the definition of T_2, and the definition of the upwinding flux $\check{\boldsymbol{u}}_h^{f,up}$ and simplifying the terms, we get

$$T_2=\frac{1}{2}\left(\rho^f(\mathrm{div}\boldsymbol{\omega}^f)\boldsymbol{u}_h^f,\boldsymbol{u}_h^f\right)_{\mathcal{T}_h^{f,t}}+\frac{1}{2}\left\langle\rho^f\left|(\boldsymbol{u}_h^f-\boldsymbol{\omega}^f)\cdot\boldsymbol{n}\right|\,\mathsf{tng}(\boldsymbol{u}_h^f-\widetilde{\boldsymbol{u}}_h^f),\mathsf{tng}(\boldsymbol{u}_h^f-\widetilde{\boldsymbol{u}}_h^f)\right\rangle_{\partial\mathcal{T}_h^{f,t}}$$

Simplifying the terms in T_3, we obtain

$$T_3=2\mu^f\left(\boldsymbol{\epsilon}_h^f,\boldsymbol{\epsilon}_h^f\right)_{\mathcal{T}_h^{f,t}}+\left\langle\alpha^f\,\mathsf{tng}(\boldsymbol{u}_h^f-\widetilde{\boldsymbol{u}}_h^f),\mathsf{tng}(\boldsymbol{u}_h^f-\widetilde{\boldsymbol{u}}_h^f)\right\rangle_{\partial\mathcal{T}_h^{f,t}}.$$

The equality in Theorem 2.1 is then obtained by simply substituting the above three terms back to equation (16). □

2.4. ALE divergence-free HDG scheme: temporal discretization. In this subsection, we consider the temporal discretization for the semidiscrete scheme (9).

We work on the time derivative term in (9a), restricting to a single element $K^t\in\mathcal{T}_h^{f,t}$. Let $\left\{\widehat{\boldsymbol{\psi}}_i(\widehat{\mathbf{x}})\right\}_{i=1}^N$ be a set of basis functions for the space $[\mathcal{P}^k(\widehat{K})]^d$, where $N=d\binom{n+d}{k}=\dim[\mathcal{P}^k(\widehat{K})]^d$. Then the function $\boldsymbol{u}_h^f$, restricting to the element K^t, can be expressed as

$$\boldsymbol{u}_h^f\Big|_{K^t}=\frac{1}{J_K^t}F_K^t\sum_{i=1}^N\mathsf{u}_i(t)\widehat{\boldsymbol{\psi}}_i\circ(\Phi_K^t)^{-1}=\frac{1}{J_0^t}F_0^t\sum_{i=1}^N\mathsf{u}_i(t)\boldsymbol{\psi}_i^0\circ(\boldsymbol{\phi}_t)^{-1},$$

where $\mathsf{u}_i:[0,T]\to\mathbb{R}$ is the coefficient associated to the i-th basis, and

$$\boldsymbol{\psi}_i^0(\mathbf{x}_0)=\frac{1}{J_K^0}F_K^0\widehat{\boldsymbol{\psi}}_i\circ(\Phi_K^0)^{-1}(\mathbf{x}_0)$$

is the mapped (time-independent) basis on the initial element K^0. Applying the chain rule, we get

(17)

$$\begin{aligned}
\left.\frac{\partial\boldsymbol{u}_h^f}{\partial t}\right|_{\mathbf{x}_0}&=\frac{\partial}{\partial t}(\frac{1}{J_0^t}F_0^t)\sum_{i=1}^N\mathsf{u}_i(t)\boldsymbol{\psi}_i^0\circ(\boldsymbol{\phi}_t)^{-1}+(\frac{1}{J_0^t}F_0^t)\sum_{i=1}^N\frac{d}{dt}\mathsf{u}_i(t)\boldsymbol{\psi}_i^0\circ(\boldsymbol{\phi}_t)^{-1}\\
&=\left(\nabla_{\mathbf{x}}\boldsymbol{\omega}^f-(\mathrm{div}_{\mathbf{x}}\boldsymbol{\omega}^f)\mathbf{I}\right)\frac{1}{J_0^t}F_0^t\sum_{i=1}^N\mathsf{u}_i(t)\boldsymbol{\psi}_i^0\circ(\boldsymbol{\phi}_t)^{-1}+(\frac{1}{J_0^t}F_0^t)\sum_{i=1}^N\frac{d}{dt}\mathsf{u}_i(t)\boldsymbol{\psi}_i^0\circ(\boldsymbol{\phi}_t)^{-1}
\end{aligned}$$

where the first term in the above right hand side is due to the use of the (time-dependent) Piola mapping; see [63] for a similar derivation. Now time derivative only appears in the coefficients u_i in the above right hand side, which can be discretized using a standard ODE solver. We use the backward difference formulas (BDFs) in this work, assuming a constant time step size throughout. Alternatively, one can apply variable time step size BDF schemes [33], or other stiff ODE solver like the Crank-Nicolson method or the implicit Runge-Kutta methods [47].

TABLE 1. BDF Coefficients

order m	b_0^m	b_1^m	b_2^m	b_3^m	b_4^m	b_5^m	b_6^m
1	1	-1					
2	3/2	-2	1/2				
3	11/6	-3	3/2	-1/3			
4	25/12	-4	3	-4/3	1/4		
5	137/60	-5	5	-10/3	5/4	-1/5	
6	49/20	-6	15/2	-20/3	15/4	-6/5	1/6

To simplify the notation, we denote $\boldsymbol{u}_h^{f,n}$ as the solution $\boldsymbol{u}_h^f$ with coefficients u_i evaluated at time $t^n = n\Delta t$, where Δt is the (constant) time step size, i.e.,

$$\boldsymbol{u}_h^{f,n}\Big|_{K^t} = \frac{1}{J_0^t} F_0^t \sum_{i=1}^{N} \mathsf{u}_i(t^n)\boldsymbol{\psi}_i^0 \circ (\boldsymbol{\phi}_t)^{-1}, \quad \forall t \in [0,T].$$

Then, the m-th order BDF (BDF[m]) time discretization of the term in (17) at time t^n is

$$D_t^m \boldsymbol{u}_h^{f,n} := \frac{\sum_{j=0}^m b_j^m \boldsymbol{u}_h^{j,n-j}}{\Delta t} + \left(\nabla_{\mathbf{x}}\boldsymbol{\omega}^{f,n} - (\mathrm{div}_{\mathbf{x}}\boldsymbol{\omega}^{f,n})\mathbf{I}\right)\boldsymbol{u}_h^{f,n}, \tag{18}$$

where $\boldsymbol{\omega}^{f,n} = \boldsymbol{\omega}^f(t^n)$ is the mesh velocity at time t^n, and the BDF coefficients b_j^m for $1 \le m \le 6$ are given in Table 1.

The fully discrete ALE divergence-free HDG scheme with BDF[m] time stepping is obtained from the semidiscrete scheme (9) by replacing the term $\frac{\partial \boldsymbol{u}_h^f}{\partial t}(t^n)\Big|_{\mathbf{x}_0}$ with $D_t^m \boldsymbol{u}_h^{f,n}$ in (18), and evaluating all the other terms at time level t^n: Given data $\boldsymbol{u}_h^{f,n-j} \in \boldsymbol{V}_h^{k,f}$ at time t^{n-j} for $j \in \{1,2,\cdots,m\}$, find $\underline{U}_h^{f,n} \in \underline{\boldsymbol{X}}_h^{k,f}$ at time t^n with $\widetilde{\boldsymbol{u}}_h^{f,n}|_{\Gamma_h^f} = 0$ such that

$$\mathcal{M}_h^f\left(D_t^m \underline{U}_h^{f,n}, \underline{V}_h^f\right) + \mathcal{C}_h^f\left(\boldsymbol{u}_h^{f,n} - \boldsymbol{\omega}^{f,n}; \underline{U}_h^{f,n}, \underline{V}_h^f\right) + \mathcal{A}_h^f\left(\underline{U}_h^{f,n}, \underline{V}_h^f\right) = \mathcal{F}_h^f(\underline{V}_h^f). \tag{19}$$

for all $\underline{V}_h^f \in \underline{\boldsymbol{X}}_h^{k,f}$ with $\widetilde{\boldsymbol{v}}_h^f|_{\Gamma_h^f} = 0$.

Remark 2.1 (Semi-implicit convection treatment)**.** *The scheme* (19) *leads to a nonlinear system due to a fully implicit treatment of the nonlinear convection term. A slightly cheaper method is to treat the convection term semi-implicitly by replacing the implicit convection velocity term* $\boldsymbol{u}_h^{f,n} - \boldsymbol{\omega}^{f,n}$ *in equation* (19) *with the following extrapolation with a matching order*

$$\boldsymbol{u}_h^{f,n,*m} - \boldsymbol{\omega}^{f,n},$$

where

$$\boldsymbol{u}_h^{f,n,*m} := \sum_{j=1}^{m} c_j^m \boldsymbol{u}_h^{f,n-j} \tag{20}$$

is the m*-th order extrapolation of* $\boldsymbol{u}_h^{f,n}$ *from data* $\{\boldsymbol{u}_h^{f,n-j}\}_{j=1}^m$ *with the extrapolation coefficients given in Table 2. This leads to a linear scheme with a similar stability property as the original nonlinear scheme* (19)*.*

TABLE 2. Extrapolation Coefficients

order m	c_1^m	c_2^m	c_3^m	c_4^m	c_5^m	c_6^m
1	1					
2	2	-1				
3	3	-3	1			
4	4	-6	4	-1		
5	5	-10	10	-5	1	
6	6	-15	20	-15	6	-1

3. The TDNNS scheme for nonlinear elasticity

In this section, we discretize the nonlinear elasticity equations within the Lagrangian framework using the recently introduced three-field Tangential-Displacement and Normal-Normal-Stress (TDNNS) method [62]. Three different TDNNS approaches were introduced for nonlinear elastostatics in [62] based on different approximation variables. Here we focus on the $\boldsymbol{F}$-based scheme [62] where the deformation gradient serves as a new unknown. We refer to the references [67–69,83] for the origin and analysis of the TDNNS method for linear elasticity problems.

3.1. The equations of elastodynamics. We consider the following nonlinear elasticity problem with a hyperelastic material in a Hu-Washizu formulation [91] on the fixed reference domain $\Omega^s \in \mathbb{R}$ for time $t \in (0, T]$:

$$\frac{\partial}{\partial t}\boldsymbol{d} - \boldsymbol{u}^s = 0, \tag{21a}$$

$$\rho^s \frac{\partial}{\partial t}\boldsymbol{u}^s - \mathrm{div}\boldsymbol{P} = \rho^s \boldsymbol{f}^s, \tag{21b}$$

$$\boldsymbol{P} - \frac{\partial \Psi(\boldsymbol{F})}{\partial \boldsymbol{F}} = 0, \tag{21c}$$

$$\boldsymbol{F} - \nabla \boldsymbol{d} - \mathbf{I} = 0, \tag{21d}$$

where $\boldsymbol{d}$ is the structure displacement field, $\boldsymbol{u}^s$ is the structure velocity (on reference domain), $\boldsymbol{F}$ is the deformation gradient, $\boldsymbol{P}$ is the first Piola-Kirchhoff stress tensor, and $\Psi(\boldsymbol{F})$ is the hyperelastic potential, where we use the following Saint Venant-Kirchhoff model in the current work

$$\Psi(\boldsymbol{F}) := \frac{\lambda^s}{2}\mathrm{tr}(\boldsymbol{E})^2 + \mu^s \boldsymbol{E} : \boldsymbol{E}, \qquad \boldsymbol{E} := \frac{1}{2}(\boldsymbol{F}^T\boldsymbol{F} - \mathbf{I}),$$

with λ^s, μ^s being the two Lamé parameters. In this case, we have

$$\frac{\partial \Psi}{\partial \boldsymbol{F}} = \boldsymbol{F}(\lambda^s \mathrm{tr}(\boldsymbol{E})\mathbf{I} + 2\mu^s \boldsymbol{E}).$$

The TDNNS scheme [62] is based on a splitting of the stress and deformation tensors into a symmetric and skew-symmetric part:

$$\boldsymbol{P} = \boldsymbol{P}_{\mathrm{sym}} + \boldsymbol{P}_{\mathrm{skw}}, \quad \boldsymbol{F} = \boldsymbol{F}_{\mathrm{sym}} + \boldsymbol{F}_{\mathrm{skw}},$$

where $\boldsymbol{G}_{\mathrm{sym}} := \frac{1}{2}(\boldsymbol{G} + \boldsymbol{G}^T)$ and $\boldsymbol{G}_{\mathrm{skew}} := \frac{1}{2}(\boldsymbol{G} - \boldsymbol{G}^T)$ for a tensor $\boldsymbol{G}$. Using the above splitting, and taking the time derivative of equation (21d), we get the

following set of equations that will be used in the discretization:

$$\frac{\partial}{\partial t}\boldsymbol{d} - \boldsymbol{u}^s = 0, \tag{22a}$$

$$\rho^s \frac{\partial}{\partial t}\boldsymbol{u}^s - \mathrm{div}\boldsymbol{P}_{\mathrm{sym}} - \mathrm{div}\boldsymbol{P}_{\mathrm{skw}} = \rho^s \boldsymbol{f}^s, \tag{22b}$$

$$\boldsymbol{P}_{\mathrm{sym}} - (\frac{\partial \Psi(\boldsymbol{F})}{\partial \boldsymbol{F}})_{\mathrm{sym}} = 0, \quad \boldsymbol{P}_{\mathrm{skw}} = (\frac{\partial \Psi(\boldsymbol{F})}{\partial \boldsymbol{F}})_{\mathrm{skw}}, \tag{22c}$$

$$\frac{\partial}{\partial t}\boldsymbol{F}_{\mathrm{sym}} - \epsilon(\boldsymbol{u}) = 0, \quad \boldsymbol{F}_{\mathrm{skw}} = (\nabla \boldsymbol{d})_{\mathrm{skw}}, \tag{22d}$$

where $\epsilon(\boldsymbol{u}) = (\nabla \boldsymbol{u})_{\mathrm{sym}}$ is the linearized strain tensor.

The TDNNS method use $H(\mathrm{curl})$-conforming vectorial finite elements to approximate the velocity field $\boldsymbol{u}^s$ and displacement field $\boldsymbol{d}$, whose tangential component is continuous across element boundaries, and a symmetric tensorial finite element space whose normal-normal component is continuous across element boundaries to approximate the symmetric part of the stress tensor $\boldsymbol{P}_{\mathrm{sym}}$. Moreover, a discontinuous symmetric tensorial finite element space is used to approximate the symmetric deformation gradient $\boldsymbol{F}_{\mathrm{sym}}$. No finite element spaces are involved with the skew-symmetric parts $\boldsymbol{P}_{\mathrm{skw}}$ and $\boldsymbol{F}_{\mathrm{skw}}$, which will be directly obtained by the identities in (22c) and (22d).

To improve efficiency of the scheme, the hybridization technique [67] is used to break the normal-normal continuity of $\boldsymbol{P}_{\mathrm{sym}}$ and re-enforce it via the introduction of a Lagrange multiplier which can be interpreted as normal displacements on the mesh skeleton. Details of the finite element spaces and the TDNNS discretization are given below.

3.2. Mesh and finite element spaces.

3.2.1. Mesh and mappings. We consider a similar mesh setting as that in Section 2, except that the structure domain and the associated mesh do not move over time. In particular, $\mathcal{T}_h^s := \{K\}$ is a conforming simplicial triangulation of the structure domain $\Omega^s \subset \mathbb{R}^d$, where the element $K = \Phi_K(\widehat{K})$ is a mapped simplex from the reference simplex element $\widehat{K}$, $\partial\mathcal{T}_h^s := \{\partial K := \Phi_K(\partial\widehat{K})\}$ is the collection of element boundaries of the mesh $\mathcal{T}_h^s$, and $\mathcal{E}_h^s := \{E := \Psi_E(\widehat{E})\}$ is the mesh skeleton, where $\Psi_E : \widehat{E} \to E$ is the mapping between the reference surface element $\widehat{E}$ and the physical facet E.

3.2.2. The finite element spaces. We introduce the following finite element spaces on the structure mesh $\mathcal{T}_h^s$ and its mesh skeleton $\mathcal{E}_h^s$:

$$\boldsymbol{\Sigma}_h^{k,s} := \{\boldsymbol{\sigma} \in [L^2(\Omega^s)]^{d\times d}_{\mathrm{sym}} : \ \boldsymbol{\sigma}|_K = \frac{1}{J_K^2} F_K(\widehat{\boldsymbol{\sigma}} \circ (\Phi_K)^{-1}) F_K^T, \ \widehat{\boldsymbol{\sigma}} \in [\mathcal{P}^k(\widehat{K})]^{d\times d}_{\mathrm{sym}}, \ \forall K \in \mathcal{T}_h^s\}, \tag{23a}$$

$$\boldsymbol{\Lambda}_h^{k,s} := \{\boldsymbol{\lambda} \in [L^2(\Omega^s)]^{d\times d}_{\mathrm{sym}} : \ \boldsymbol{\lambda}|_K = F_K^{-T}(\widehat{\boldsymbol{\lambda}} \circ (\Phi_K)^{-1}) F_K^{-1}, \ \widehat{\boldsymbol{\lambda}} \in [\mathcal{P}^k(\widehat{K})]^{d\times d}_{\mathrm{sym}}, \ \forall K \in \mathcal{T}_h^s\}, \tag{23b}$$

$$\boldsymbol{V}_h^{k,s} := \left\{\boldsymbol{v} \in H(\mathrm{curl};\Omega^s) : \ \boldsymbol{v}|_K = F_K^{-T}\left(\widehat{\boldsymbol{v}} \circ (\Phi_K)^{-1}\right), \ \widehat{\boldsymbol{v}} \in [\mathcal{P}^k(\widehat{K})]^d, \ \forall K \in \mathcal{T}_h^s\right\}, \tag{23c}$$

$$\widetilde{\boldsymbol{V}}_h^{k,s} := \{\widetilde{\boldsymbol{v}} \in [L^2(\mathcal{E}_h^s)]^d : \ \widetilde{\boldsymbol{v}}|_E = \mathsf{nrm}\left(\frac{1}{J_E} F_E \, \widehat{\boldsymbol{v}} \circ (\Psi_E)^{-1}\right), \ \widehat{\boldsymbol{v}} \in [\mathcal{P}^k(\widehat{E})]^d, \quad \forall E \in \mathcal{E}_h^s\}, \tag{23d}$$

where $\mathsf{nrm}(\boldsymbol{v})|_E := (\boldsymbol{v} \cdot \boldsymbol{n}_E)\boldsymbol{n}_E$ denotes the normal component of the vector $\boldsymbol{v}$ on the facet E, whose normal direction is $\boldsymbol{n}_E$. Note that the covariant mapping is used to define the $H(\mathrm{curl})$-conforming vector space $\boldsymbol{V}_h^{k,s}$, which will be used

to approximate the structure displacement and velocity, and the Piola mapping is used to define the hybrid Lagrange multiplier space $\widetilde{\boldsymbol{V}}_h^{k,s}$, which will be used to approximate the normal component of structure velocity on the mesh skeleton. Moreover, the doubly Piola mapping is used to define the symmetric tensor space $\boldsymbol{\Sigma}_h^{k,s}$, which will be used to approximate the symmetric stress tensor $\boldsymbol{P}_{\rm sym}$, and the doubly covariant mapping is used to define the symmetric tensor space $\boldsymbol{\Lambda}_h^{k,s}$, which will be used to approximate the symmetric deformation tensor $\boldsymbol{F}_{\rm sym}$. The doubly Piola mapping is a nature choice for $\boldsymbol{P}_{\rm sym}$ for the re-enforcement of the normal-normal inter-element continuity, and the doubly covariant mapping for $\boldsymbol{F}_{\rm sym}$ was motivated in [62] to ensure that $\boldsymbol{F}_{\rm sym}$ and the gradient $\nabla \boldsymbol{d}$ are mapped in the same way from the reference element to a physical element.

3.3. The TDNNS scheme: spatial discretization. In this subsection, we focus on the spatial discretization of the equations (22) with homogeneous Dirichlet boundary conditions

$$\boldsymbol{d}(\mathbf{x},t)=\boldsymbol{u}^s(\mathbf{x},t)=0,\quad \forall \mathbf{x}\in\partial\Omega^s,\quad t\in[0,T]. \tag{24}$$

We use polynomials of degree $k\geq 1$ for all the variables. The spatial HDG discretization reads as follows: Find $(\boldsymbol{P}_{{\rm sym},h},\boldsymbol{F}_{{\rm sym},h},\boldsymbol{u}_h^s,,\widetilde{\boldsymbol{u}}_h^s)\in \boldsymbol{\Sigma}_h^{k,s}\times\boldsymbol{\Lambda}_h^{k,s}\times \boldsymbol{V}_h^{k,s}\times\widetilde{\boldsymbol{V}}_h^{k,s}$ with $\mathsf{tng}(\boldsymbol{u}_h^s)|_{\partial\Omega^s}=0, \mathsf{nrm}(\widetilde{\boldsymbol{u}}_h^s)|_{\partial\Omega^s}=0$, such that

$$\begin{aligned}\left(\rho^s\frac{\partial \boldsymbol{u}_h^s}{\partial t},\boldsymbol{v}_h^s\right)_{\mathcal{T}_h^s}+(\boldsymbol{P}_{{\rm sym},h},\nabla\boldsymbol{v}_h^s)_{\mathcal{T}_h^s}&\\ -\langle \boldsymbol{P}_{{\rm sym},h}\boldsymbol{n},\ \mathsf{nrm}(\boldsymbol{v}_h^s)\rangle_{\partial\mathcal{T}_h^s}+\left(\frac{\partial\Psi(\boldsymbol{F}_h)}{\partial\boldsymbol{F}},(\nabla\boldsymbol{v}_h^s)_{\rm skw}\right)_{\mathcal{T}_h^s}&=(\rho^s\boldsymbol{f}^s,\boldsymbol{\xi})_{\mathcal{T}_h^s},\end{aligned} \tag{25a}$$

$$\left(\frac{\partial\Psi(\boldsymbol{F}_h)}{\partial\boldsymbol{F}}-\boldsymbol{P}_{{\rm sym},h},\boldsymbol{G}_h\right)_{\mathcal{T}_h^s}=0, \tag{25b}$$

$$\left(\frac{\partial\boldsymbol{F}_{{\rm sym},h}}{\partial t}-\nabla\boldsymbol{u}_h^s,\boldsymbol{Q}_h\right)_{\mathcal{T}_h^s}+\langle\ \mathsf{nrm}(\boldsymbol{u}_h^s-\widetilde{\boldsymbol{u}}_h^s),\boldsymbol{Q}_h\boldsymbol{n}\rangle_{\partial\mathcal{T}_h^s}=0, \tag{25c}$$

$$\langle\boldsymbol{P}_{{\rm sym},h}\boldsymbol{n},\ \mathsf{nrm}(\widetilde{\boldsymbol{v}}_h^s)\rangle_{\partial\mathcal{T}_h^s}=0, \tag{25d}$$

for all $(\boldsymbol{Q}_h,\boldsymbol{G}_h,\boldsymbol{v}_h^s,\widetilde{\boldsymbol{v}}_h^s)\in\boldsymbol{\Sigma}_h^{k,s}\times\boldsymbol{\Lambda}_h^{k,s}\times\boldsymbol{V}_h^{k,s}\times\widetilde{\boldsymbol{V}}_h^{k,s}$ with $\mathsf{tng}(\boldsymbol{v}_h^s)|_{\partial\Omega^s}=\mathsf{nrm}(\widetilde{\boldsymbol{v}}_h^s)|_{\partial\Omega^s}=0$, where the full deformation gradient

$$\boldsymbol{F}_h:=\boldsymbol{F}_{{\rm sym},h}+(\nabla\boldsymbol{d}_h)_{\rm skw}, \tag{25e}$$

and the displacement field $\boldsymbol{d}_h\in\boldsymbol{V}_h^{k,s}$ satisfies

$$\frac{\partial\boldsymbol{d}_h}{\partial t}=\boldsymbol{u}_h^s \tag{25f}$$

We note that due to $H(\mathrm{curl})$-conformity of the space $\boldsymbol{V}_h^{k,s}$, the skew symmetric tensor $(\nabla\boldsymbol{d}_h)_{\rm skw}$, which has a one-to-one correspondence to the curl operator, is a regular L^2-conforming function. When restricted to elastostatics problems, the above variational scheme (25) is precisely the $\boldsymbol{F}$-based TDNNS scheme introduced in [62], which was formulated as an optimization problem of a saddle point Lagrangian.

To further simplify the notation, we denote the compound space and variables

$$\underline{\boldsymbol{X}}_h^{k,s}:=\boldsymbol{\Sigma}_h^{k,s}\times\boldsymbol{\Lambda}_h^{k,s}\times\boldsymbol{V}_h^{k,s}\times\widetilde{\boldsymbol{V}}_h^{k,s},$$

$$\underline{U}_h^s:=(\boldsymbol{P}_{{\rm sym},h},\boldsymbol{F}_{{\rm sym},h},\boldsymbol{u}_h^s,\widetilde{\boldsymbol{u}}_h^s)\in\underline{\boldsymbol{X}}_h^{k,s},\quad \underline{V}_h^s:=(\boldsymbol{Q}_h,\boldsymbol{G}_h,\boldsymbol{v}_h^s,\widetilde{\boldsymbol{v}}_h^s)\in\underline{\boldsymbol{X}}_h^{k,s},$$

and introduce the following operators:

$$\mathcal{M}_h^s\left(\underline{U}_h^s,\underline{V}_h^s\right) := (\rho^s \boldsymbol{u}_h^s, \boldsymbol{v}_h^s)_{\mathcal{T}_h^s} + (\boldsymbol{F}_{\mathrm{sym},h}, \boldsymbol{Q}_h)_{\mathcal{T}_h^s}\,, \tag{26a}$$

$$\begin{aligned}\mathcal{A}_h^s\left(\underline{U}_h^s,\underline{V}_h^s\right) :=\ & (\boldsymbol{P}_{\mathrm{sym},h}, \nabla \boldsymbol{v}_h^s)_{\mathcal{T}_h^s} - \langle \boldsymbol{P}_{\mathrm{sym},h}\boldsymbol{n},\ \mathsf{nrm}(\boldsymbol{v}_h^s - \widetilde{\boldsymbol{v}}_h^s)\rangle_{\partial\mathcal{T}_h^s} \\ & + \left(\frac{\partial \Psi(\boldsymbol{F}_h)}{\partial \boldsymbol{F}}, (\nabla \boldsymbol{v}_h^s)_{\mathrm{skw}} + \boldsymbol{G}_h\right)_{\mathcal{T}_h^s} - (\boldsymbol{P}_{\mathrm{sym},h}, \boldsymbol{G}_h)_{\mathcal{T}_h^s} \\ & - (\nabla \boldsymbol{u}_h^s, \boldsymbol{Q}_h)_{\mathcal{T}_h^s} + \langle\ \mathsf{nrm}(\boldsymbol{u}_h^s - \widetilde{\boldsymbol{u}}_h^s), \boldsymbol{Q}_h\boldsymbol{n}\rangle_{\partial\mathcal{T}_h^s}\,,\end{aligned} \tag{26b}$$

$$\mathcal{F}_h^s(\underline{V}_h^s) := (\rho^s \boldsymbol{f}^s, \boldsymbol{v}_h^s)_{\mathcal{T}_h^s}\,. \tag{26c}$$

Then the scheme (25) can be expressed as the following compact form: find $\underline{U}_h^s \in \underline{\boldsymbol{X}}_h^{k,s}$ with $\mathsf{tng}(\boldsymbol{u}_h^s)|_{\partial\Omega^s} = \mathsf{nrm}(\widetilde{\boldsymbol{u}}_h^s)|_{\partial\Omega^s} = 0$, such that

$$\mathcal{M}_h^s\left(\frac{\partial \underline{U}_h^s}{\partial t}, \underline{V}_h^s\right) + \mathcal{A}_h^s\left(\underline{U}_h^s,\underline{V}_h^s\right) = \mathcal{F}_h^s(\underline{V}_h^s), \tag{27}$$

for all $\underline{V}_h^s \in \underline{\boldsymbol{X}}_h^{k,s}$ with $\mathsf{tng}(\boldsymbol{v}_h^s)|_{\partial\Omega^s} = \mathsf{nrm}(\widetilde{\boldsymbol{v}}_h^s)|_{\partial\Omega^s} = 0$, where $\boldsymbol{F}_h$ in (26b) is given by equation (25e), with the displacement $\boldsymbol{d}_h$ determined through equation (25f).

We have the following energy stability result of the scheme (25).

Theorem 3.1. *Let* $(\boldsymbol{P}_h, \boldsymbol{F}_h, \boldsymbol{u}_h^s, , \widetilde{\boldsymbol{u}}_h^s) \in \boldsymbol{\Sigma}_h^{k,s} \times \boldsymbol{\Lambda}_h^{k,s} \times \boldsymbol{V}_h^{k,s} \times \widetilde{\boldsymbol{V}}_h^{k,s}$ *be the solution to the scheme* (25)*. Then the following energy identity holds:*

$$\frac{d}{dt}\mathsf{E}_h^s = \left(\rho^f \boldsymbol{f}^s, \boldsymbol{u}_h^s\right)_{\mathcal{T}_h^s}\,,$$

where the elastic energy

$$\mathsf{E}_h^s := \frac{1}{2}\left(\rho^s \boldsymbol{u}_h^s, \boldsymbol{u}_h^s\right)_{\mathcal{T}_h^s} + \left(\Psi(\boldsymbol{F}_h), 1\right)_{\mathcal{T}_h^s} \tag{28}$$

Proof. Taking the test functions $(\boldsymbol{Q}_h, \boldsymbol{G}_h, \boldsymbol{v}_h^s, \widetilde{\boldsymbol{v}}_h^s) = (\boldsymbol{P}_{\mathrm{sym},h}, \frac{\partial \boldsymbol{F}_{\mathrm{sym},h}}{\partial t}, \boldsymbol{u}_h^s, \widetilde{\boldsymbol{u}}_h^s)$ in the scheme (25) and adding, we get

$$\frac{1}{2}\frac{d}{dt}\left(\rho^s \boldsymbol{u}_h^s, \boldsymbol{u}_h^s\right)_{\mathcal{T}_h^s} + \left(\frac{\partial \Psi(\boldsymbol{F}_h)}{\partial \boldsymbol{F}}, \frac{\partial \boldsymbol{F}_{\mathrm{sym},h}}{\partial t} + (\nabla \boldsymbol{u}_h^s)_{\mathrm{skw}}\right)_{\mathcal{T}_h^s} = \left(\rho^s \boldsymbol{f}^s, \boldsymbol{u}_h^s\right)_{\mathcal{T}_h^s}\,.$$

By the equalities (25e)–(25f), we have

$$\frac{\partial \boldsymbol{F}_h}{\partial t} = \frac{\partial \boldsymbol{F}_{\mathrm{sym},h}}{\partial t} + (\nabla \boldsymbol{u}_h^s)_{\mathrm{skw}}.$$

Hence,

$$\left(\rho^s \boldsymbol{f}^s, \boldsymbol{u}_h^s\right)_{\mathcal{T}_h^s} = \frac{1}{2}\frac{d}{dt}\left(\rho^s \boldsymbol{u}_h^s, \boldsymbol{u}_h^s\right)_{\mathcal{T}_h^s} + \left(\frac{\partial \Psi(\boldsymbol{F}_h)}{\partial \boldsymbol{F}}, \frac{\partial \boldsymbol{F}_h}{\partial t}\right)_{\mathcal{T}_h^s} = \frac{d}{dt}\mathsf{E}_h^s,$$

which concludes the proof. □

Remark 3.1 (reduced TDNNS schemes)**.** *When applied to linear elasostatics problems, the TDNNS scheme* (25) *was proven [69] to provide optimal convergence of order* k *in the* $H(\mathrm{div}\,\mathrm{div})$*-norm for the symmetric stress* $\boldsymbol{P}_{\mathrm{sym},h}$ *and the* $H(\mathrm{curl})$*-norm of the displacement* $\boldsymbol{d}_h$*. However, the* L^2*-convergence rate in the symmetric stress was also proven [67] to be of order* k*, which is numerically verified to be sharp and is suboptimal as the space contains the whole polynomials of degree* k *on each element. The work [67] suggests to reduce the local symmetric stress space*

such that its normal-normal component on the element boundary is a polynomial of degree $\max(1, k-1)$*:*

$$\boldsymbol{\Sigma}_h^{k,\mathrm{red}} := \{\boldsymbol{\sigma} \in \boldsymbol{\Sigma}_h^{k,s} : \quad (\boldsymbol{\sigma}\boldsymbol{n}) \cdot \boldsymbol{n}|_E \in \mathcal{P}^{\max(1,k-1)}(E), \quad \forall E \in \mathcal{E}_h^s\} \tag{29}$$

The companion Lagrange multiplier space for $\boldsymbol{\Sigma}_h^{k,\mathrm{red}}$ *is then* $\widetilde{\boldsymbol{V}}_h^{\max(1,k-1),s}$*. The reduced TDNNS scheme uses* $\boldsymbol{\Sigma}_h^{k,\mathrm{red}}$ *for* $\boldsymbol{P}_{\mathrm{sym},h}$ *and* $\widetilde{\boldsymbol{V}}_h^{\max(1,k-1),s}$ *for* $\widetilde{\boldsymbol{u}}_h^s$*, which enjoys the same convergence rates as the original TDNNS scheme with a reduced computational cost whose globally coupled DOFs consist of those in* $\boldsymbol{V}_h^{k,s}$ *and* $\widetilde{\boldsymbol{V}}_h^{\max(1,k-1),s}$ *on the mesh skeleton. The order* k *convergence in* L^2 *norm for the symmetric stress is sharp for* $k \geq 2$ *for this reduced TDNNS scheme as the associated space contains full polynomials of degree* $k-1$ *but not of degree* k*.*

In two dimensions, [67] also suggests a non-conforming reduced TDNNS scheme such that the displacement space $\boldsymbol{V}_h^{k,s}$ *is replaced by an* $H(\mathrm{curl})$*-non-conforming space* $\boldsymbol{V}_h^{k,nc}$ *which has the same local polynomial space of degree* k *as* $\boldsymbol{V}_h^{k,s}$ *in each element, but leaves the highest order edge basis function discontinuous across element edges. The space* $\boldsymbol{V}_h^{k,nc}$ *consists of less globally coupled DOFs, and more internal DOFs which can be eliminated locally. The non-conforming reduced TDNNS scheme was also proven to provide the same convergence rates as the original TDNNS scheme, with a further reduced computational cost. We note that this non-conforming approach does not extend to three dimensions. We will numerical exam the convergence behavior of the original TDNNS scheme* (25) *and the non-conforming reduced TDNNS scheme, whose approximation spaces are*

$$\boldsymbol{\Sigma}_h^{k,\mathrm{red}} \times \boldsymbol{\Lambda}_h^{k,s} \times \boldsymbol{V}_h^{k,nc} \times \widetilde{\boldsymbol{V}}_h^{\max(1,k-1),s}, \tag{30}$$

for nonlinear elasticity in two dimensions in the numerical results section.

3.4. The TDNNS scheme: temporal discretization. Since the semidiscrete scheme (25) is constructed in the Lagrangian framework on a fixed domain, a standard method-of-lines approach can be readily used to discretize the time derivatives. In particular, the BDF[m] temporal discretization is obtained from the scheme (25) by replacing the time derivative terms in (25a), (25c), and (25f) by the corresponding BDF approximations:

$$\mathbb{D}_t^m \boldsymbol{\phi}_h^n := \frac{\sum_{j=0}^m b_j^m \boldsymbol{\phi}_h^{n-j}}{\Delta t}, \tag{31}$$

where the BDF coefficients b_j^m are given in Table 1.

4. HDG for FSI: coupling and mesh movement

In this section, we introduce partitioned and monolithic FSI solvers by combing the ALE divergence-free HDG scheme for fluids in Section 2 and the TDNNS scheme for structure in Section 3. We mainly focus on the proper treatment of the fluid-structure interface, and the construction of the ALE map in the fluid domain.

4.1. The FSI problem. We consider the interaction between an incompressible viscous fluid and an elastic structure. We use the same notation as the previous two sections. In particular, the Navier-Stokes equations (8) is considered on the (moving) fluid domain Ω_t^f, and the equations of nonlinear hypreelasticity (21) is considered on the reference structure domain Ω^s. We denote $\Gamma_0 = \Omega_0^f \cap \Omega^s$ as the fluid-structure interface in the initial configuration, and denote $\Gamma_t = \boldsymbol{\phi}_t(\Gamma_0)$ as

the deformed interface. The equations (8) and (21) are equiped with the following coupling and boundary conditions:

$$\boldsymbol{u}^f = \boldsymbol{u}^s \circ (\boldsymbol{\phi}_t)^{-1} \quad \text{on } \Gamma_t, \tag{32a}$$

$$(\boldsymbol{P}\boldsymbol{n}^s) \circ (\boldsymbol{\phi}_t)^{-1} = -J_b \boldsymbol{\sigma}^f \boldsymbol{n}^f \quad \text{on } \Gamma_t, \tag{32b}$$

$$\boldsymbol{u}^f = 0 \quad \text{on } \partial\Omega_t^f \backslash \Gamma_t, \tag{32c}$$

$$\boldsymbol{d} = \boldsymbol{u}^s = 0 \quad \text{on } \partial\Omega^s \backslash \Gamma_0, \tag{32d}$$

where $\boldsymbol{n}^f$ is the outward normal direction on the deformed interface Γ_t from the fluid domain Ω_t^f, $\boldsymbol{n}^s$ is the outward normal direction on the initial interface Γ_0 from the structure domain Ω^s, and J_b is the surface Jacobian of the mapping from Γ_0 to Γ_t.

4.2. Semidiscrete scheme: a generalized Robin interface condition treatment. The key to an efficient partitioned FSI solver is the proper treatment of the interface conditions (32a) and (32b). It is well-known that the classical Dirichlet-Neumann interface condition treatment, where (32a) serves as the Dirichlet boundary condition for the fluid and (32b) as the Neumann boundary condition for the structure, suffers from stability issues due to the so-called added mass effects when it is used in a partitioned FSI solver when the fluid and structure have similar densities. To make the overall scheme robust for partitioned FSI solvers, we follow the novel ideas in [8, 13, 15, 79] to implement the interface conditions as the following set of transmission conditions of Robin type:

$$\alpha \boldsymbol{u}^f + \boldsymbol{\sigma}^f \boldsymbol{n}^f = \alpha \boldsymbol{u}^s \circ (\boldsymbol{\phi}_t)^{-1} + \boldsymbol{\sigma}^{f,*} \boldsymbol{n}^f \quad \text{on } \Gamma_t, \tag{33a}$$

$$(\alpha J_b \boldsymbol{u}^s + \boldsymbol{P}\boldsymbol{n}^s) \circ (\boldsymbol{\phi}_t)^{-1} = \alpha J_b \boldsymbol{u}^{f,*} - J_b \boldsymbol{\sigma}^{f,*} \boldsymbol{n}^f \quad \text{on } \Gamma_t, \tag{33b}$$

where $\alpha > 0$ is a combination parameter, and $\boldsymbol{u}^{f,*}$ and $\boldsymbol{\sigma}^{f,*}$ are proper approximations to the fluid velocity and fluid stress to be specified later. We further denote

$$\underline{U}_h^{f,*} := (p_h^{f,*}, \boldsymbol{\epsilon}_h^{f,*}, \boldsymbol{u}_h^{f,*}, \widetilde{\sigma}_h^{f,*}, \widetilde{\boldsymbol{u}}_h^{f,*}) \in \underline{\boldsymbol{X}}_h^{k,f}$$

to be an approximation of $\underline{U}_h^f$. Here (33a) is used as a Robin boundary condition for the fluid, and (33b) is used as a Robin boundary condition for the solid. We note that in a fully discrete scheme, taking $\underline{U}_h^{f,*}$ to be extrapolations of data from previous time steps would lead to a loosely coupled partitioned scheme, while taking $\underline{U}_h^{f,*}$ to be the unknonws $\underline{U}_h^f$ would lead to a fully coupled monolithlic scheme. Details of the choices for $\underline{U}_h^{f,*}$ will be discussed in the next subsection.

To simplify the notation, we define the following quantities on the interface Γ_0:

$$\overline{\boldsymbol{u}_h^s} := \mathsf{tng}(\boldsymbol{u}_h^s) + \mathsf{nrm}(\widetilde{\boldsymbol{u}}_h^s), \quad \overline{\boldsymbol{v}_h^s} := \mathsf{tng}(\boldsymbol{v}_h^s) + \mathsf{nrm}(\widetilde{\boldsymbol{v}}_h^s),$$

where $\overline{\boldsymbol{u}_h^s}$ is the effective structure velocity on the interface Γ_0. The spatial discretization of the fluid with boundary conditions (32c) and (33a) is adapted from (15) and is given as follows: find $\underline{U}_h^f \in \underline{\boldsymbol{X}}_h^{k,f}$ with $\widetilde{\boldsymbol{u}}_h^f|_{\partial\Omega^f \backslash \Gamma_t} = 0$ such that

$$\mathcal{M}_h^f\Big(\frac{\partial \underline{U}_h^f}{\partial t}\Big|_{\mathbf{x}_0}, \underline{V}_h^f\Big) + \mathcal{C}_h^f\left(\boldsymbol{u}_h^f - \boldsymbol{\omega}^f; \underline{U}_h^f, \underline{V}_h^f\right) + \mathcal{A}_h^f\left(\underline{U}_h^f, \underline{V}_h^f\right) + \mathcal{J}_h^{f,R}((\underline{U}_h^f, \underline{U}_h^{f,*}, \underline{U}_h^s), \underline{V}_h^f) = \mathcal{F}_h^f(\underline{V}_h^f), \tag{34}$$

for all $\underline{V}_h^f \in \underline{\boldsymbol{X}}_h^{k,f}$ with $\widetilde{\boldsymbol{v}}_h^f|_{\partial\Omega^f\setminus\Gamma_t} = 0$, where the interface operator

(35)
$$\begin{aligned}\mathcal{I}_h^{f,R}((\underline{U}_h^f,\underline{U}_h^{f,*},\underline{U}_h^s),\underline{V}_h^f) :=& \left\langle \frac{1}{\alpha}(\widetilde{\sigma}_h^f - \widetilde{\sigma}_h^{f,*}) - \overline{\boldsymbol{u}_h^s}\circ(\boldsymbol{\phi}_t)^{-1}\cdot\boldsymbol{n}^f, \widetilde{\tau}_h^f\right\rangle_{\Gamma_t}\\ &+ \left\langle \alpha\mathsf{tng}\left(\widetilde{\boldsymbol{u}}_h^f - \overline{\boldsymbol{u}_h^s}\circ(\boldsymbol{\phi}_t)^{-1}\right) - 2\mu^f\mathsf{tng}(\boldsymbol{\epsilon}_h^{f,*}\boldsymbol{n}^f), \mathsf{tng}(\widetilde{\boldsymbol{v}}_h^f)\right\rangle_{\Gamma_t}\\ &+ \left\langle \alpha\left(\boldsymbol{u}_h^f - \overline{\boldsymbol{u}_h^s}\circ(\boldsymbol{\phi}_t)^{-1}\right)\cdot\boldsymbol{n}^f + (\widetilde{\sigma}_h^f - \widetilde{\sigma}_h^{f,*}), \boldsymbol{v}_h^f\cdot\boldsymbol{n}^f\right\rangle_{\Gamma_t}\\ &+ \left\langle \mathsf{tng}\left(\widetilde{\boldsymbol{u}}_h^f - \overline{\boldsymbol{u}_h^s}\circ(\boldsymbol{\phi}_t)^{-1}\right) + \frac{1}{\alpha}2\mu^f\mathsf{tng}(\boldsymbol{\epsilon}_h^f\boldsymbol{n}^f - \boldsymbol{\epsilon}_h^{f,*}\boldsymbol{n}^f), 2\mu^f\mathsf{tng}(\boldsymbol{G}\boldsymbol{n}^f)\right\rangle_{\Gamma_t},\end{aligned}$$

where the first two terms are obtained from the Robin boundary condition (33a) in the normal and tangential directions, respective, and the last two terms are consist terms that enhance the stability of the overall scheme.

The spatial discretization of the solid with boundary conditions (32d) and (33b) is adapted from (27) and is given as follows: find $\underline{U}_h^s \in \underline{\boldsymbol{X}}_h^{k,s}$ with $\mathsf{tng}(\boldsymbol{u}_h^s)|_{\partial\Omega^f\setminus\Gamma_t} = 0$ and $\mathsf{nrm}(\widetilde{\boldsymbol{u}}_h^s)|_{\partial\Omega^f\setminus\Gamma_t} = 0$ such that

$$\mathcal{M}_h^s\left(\frac{\partial\underline{U}_h^s}{\partial t}, \underline{V}_h^s\right) + \mathcal{A}_h^s(\underline{U}_h^s, \underline{V}_h^s) + \mathcal{I}_h^{s,R}((\underline{U}_h^{f,*},\underline{U}_h^s),\underline{V}_h^s) = \mathcal{F}_h^s(\underline{V}_h^s), \tag{36}$$

for all $\underline{V}_h^s \in \underline{\boldsymbol{X}}_h^{k,s}$ with $\mathsf{tng}(\boldsymbol{v}_h^s)|_{\partial\Omega^f\setminus\Gamma_t} = 0$ and $\mathsf{nrm}(\widetilde{\boldsymbol{v}}_h^s)|_{\partial\Omega^f\setminus\Gamma_t} = 0$, where the interface operator

(37)
$$\begin{aligned}\mathcal{I}_h^{s,R}((\underline{U}_h^{f,*},\underline{U}_h^s),\underline{V}_h^s) :=& \left\langle \widetilde{\sigma}_h^{f,*}\boldsymbol{n}^f + 2\mu^f\mathsf{tng}(\boldsymbol{\epsilon}_h^{f,*}\boldsymbol{n}^f), \overline{\boldsymbol{v}_h^s}\circ(\boldsymbol{\phi}_t)^{-1}\right\rangle_{\Gamma_t}\\ &+ \left\langle \alpha\left(\overline{\boldsymbol{u}_h^s}\circ(\boldsymbol{\phi}_t)^{-1} - \mathsf{nrm}(\boldsymbol{u}_h^{f,*}) - \mathsf{tng}(\widetilde{\boldsymbol{u}}_h^{f,*})\right), \overline{\boldsymbol{v}_h^s}\circ(\boldsymbol{\phi}_t)^{-1}\right\rangle_{\Gamma_t}\end{aligned}$$

is obtained from the Robin boundary condition (33b).

Stability of the coupled scheme (34)–(36) is documented in the following result.

Theorem 4.1. *Let $\underline{U}_h^f \in \underline{\boldsymbol{X}}_h^{k,f}$ and $\underline{U}_h^s \in \underline{\boldsymbol{X}}_h^{k,s}$ be the solution to the semi-discrete coupled scheme* (34)–(36)*. Then there holds*

(38)
$$\begin{aligned}&\frac{\partial}{\partial t}\left(\frac{1}{2}\left(\rho^f\boldsymbol{u}_h^f,\boldsymbol{u}_h^f\right)_{\mathcal{T}_h^{f,t}} + \mathsf{E}_h^s\right) + 2\mu^f\left(\boldsymbol{\epsilon}_h^f,\boldsymbol{\epsilon}_h^f\right)_{\mathcal{T}_h^{f,t}} + \left\langle\gamma_h\left|\mathsf{tng}\left(\boldsymbol{u}_h^f - \widetilde{\boldsymbol{u}}_h^f\right)\right|^2, 1\right\rangle_{\partial\mathcal{T}_h^{f,t}}\\ &+ I_h(\underline{U}_h^f) + D_h(\underline{U}_h^f,\underline{U}_h^{f,*},\underline{U}_h^s) = \mathcal{F}_h^f(\underline{V}_h^f) + \mathcal{F}_h^s(\underline{V}_h^s) + I_h(\underline{U}_h^{f,*}),\end{aligned}$$

where the elastic energy E_h^s is given in (28)*,*

$$I_h(\underline{U}_h^f) := \left\langle\frac{1}{2\alpha}\left(|\widetilde{\sigma}_h^f|^2 + |2\mu^f\mathsf{tng}(\boldsymbol{\epsilon}_h^f\boldsymbol{n}^f)|^2\right) + \frac{\alpha}{2}\left(|\boldsymbol{u}_h^f\cdot\boldsymbol{n}^f|^2 + |\mathsf{tng}(\widetilde{\boldsymbol{u}}_h^f)|^2\right), 1\right\rangle_{\Gamma_t}$$

and

$$\begin{aligned}&D_h(\underline{U}_h^f,\underline{U}_h^{f,*},\underline{U}_h^s):\\ =& \left\langle\frac{\alpha}{2}\left(|(\boldsymbol{u}_h^{f,*} - \overline{\boldsymbol{u}_h^s}\circ(\boldsymbol{\phi}_t)^{-1})\cdot\boldsymbol{n}^f|^2 + |\mathsf{tng}(\widetilde{\boldsymbol{u}}_h^{f,*} - \overline{\boldsymbol{u}_h^s}\circ(\boldsymbol{\phi}_t)^{-1})|^2\right), 1\right\rangle_{\Gamma_t}\\ &+ \left\langle\frac{1}{2\alpha}|\alpha\mathsf{tng}(\widetilde{\boldsymbol{u}}_h^f - \overline{\boldsymbol{u}_h^s}\circ(\boldsymbol{\phi}_t)^{-1}) + 2\mu^f\mathsf{tng}(\boldsymbol{\epsilon}_h^f\boldsymbol{n}^f - \boldsymbol{\epsilon}_h^{f,*}\boldsymbol{n}^f)|^2, 1\right\rangle_{\Gamma_t}\\ &+ \left\langle\frac{1}{2\alpha}|\alpha(\boldsymbol{u}_h^f - \overline{\boldsymbol{u}_h^s}\circ(\boldsymbol{\phi}_t)^{-1})\cdot\boldsymbol{n}^f + (\widetilde{\sigma}_h^f - \widetilde{\sigma}_h^{f,*})|^2, 1\right\rangle_{\Gamma_t}\end{aligned}$$

Proof. With an abuse of notation, we denote $\overline{\boldsymbol{u}_h^s} := \overline{\boldsymbol{u}_h^s} \circ (\boldsymbol{\phi}_t)^{-1}$ as the structure velocity on the deformed interface Γ_t. By definition, we have

$$\mathcal{I}_h^{f,R}((\underline{U}_h^f, \underline{U}_h^{f,*}, \underline{U}_h^s), \underline{U}_h^f) + \mathcal{I}_h^{f,R}((\underline{U}_h^{f,*}, \underline{U}_h^s), \underline{U}_h^s) = I_n + I_t,$$

where

$$\begin{aligned} I_n = &\left\langle \frac{1}{\alpha}(\widetilde{\sigma}_h^f - \widetilde{\sigma}_h^{f,*}), \widetilde{\sigma}_h^f \right\rangle_{\Gamma_t} + \left\langle \alpha \left(\boldsymbol{u}_h^f - \overline{\boldsymbol{u}_h^s} \right) \cdot \boldsymbol{n}^f, \boldsymbol{u}_h^f \cdot \boldsymbol{n}^f \right\rangle_{\Gamma_t} \\ &+ \left\langle (\widetilde{\sigma}_h^f - \widetilde{\sigma}_h^{f,*}), (\boldsymbol{u}_h^f - \overline{\boldsymbol{u}_h^s}) \cdot \boldsymbol{n}^f \right\rangle_{\Gamma_t} + \left\langle \alpha \left(\overline{\boldsymbol{u}_h^s} - \boldsymbol{u}_h^{f,*} \right) \cdot \boldsymbol{n}^f, \overline{\boldsymbol{u}_h^s} \cdot \boldsymbol{n}^f \right\rangle_{\Gamma_t}, \end{aligned}$$

and

$$\begin{aligned} I_t = &\left\langle \frac{1}{\alpha} 2\mu^f \mathsf{tng}(\boldsymbol{\epsilon}_h^f \boldsymbol{n}^f - \boldsymbol{\epsilon}_h^{f,*} \boldsymbol{n}^f), 2\mu^f \mathsf{tng}(\boldsymbol{\epsilon}_h^f \boldsymbol{n}^f) \right\rangle_{\Gamma_t} + \left\langle \alpha \mathsf{tng} \left(\widetilde{\boldsymbol{u}}_h^f - \overline{\boldsymbol{u}_h^s} \right), \mathsf{tng}(\widetilde{\boldsymbol{u}}_h^f) \right\rangle_{\Gamma_t} \\ &+ \left\langle 2\mu^f \mathsf{tng}(\boldsymbol{\epsilon}_h^f \boldsymbol{n}^f - \boldsymbol{\epsilon}_h^{f,*} \boldsymbol{n}^f), \mathsf{tng}(\widetilde{\boldsymbol{u}}_h^f - \overline{\boldsymbol{u}_h^s}) \right\rangle_{\Gamma_t} + \left\langle \alpha \mathsf{tng} \left(\overline{\boldsymbol{u}_h^s} - \widetilde{\boldsymbol{u}}_h^{f,*} \right), \mathsf{tng}(\overline{\boldsymbol{u}_h^s}) \right\rangle_{\Gamma_t}. \end{aligned}$$

The terms I_n and I_t can be treated in a similar way. In particular, after some algebraic manipulation, there holds

$$\begin{aligned} I_n = &\left\langle \frac{1}{2\alpha} |\widetilde{\sigma}_h^f|^2 + \frac{\alpha}{2} |\boldsymbol{u}_h^f \cdot \boldsymbol{n}^f|^2, 1 \right\rangle_{\Gamma_t} - \left\langle \frac{1}{2\alpha} |\widetilde{\sigma}_h^{f,*}|^2 + \frac{\alpha}{2} |\boldsymbol{u}_h^{f,*} \cdot \boldsymbol{n}^f|^2, 1 \right\rangle_{\Gamma_t} \\ &+ \left\langle \frac{\alpha}{2} |(\overline{\boldsymbol{u}_h^s} - \boldsymbol{u}_h^{f,*}) \cdot \boldsymbol{n}^f|^2, 1 \right\rangle_{\Gamma_t} + \left\langle \frac{1}{2\alpha} |\alpha(\boldsymbol{u}_h^f - \overline{\boldsymbol{u}_h^s}) \cdot \boldsymbol{n}^f + (\widetilde{\sigma}_h^f - \widetilde{\sigma}_h^{f,*})|^2, 1 \right\rangle_{\Gamma_t}, \end{aligned}$$

and

$$\begin{aligned} I_t = &\left\langle \frac{1}{2\alpha} |2\mu^f \mathsf{tng}(\boldsymbol{\epsilon}_h^f \boldsymbol{n}^f)|^2 + \frac{\alpha}{2} |\mathsf{tng}(\widetilde{\boldsymbol{u}}_h^f)|^2, 1 \right\rangle_{\Gamma_t} - \left\langle \frac{1}{2\alpha} |2\mu^f \mathsf{tng}(\boldsymbol{\epsilon}_h^{f,*} \boldsymbol{n}^f)|^2 + \frac{\alpha}{2} |\mathsf{tng}(\widetilde{\boldsymbol{u}}_h^{f,*})|^2, 1 \right\rangle_{\Gamma_t} \\ &+ \left\langle \frac{\alpha}{2} |\mathsf{tng}(\overline{\boldsymbol{u}_h^s} - \widetilde{\boldsymbol{u}}_h^{f,*})|^2, 1 \right\rangle_{\Gamma_t} + \left\langle \frac{1}{2\alpha} |\alpha \mathsf{tng}(\widetilde{\boldsymbol{u}}_h^f - \overline{\boldsymbol{u}_h^s}) + 2\mu^f \mathsf{tng}(\boldsymbol{\epsilon}_h^f \boldsymbol{n}^f - \boldsymbol{\epsilon}_h^{f,*} \boldsymbol{n}^f)|^2, 1 \right\rangle_{\Gamma_t}. \end{aligned}$$

Combining these identities with the stability results in Theorem 2.1 and Theorem 3.1, we conclude the proof. □

4.3. Fully discrete schemes: monolithic and partitioned approaches. Following the previous two sections, we consider a BDF[m] temporal discretization. The fully discrete scheme is obtained from the equations (34) –(36) by replacing the time derivative terms using the corresponding BDF[m] discretizations (18) and (31): find $\underline{U}_h^f \in \underline{\boldsymbol{X}}_h^{k,f}$ with $\widetilde{\boldsymbol{u}}_h^f|_{\partial\Omega^f \setminus \Gamma_t} = 0$ and $\underline{U}_h^s \in \underline{\boldsymbol{X}}_h^{k,s}$ with $\mathsf{tng}(\boldsymbol{u}_h^s)|_{\partial\Omega^f \setminus \Gamma_t} = 0$ and $\mathsf{nrm}(\widetilde{\boldsymbol{u}}_h^s)|_{\partial\Omega^f \setminus \Gamma_t} = 0$ such that

$$\begin{aligned} &\mathcal{M}_h^f(D_t^m \underline{U}_h^{f,n}, \underline{V}_h^f) + \mathcal{C}_h^f \left(\boldsymbol{u}_h^{f,n} - \boldsymbol{\omega}^f; \underline{U}_h^f, \underline{V}_h^f \right) + \mathcal{A}_h^f \left(\underline{U}_h^{f,n}, \underline{V}_h^f \right) \\ &\qquad + \mathcal{I}_h^{f,R}((\underline{U}_h^{f,n}, \underline{U}_h^{f,n,*}, \underline{U}_h^{s,n}), \underline{V}_h^f) = \mathcal{F}_h^f(\underline{V}_h^f), \end{aligned} \tag{39a}$$

$$\mathcal{M}_h^s(\mathbb{D}_t^m \underline{U}_h^{s,n}, \underline{V}_h^s) + \mathcal{A}_h^s(\underline{U}_h^{s,n}, \underline{V}_h^s) + \mathcal{I}_h^{s,R}((\underline{U}_h^{f,n,*}, \underline{U}_h^{s,n}), \underline{V}_h^s) = \mathcal{F}_h^s(\underline{V}_h^s), \tag{39b}$$

for all $\underline{V}_h^f \in \underline{\boldsymbol{X}}_h^{k,f}$ with $\widetilde{\boldsymbol{v}}_h^f|_{\partial\Omega^f \setminus \Gamma_t} = 0$, and $\underline{V}_h^s \in \underline{\boldsymbol{X}}_h^{k,s}$ with $\mathsf{tng}(\boldsymbol{v}_h^s)|_{\partial\Omega^f \setminus \Gamma_t} = 0$ and $\mathsf{nrm}(\widetilde{\boldsymbol{v}}_h^s)|_{\partial\Omega^f \setminus \Gamma_t} = 0$, with the structure displacement given by

$$\mathbb{D}_t^m \boldsymbol{d}_h^n = \boldsymbol{u}_h^{s,n}. \tag{39c}$$

Here the choice of the $*$-variables in (35) and (37) has a strong impact on the efficiency and robustness of the resulting fully discrete scheme. Taking the $*$-variables as the solution unknowns:

$$\underline{U}_h^{f,n,*} := \underline{U}_h^{f,n} \tag{40}$$

leads to a fully coupled monolithic scheme. In this case, the interface conditions (33a) for the fluid simply reduce to a Dirichlet boundary condition $\boldsymbol{u}^f = \boldsymbol{u}^s \circ (\boldsymbol{\phi}_t)^{-1}$, and the associated operator (35) is then a weakly treatment of this Dirichlet boundary condition. On the other hand, taking the $*$-variables as extrapolations of previous data with a matching order:

$$\underline{U}_h^{f,n,*} := \sum_{j=1}^{m} c_j^m \underline{U}_h^{f,n-j}, \tag{41}$$

with the extrapolation coefficients c_j^m given in Table 2, leads to a loosely coupled partitioned scheme where solid and fluid can be solved sequentially by first solving the solid using the extrapolated interface data. The monolithic scheme has a better stability property, while the partitioned scheme can be solved more efficiently in each time step.

In practice, we propose to solve the monolithic scheme (39) with (40) sequentially via a fixed point iteration on the $*$-variables, which lead to a strongly coupled partitioned scheme [36, 88] schematized in the following steps:

Step 1. Predict the structural displacement $\boldsymbol{d}_h$, and fluid solution unknowns $\underline{U}_h^{f,*}$ on the interface Γ_0, using m-th order extrapolations as in (41).

Step 2. Update the fluid mesh configuration using the predicted structural displacement by the ALE mapping in (45) below, and update the mesh velocity using the BDF[m] formula.

Step 3. Solve the structural problem (39b) and (39c) using the predicted fluid solution unknowns.

Step 4. Solve the fluid problem (39a) on the updated fluid mesh using the newly obtained structural solution data.

Step 5. Check for convergence: continue to next time step if converged, otherwise return to Step 3. The convergence is considered satisfied if

$$\min\{e_u^{i+1}, e_{\widetilde{u}}^{i+1}, e_\epsilon^{i+1}, e_{\widetilde{\sigma}}^{i+1}\} \le \eta \tag{42}$$

where

$$e_u^{i+1} := \|\mathsf{u}_h^{i+1,\star} - \mathsf{u}_h^i\|/\|\mathsf{u}_h^{i+1,\star}\|, \quad e_{\widetilde{u}}^{i+1} := \|\widetilde{\mathsf{u}}_h^{i+1,\star} - \widetilde{\mathsf{u}}_h^i\|/\|\widetilde{\mathsf{u}}_h^{i+1,\star}\|,$$
$$e_\epsilon^{i+1} := \|\epsilon_h^{i+1,\star} - \epsilon_h^i\|/\|\epsilon_h^{i+1,\star}\|, \quad e_{\widetilde{\sigma}}^{i+1} := \|\widetilde{\sigma}_h^{i+1,\star} - \widetilde{\sigma}_h^i\|/\|\widetilde{\sigma}_h^{i+1,\star}\|,$$

denote the relative errors in l^2-norm for the coefficient vectors of the fluid velocity $\boldsymbol{u}_h^f$, the tangential fluid velocity $\widetilde{\boldsymbol{u}}_h^f$, the fluid strain rate tensor $\boldsymbol{\epsilon}_h^f$, and the fluid normal stress $\widetilde{\sigma}_h^f$, respectively, at the i-th coupling iteration $(\bullet)^i$ and the newly computed solution $(\bullet)^{i+1,\star}$ from Step 4. The parameter η is a user-defined stopping tolerance.

The convergence of this fixed-point scheme is accelerated via relaxation by the Aitken's Δ^2 method [88]:

$$\begin{aligned}
\boldsymbol{u}_h^{f,i+1} &= \omega_u^i\, \boldsymbol{u}_h^{f,i+1,\star} + (1-\omega_u^i)\boldsymbol{u}_h^{f,i},\\
\widetilde{\boldsymbol{u}}_h^{f,i+1} &= \omega_{\widetilde{u}}^i\, \widetilde{\boldsymbol{u}}_h^{f,i+1,\star} + (1-\omega_{\widetilde{u}}^i)\widetilde{\boldsymbol{u}}_h^{f,i},\\
\boldsymbol{\epsilon}_h^{f,i+1} &= \omega_\epsilon^i\, \boldsymbol{\epsilon}_h^{f,i+1,\star} + (1-\omega_\epsilon^i)\boldsymbol{\epsilon}_h^{f,i},\\
\widetilde{\sigma}_h^{f,i+1} &= \omega_{\widetilde{\sigma}}^i\, \widetilde{\sigma}_h^{f,i+1,\star} + (1-\omega_{\widetilde{\sigma}}^i)\widetilde{\sigma}_h^{f,i},
\end{aligned} \tag{43}$$

where the dynamic relaxation parameters ω are given by:

$$\omega_\bullet^{i+1} = -\omega_\bullet^i \frac{\boldsymbol{r}_\bullet^{i+1} \cdot (\boldsymbol{r}_\bullet^{i+1} - \boldsymbol{r}_\bullet^i)}{\|\boldsymbol{r}_\bullet^{i+1} - \boldsymbol{r}_\bullet^i\|^2}, \quad \text{for } \bullet \in \{u, \widetilde{u}, \epsilon, \widetilde{\sigma}\}, \quad \forall i \ge 0, \tag{44}$$

where we take $\omega_\bullet^0 = 1$ for the first iteration, and $\boldsymbol{r}_\bullet^i := (\bullet)^{i+1,\star} - (\bullet)^i$ is the difference of the coefficient vectors for the solution at i-th coupling iteration and the newly computed solution from Step 4.

We denote the above iterative partitioned algorithm as ALG-SP. The monolithic scheme, denoted as ALG-M, is to replace Step 3–5 in the above algorithm with the fully coupled solver for the system (39a)–(39c) using implicit $*$-variables (40). We note that for both schemes, we treat the geometric nonlinearity explicitly in Step 1-2. Furthermore, we remark that ALG-SP with no sub-iteration is simply the loosely coupled partitioned scheme using extrapolated $*$-values (41), which we denote as ALG-P. When coupled with lowest order BDF[1] time stepping, it has been shown in [13, 79] that a loosely coupled scheme with the same interface treatment as in ALG-P is unconditionally energy stable. However, such stability result does not hold for higher order time discretizations, and the sub-iterations in ALG-SP are numerically observed to greatly enhance the stability of the partitioned scheme ALG-P.

4.4. ALE mapping construction. The last ingredient for an implementable scheme is the construction of the (unknown) ALE map (1), which, ideally, can be used to handle large mesh deformations. Various moving mesh algorithms exist in the literature [80,92]. Here we adopt the nonlinear elasticity model with a mesh-Jacobian-based stiffening proposed in [80]. In particular, we compute the ALE map $\boldsymbol{\phi}_h^n \in \boldsymbol{S}_h^k$ at time t^n such that it satisfies the boundary conditions

$$\boldsymbol{\phi}_h^n(\mathbf{x}_0) = \mathbf{x}_0 + \boldsymbol{d}_h^n(\mathbf{x}_0), \quad \forall \mathbf{x}_0 \in \Gamma_0, \qquad \boldsymbol{\phi}_h^n(\mathbf{x}_0) = \mathbf{x}_0, \quad \forall \mathbf{x}_0 \in \partial\Omega_0^f \backslash \Gamma_0, \tag{45a}$$

and

$$\left(\frac{1}{J_K^0}\boldsymbol{P}_a, \nabla_{\mathbf{x}_0}\boldsymbol{\psi}_h\right)_{\mathcal{T}_h^{f,0}} = 0, \quad \forall \boldsymbol{\psi}_h \in \boldsymbol{S}_h^k \text{ with } \boldsymbol{\psi}_h|_{\partial\Omega_0^f} = 0, \tag{45b}$$

where J_K^0 is the Jacobian determinant for the initial configuration given in (6), and following [80], we use the logarithmic variation of the neo-Hookean material law

$$\boldsymbol{P}_a := \boldsymbol{F}_a(\lambda_a \ln J_a \boldsymbol{C}_a^{-1} + \mu_a(\mathbf{I} - \boldsymbol{C}_a^{-1}))$$

where $\boldsymbol{F}_a = \nabla_{\mathbf{x}_0}\boldsymbol{\phi}_h$, $J_a = \det(\boldsymbol{F}_a)$, $\boldsymbol{C}_a = \boldsymbol{F}_a^T\boldsymbol{F}_a$. We take the artificial Lamé parameters $\mu_a = 1$ and $\lambda_a = 1.5$ so that the Poisson ration $\nu_a = \frac{\lambda_a}{2(\lambda_a+\mu_a)} = 0.3$. After the discrete ALE maps $\boldsymbol{\phi}_h^n$ have been computed, the mesh velocity is obtained by the BDF[m] formula:

$$\boldsymbol{\omega}_h^{f,n} := \mathbb{D}_h^m \boldsymbol{\phi}_h^n \tag{46}$$

5. Numerical results

Our numerical simulations are performed using the open-source finite-element software NGSolve [78], `https://ngsolve.org/`.

5.1. Example 1: Convergence study for the ALE fluid solver. We first consider the incompressible Navier-Stokes equations (2) with $\rho^f = 1$ and $\boldsymbol{f}^f = 0$ (no source term) on a static 2D periodic domain $\Omega_t^f = [0, 2\pi] \times [0, 2\pi]$ with initial conditions

$$\boldsymbol{u}^f(x, y, 0) = (\cos(x)\sin(y), -\sin(x)\cos(y)), \quad p^f(x, y, 0) = -\frac{1}{4}(\cos(2x) + \cos(2y)).$$

The exact solution is given by the following Taylor-Green vortex solution:

$$\boldsymbol{u}^f(x, y, t) = (\cos(x)\sin(y)F(t), -\sin(x)\cos(y)F(t)),$$

$$p^f(x,y,t) = -\frac{1}{4}(\cos(2x)+\cos(2y))F(2t),$$

where $F(t) = \exp(-2\mu^f t)$. We take dynamic viscosity $\mu^f = 0.1$, and final time at $t = 1$.

In this example, we focus on verifying the accuracy of spatial approximation of the HDG scheme (19). In particular, we consider the scheme (19) with polynomial degree $k \in \{1,2,3,4\}$ combined with a high-order BDF$[k+2]$ time stepping. We consider both the static mesh case, and the moving mesh case with a prescribed ALE mapping

$$\boldsymbol{\phi}_t(x,y,t) = (x + 0.5\sin(x)\cos(y)\sin(\pi t), y - 0.5\cos(x)\sin(y)\sin(\pi t).$$

For the moving mesh case, the ALE map is interpolated using functions in $\boldsymbol{S}_h^k$, which is the space of continuous piecewise polynomials of degree k defined in (5).

We consider a sequence of structured triangular meshes obtained by splitting the square domain into $N \times N$ equal squares and then splitting each small square to two triangles by connecting its diagonal line with negative slope, where $N = 8 \times 2^l$ for $l \in \{0,1,2,3\}$. On each mesh with size N, the (uniform) time step size is taken to be $\Delta t = 1/N$ for $k = 1,2$, and $\Delta t = 1/2N$ for $k = 3,4$. We record the L^2-convergence rates of the strain rate tensor approximation $\boldsymbol{\epsilon}_h^f$, pressure approximation p_h^f, velocity approximation $\boldsymbol{u}_h^f$, divergence of the velocity approximation $\mathrm{div}(\boldsymbol{u}_h^f)$, and a postprocessed velocity approximation $\boldsymbol{u}_h^*$, which is (part of) the solution to the following local problem: find $(\boldsymbol{u}_h^*, \boldsymbol{\lambda}_h) \in [W_h^{k+1,f}]^d \times \Lambda_h$ such that

$$\begin{aligned}(\boldsymbol{D}_x(\boldsymbol{u}_h^*), \boldsymbol{D}_x(\boldsymbol{v}_h))_{\mathcal{T}_h^{f,t}} + (\boldsymbol{\lambda}_h, \boldsymbol{v}_h)_{\mathcal{T}_h^{f,t}} &= \left(\boldsymbol{\epsilon}_h^f, \boldsymbol{D}_x(\boldsymbol{v}_h)\right)_{\mathcal{T}_h^{f,t}}, \quad \forall \boldsymbol{v}_h \in [W_h^{k+1,f}]^d,\\ (\boldsymbol{u}_h^*, \boldsymbol{\mu}_h)_{\mathcal{T}_h^{f,t}} &= \left(\boldsymbol{u}_h^f, \boldsymbol{\mu}_h\right)_{\mathcal{T}_h^{f,t}}, \quad \forall \boldsymbol{v}_h \in \Lambda_h,\end{aligned}$$

where

$$\Lambda_h := \{\boldsymbol{\mu} \in [L^2(\mathcal{T}_h^f)]^d : \quad \boldsymbol{\mu}|_K \in RM(K), \forall K \in \mathcal{T}_h^f\},$$

with $RM(K) := [\mathcal{P}^0(K)]^d \oplus [\mathcal{P}^0(K)] \times \boldsymbol{x}$ being the space of rigid motions in element K. The above postprocessing can be found, e.g., in [44].

The history of convergence for the static mesh case is recorded in Table 3, and that for the moving mesh case is recorded in Table 4. From both tables, we observe optimal L^2-convergence rate of k in pressure p_h^f and $k+1$ in velocity $\boldsymbol{u}_h^f$, and machine zero in the L^2-norm of the divergence of velocity approximation for all polynomial degree k. The convergence rate for the strain rate tensor $\boldsymbol{\epsilon}_h^f$ is slightly less than $k+1$. Moreover, the error in the postprocessed velocity $\boldsymbol{u}_h^*$ is always smaller than that for $\boldsymbol{u}_h^f$, whose convergence rate is in between $k+1$ and $k+2$ for all cases, which is a superconvergence property. We remark that due to the use of symmetric tensor approximation $\boldsymbol{\epsilon}_h^f$ in the HDG formulation (19), the best theoretical result on the L^2-convergence rates for $\boldsymbol{\epsilon}_h^f$ and $\boldsymbol{u}_h^*$ one can prove is $k+1/2$ and $k+1$, respectively, see, e.g., [44] for a similar analysis for linear elasticity problems. It is clear that here the numerical results perform slightly better than the theory might predict.

To summarize, the scheme (19) is numerically observed to provide (1) optimal spatial convergence in the velocity and pressure approximations, (2) divergence-free velocity approximations, (3) nearly optimal spatial convergence in the strain rate tensor, and (4) superconvergence in the postprocessed velocity approximation.

TABLE 3. **Example 1:** History of convergence of the L^2-errors, static mesh case. Here e_ϵ, e_p, e_u, e_{u^*}, and e_{div}, respectively, represents the L^2-errors at final time $t = 1$ for the approximations $\boldsymbol{\epsilon}_h^f$, p_h^f, $\boldsymbol{u}_h^f$, $\boldsymbol{u}_h^*$, and $\text{div}(\boldsymbol{u}_h^f)$, respectively.

		e_ϵ		e_p		e_u		e_{u^*}		e_{div}
k	N	Error	Order	Error	Order	Error	Order	Error	Order	Error
1	8	4.057e-01	–	3.916e-01	–	2.461e-01	–	1.326e-01	–	3.232e-16
	16	1.309e-01	1.63	1.960e-01	1.00	6.278e-02	1.97	2.597e-02	2.35	3.372e-16
	32	3.740e-02	1.81	9.766e-02	1.01	1.551e-02	2.02	5.000e-03	2.38	3.378e-16
	64	1.001e-02	1.90	4.876e-02	1.00	3.848e-03	2.01	1.078e-03	2.21	3.463e-16
2	8	6.910e-02	–	7.318e-02	–	2.324e-02	–	9.966e-03	–	4.726e-16
	16	1.072e-02	2.69	1.863e-02	1.97	2.948e-03	2.98	7.962e-04	3.65	4.490e-16
	32	1.561e-03	2.78	4.680e-03	1.99	3.741e-04	2.98	6.681e-05	3.57	4.520e-16
	64	2.149e-04	2.86	1.171e-03	2.00	4.738e-05	2.98	6.440e-06	3.37	4.572e-16
3	8	7.608e-03	–	9.475e-03	–	1.962e-03	–	9.267e-04	–	5.891e-16
	16	6.284e-04	3.60	1.208e-03	2.97	1.236e-04	3.99	3.762e-05	4.62	5.735e-16
	32	4.595e-05	3.77	1.516e-04	2.99	7.855e-06	3.98	1.361e-06	4.79	5.683e-16
	64	3.151e-06	3.87	1.897e-05	3.00	4.994e-07	3.98	4.630e-08	4.88	5.816e-16
4	8	5.818e-04	–	9.373e-04	–	1.390e-04	–	5.710e-05	–	7.214e-16
	16	2.127e-05	4.77	5.893e-05	3.99	4.396e-06	4.98	1.046e-06	5.77	7.057e-16
	32	7.459e-07	4.83	3.698e-06	3.99	1.401e-07	4.97	1.781e-08	5.88	7.076e-16
	64	2.506e-08	4.90	2.314e-07	4.00	4.451e-09	4.98	2.997e-10	5.89	7.111e-16

TABLE 4. **Example 1:** History of convergence of the L^2-errors, moving mesh case. Here e_ϵ, e_p, e_u, e_{u^*}, and e_{div}, respectively, represent the L^2-errors at final time $t = 1$ for the approximations $\boldsymbol{\epsilon}_h^f$, p_h^f, $\boldsymbol{u}_h^f$, $\boldsymbol{u}_h^*$, and $\text{div}(\boldsymbol{u}_h^f)$, respectively.

		e_ϵ		e_p		e_u		e_{u^*}		e_{div}
k	N	Error	Order	Error	Order	Error	Order	Error	Order	Error
1	8	6.009e-01	–	4.035e-01	–	2.497e-01	–	1.637e-01	–	2.851e-16
	16	2.053e-01	1.55	1.977e-01	1.03	6.042e-02	2.05	2.833e-02	2.53	3.325e-16
	32	6.111e-02	1.75	9.786e-02	1.01	1.475e-02	2.03	4.707e-03	2.59	3.525e-16
	64	1.682e-02	1.86	4.878e-02	1.00	3.650e-03	2.01	8.720e-04	2.43	3.487e-16
2	8	9.904e-02	–	7.374e-02	–	2.584e-02	–	1.671e-02	–	4.582e-16
	16	1.532e-02	2.69	1.865e-02	1.98	3.028e-03	3.09	1.278e-03	3.71	4.723e-16
	32	2.335e-03	2.71	4.680e-03	1.99	3.720e-04	3.02	9.326e-05	3.78	4.469e-16
	64	3.356e-04	2.80	1.171e-03	2.00	4.677e-05	2.99	7.090e-06	3.72	4.525e-16
3	8	9.935e-03	–	9.510e-03	–	2.207e-03	–	1.419e-03	–	5.879e-16
	16	8.035e-04	3.63	1.208e-03	2.98	1.266e-04	4.12	5.449e-05	4.70	5.847e-16
	32	6.052e-05	3.73	1.516e-04	2.99	7.838e-06	4.01	1.996e-06	4.77	5.761e-16
	64	4.235e-06	3.84	1.897e-05	3.00	4.964e-07	3.98	6.873e-08	4.86	5.778e-16
4	8	8.600e-04	–	9.294e-04	–	1.850e-04	–	1.360e-04	–	7.345e-16
	16	2.984e-05	4.85	5.894e-05	3.98	4.667e-06	5.31	2.098e-06	6.02	7.033e-16
	32	1.087e-06	4.78	3.698e-06	3.99	1.411e-07	5.05	3.560e-08	5.88	7.108e-16
	64	3.774e-08	4.85	2.314e-07	4.00	4.434e-09	4.99	6.068e-10	5.87	7.064e-16

5.2. Example 2: Convergence study for the elastodynamics solver. We now numerically verify the spatial approximation errors of the TDNNS elastodynamics solver (25) and its non-conforming reduced version.

Here we consider both the Saint Venant-Kirchhoff model (21), and the linear elastodynamics model where $\frac{\partial \Psi}{\partial \boldsymbol{F}}$ in (21c) is replaced by the following linearization

$$\frac{\partial \Psi}{\partial \boldsymbol{F}} = \lambda^s \mathrm{tr}(\boldsymbol{e})\mathbf{I} + 2\mu^s \boldsymbol{e}, \quad \text{with } \boldsymbol{e} = \frac{1}{2}(\boldsymbol{F}^T + \boldsymbol{F} - \mathbf{I}). \tag{47}$$

Note that for the linear case, the tensor $\boldsymbol{P}$ is symmetric.

We consider a 2D periodic domain $\Omega^s = [0, 2\pi] \times [0, 2\pi]$ with material parameters $\rho^s = 1, \mu^s = 1, \lambda^s = 1$. We take source term $\boldsymbol{f}^s$ and initial data such that the manufactured exact solution for the displacement is

$$\boldsymbol{d}(x, y, t) = (\cos(x)\sin(y)\sin(t), -\sin(x)\cos(y)\sin(t)).$$

We take final time at $t = 0.2$.

We apply the TDNNS scheme (25) and the non-conforming reduced TDNNS scheme with approximation spaces (30) with polynomial degree $k \in \{1, 2, 3, 4\}$ combined with a high-order BDF$[k + 2]$ time stepping on a sequence of structured triangular meshes obtained by splitting the square domain into $N \times N$ equal squares and then splitting each small square to two triangles by connecting its diagonal line with negative slope, where $N = 8 \times 2^l$ for $l \in \{0, 1, 2, 3\}$. On each mesh with size N, the (uniform) time step size is taken to be $\Delta t = 0.2/N$ when the polynomial degree $k = 1$, $\Delta t = 0.1/N$ when $k = 2, 3$, and $\Delta t = 0.05/N$ when $k = 4$. The original TDNNS scheme has $2(k + 1)$ globally coupled DOFs per edge, while the non-conforming reduced TDNNS scheme has $k + \max(2, k)$ globally coupled DOFs per edge, which is computationally more efficient.

We record the history of convergence of errors in the L^2-norm at final time $t = 0.2$ for the variables $\boldsymbol{P}_{\mathrm{sym},h}, \boldsymbol{F}_{\mathrm{sym},h}$, $\boldsymbol{u}_h^s$, and $\boldsymbol{d}_h$. The results for the TDNNS scheme are presented in Table 5 for the linear case and in Table 7 for the nonlinear case, and those for the non-conforming reduced TDNNS scheme are presented in Table 6 for the linear case and in Table 8 for the nonlinear case.

Comparing the results in Table 5 and Table 6 for the linear model, we observe both methods provide the expected L^2-convergence rates of order k for the tensor variables $\boldsymbol{P}_{\mathrm{sym},h}$ and $\boldsymbol{F}_{\mathrm{sym},h}$, and of order $k + 1$ for the velocity and displacement variables $\boldsymbol{u}_h^s$ and $\boldsymbol{d}_h$. For a fixed polynomial degree k, the error magnitudes on the final mesh for both methods are also comparable to each other.

Comparing the results in Table 7 and Table 8 for the nonlinear model, we observe the convergence rates for the original TDNNS scheme is similar to the linear case, which are of order k for the tensor variables $\boldsymbol{P}_{\mathrm{sym},h}$ and $\boldsymbol{F}_{\mathrm{sym},h}$, and of order $k+1$ for the velocity and displacement variables $\boldsymbol{u}_h^s$ and $\boldsymbol{d}_h$. However, the convergence rates for the non-conforming reduced TDNNS scheme deteriorate slightly, noticeably on the velocity and displacement fields for $k \geq 2$. Comparing the error magnitudes on the final mesh for the two methods, we find that the errors for all the variables for the reduced scheme are roughly at most 3 times larger that those for the original TDNNS scheme. Hence the reduced scheme is still highly competitive for the nonlinear model due to its computational efficiency.

5.3. Example 3: Nonlinear elasticity with thin structures. Various benchmark tests for 3D large deformation nonlinear elastostatics problems have been performed in [62] for the nonlinear TDNNS scheme. Excellent results were obtained therein for problems involve thin structure or in the nearly incompressible regime using highly anisotropic elements.

Here we present the results of the TDNNS scheme for three shell problems from the benchmark examples in [84] to further highlight its excellent performance for

TABLE 5. **Example 2:** History of convergence of the L^2-errors for the linear elastodynamics case for the TDNNS scheme (25). Here e_P, e_F, e_u, and e_d, respectively, represents the L^2-errors at final time $t = 0.2$ for the approximations $\boldsymbol{P}_{\mathrm{sym},h}$, $\boldsymbol{F}_{\mathrm{sym},h}$, $\boldsymbol{u}_h^s$, and $\boldsymbol{d}_h$, respectively.

		e_P		e_F		e_u		e_d	
k	N	Error	Order	Error	Order	Error	Order	Error	Order
1	4	4.392e-01	–	1.908e-01	–	1.255e+00	–	2.552e-01	–
	8	3.101e-01	0.50	1.530e-01	0.32	3.351e-01	1.90	6.837e-02	1.90
	16	1.929e-01	0.68	9.640e-02	0.67	8.514e-02	1.98	1.722e-02	1.99
	32	1.063e-01	0.86	5.313e-02	0.86	2.188e-02	1.96	4.308e-03	2.00
2	4	1.916e-01	–	8.779e-02	–	2.149e-01	–	4.452e-02	–
	8	5.167e-02	1.89	2.504e-02	1.81	2.864e-02	2.91	5.844e-03	2.93
	16	1.339e-02	1.95	6.477e-03	1.95	3.664e-03	2.97	7.022e-04	3.06
	32	3.501e-03	1.94	1.696e-03	1.93	4.699e-04	2.96	8.733e-05	3.01
3	4	3.496e-02	–	1.566e-02	–	4.875e-02	–	1.005e-02	–
	8	5.719e-03	2.61	2.758e-03	2.51	3.085e-03	3.98	5.466e-04	4.20
	16	7.915e-04	2.85	3.826e-04	2.85	2.319e-04	3.73	3.377e-05	4.02
	32	1.067e-04	2.89	5.182e-05	2.88	1.094e-05	4.41	2.108e-06	4.00
4	4	9.318e-03	–	4.193e-03	–	5.062e-03	–	1.041e-03	–
	8	5.578e-04	4.06	2.676e-04	3.97	1.930e-04	4.71	3.356e-05	4.96
	16	3.488e-05	4.00	1.663e-05	4.01	7.647e-06	4.66	1.006e-06	5.06
	32	2.250e-06	3.95	1.076e-06	3.95	2.183e-07	5.13	3.140e-08	5.00

TABLE 6. **Example 2:** History of convergence of the L^2-errors for the linear elastodynamics case for the non-conforming reduced TDNNS scheme with approximation spaces (30). Here e_P, e_F, e_u, and e_d, respectively, represents the L^2-errors at final time $t = 0.2$ for the approximations $\boldsymbol{P}_{\mathrm{sym},h}$, $\boldsymbol{F}_{\mathrm{sym},h}$, $\boldsymbol{u}_h^s$, and $\boldsymbol{d}_h$, respectively.

		e_P		e_F		e_u		e_d	
k	N	Error	Order	Error	Order	Error	Order	Error	Order
1	4	4.543e-01	–	1.926e-01	–	1.028e+00	–	2.069e-01	–
	8	3.185e-01	0.51	1.302e-01	0.57	2.752e-01	1.90	5.355e-02	1.95
	16	2.461e-01	0.37	1.004e-01	0.38	1.024e-01	1.43	1.388e-02	1.95
	32	1.304e-01	0.92	5.327e-02	0.91	1.644e-02	2.64	3.435e-03	2.01
2	4	2.013e-01	–	9.130e-02	–	2.105e-01	–	4.261e-02	–
	8	6.138e-02	1.71	2.789e-02	1.71	3.239e-02	2.70	5.657e-03	2.91
	16	2.044e-02	1.59	8.370e-03	1.74	5.521e-03	2.55	7.886e-04	2.84
	32	4.393e-03	2.22	1.798e-03	2.22	4.658e-04	3.57	9.636e-05	3.03
3	4	3.790e-02	–	1.680e-02	–	5.176e-02	–	1.006e-02	–
	8	7.165e-03	2.40	3.308e-03	2.34	3.309e-03	3.97	5.683e-04	4.15
	16	8.457e-04	3.08	3.879e-04	3.09	2.216e-04	3.90	3.481e-05	4.03
	32	1.023e-04	3.05	4.692e-05	3.05	1.166e-05	4.25	2.176e-06	4.00
4	4	9.860e-03	–	4.444e-03	–	5.217e-03	–	1.053e-03	–
	8	6.153e-04	4.00	2.871e-04	3.95	1.985e-04	4.72	3.439e-05	4.94
	16	3.661e-05	4.07	1.690e-05	4.09	7.454e-06	4.73	1.015e-06	5.08
	32	2.290e-06	4.00	1.062e-06	3.99	2.308e-07	5.01	3.122e-08	5.02

TABLE 7. **Example 2:** History of convergence of the L^2-errors for the nonlinear elastodynamics case for the TDNNS scheme (25). Here e_P, e_F, e_u, and e_d, respectively, represents the L^2-errors at final time $t = 0.2$ for the approximations $\boldsymbol{P}_{\mathrm{sym},h}$, $\boldsymbol{F}_{\mathrm{sym},h}$, $\boldsymbol{u}_h^s$, and $\boldsymbol{d}_h$, respectively.

		e_P		e_F		e_u		e_d	
k	N	Error	Order	Error	Order	Error	Order	Error	Order
1	4	5.053e-01	–	1.919e-01	–	1.254e+00	–	2.552e-01	–
	8	3.267e-01	0.63	1.548e-01	0.31	3.350e-01	1.90	6.835e-02	1.90
	16	1.985e-01	0.72	9.714e-02	0.67	8.516e-02	1.98	1.722e-02	1.99
	32	1.088e-01	0.87	5.343e-02	0.86	2.184e-02	1.96	4.306e-03	2.00
2	4	2.051e-01	–	8.828e-02	–	2.151e-01	–	4.451e-02	–
	8	5.568e-02	1.88	2.544e-02	1.80	2.901e-02	2.89	5.848e-03	2.93
	16	1.412e-02	1.98	6.582e-03	1.95	3.687e-03	2.98	7.038e-04	3.05
	32	3.666e-03	1.95	1.720e-03	1.94	4.753e-04	2.96	8.769e-05	3.00
3	4	4.921e-02	–	1.691e-02	–	4.928e-02	–	1.005e-02	–
	8	6.263e-03	2.97	2.840e-03	2.57	3.117e-03	3.98	5.472e-04	4.20
	16	8.220e-04	2.93	3.885e-04	2.87	2.333e-04	3.74	3.388e-05	4.01
	32	1.091e-04	2.91	5.228e-05	2.89	1.122e-05	4.38	2.109e-06	4.01
4	4	9.704e-03	–	4.291e-03	–	5.087e-03	–	1.043e-03	–
	8	6.628e-04	3.87	2.863e-04	3.91	2.053e-04	4.63	3.381e-05	4.95
	16	3.771e-05	4.14	1.725e-05	4.05	7.919e-06	4.70	1.020e-06	5.05
	32	2.361e-06	4.00	1.100e-06	3.97	2.267e-07	5.13	3.175e-08	5.01

TABLE 8. **Example 2:** History of convergence of the L^2-errors for the nonlinear elastodynamics case for the non-conforming reduced TDNNS scheme with approximation spaces (30). Here e_P, e_F, e_u, and e_d, respectively, represents the L^2-errors at final time $t = 0.2$ for the approximations $\boldsymbol{P}_{\mathrm{sym},h}$, $\boldsymbol{F}_{\mathrm{sym},h}$, $\boldsymbol{u}_h^s$, and $\boldsymbol{d}_h$, respectively.

		e_P		e_F		e_u		e_d	
k	N	Error	Order	Error	Order	Error	Order	Error	Order
1	4	5.087e-01	–	1.940e-01	–	1.029e+00	–	2.069e-01	–
	8	3.333e-01	0.61	1.315e-01	0.56	2.760e-01	1.90	5.356e-02	1.95
	16	2.514e-01	0.41	1.008e-01	0.38	1.033e-01	1.42	1.391e-02	1.94
	32	1.322e-01	0.93	5.375e-02	0.91	1.748e-02	2.56	3.475e-03	2.00
2	4	2.380e-01	–	9.954e-02	–	2.106e-01	–	4.259e-02	–
	8	7.291e-02	1.71	3.006e-02	1.73	3.312e-02	2.67	5.656e-03	2.91
	16	2.327e-02	1.65	9.008e-03	1.74	6.159e-03	2.43	8.023e-04	2.82
	32	5.374e-03	2.11	2.067e-03	2.12	1.415e-03	2.12	1.218e-04	2.72
3	4	5.716e-02	–	1.894e-02	–	5.206e-02	–	1.006e-02	–
	8	1.056e-02	2.44	4.173e-03	2.18	4.106e-03	3.66	5.812e-04	4.11
	16	1.408e-03	2.91	5.582e-04	2.90	4.081e-04	3.33	4.036e-05	3.85
	32	1.900e-04	2.89	7.640e-05	2.87	2.930e-05	3.80	3.170e-06	3.67
4	4	2.214e-02	–	8.465e-03	–	7.799e-03	–	1.095e-03	–
	8	1.472e-03	3.91	5.710e-04	3.89	4.163e-04	4.23	4.063e-05	4.75
	16	1.101e-04	3.74	4.361e-05	3.71	2.521e-05	4.05	2.008e-06	4.34
	32	7.558e-06	3.87	3.010e-06	3.86	7.436e-07	5.08	8.200e-08	4.61

thin structures. The shell problems are discretized using the 3D TDNNS scheme (25) with a reduced stress space $\boldsymbol{\Sigma}_h^{k,\mathrm{red}}$ and normal displacement space $\widetilde{\boldsymbol{V}}_h^{\max(1,k-1),s}$ on hexahedral meshes with only one element in the thickness direction. We take polynomials of degree $k = 2$ in the numerical simulations. The globally coupled DOFs consists of 3 tangential displacement DOFs per edge, 12 tangential displacement DOFs per face, and 4 normal displacement DOFs per face. The overall computational cost is comparable to a conforming Galerkin method with polynomials of degree 3 on the same mesh.

Example 3.1: Slit annular plate subjected to lifting line force. The problem consider a slit annular plate domain with inner radius $R_i = 6$, outer radius $R_o = 10$, and thickness $t = 0.03$ that is clamped at one end of the slit and subjected to a lifting force P at the other end; see left of Figure 1 for the domain under maximum deformation. The lifting force with a maximum magnitude $P_{\max} = 0.8$ is applied as traction along vertical direction over the slit boundary. The material parameters are $E = 21 \times 10^6$ and $\nu = 0$. A load incrementation algorithm with uniform 40 load steps is used to solve the nonlinear problem. The vertical deflections at two end points of the slit are shown in Figure 1 for the TDNNS scheme on two meshes, a coarse mesh with 2×10 hexahedral elements and a fine mesh with 3×15 hexahedral elements, along with reference data from [84] which use the S4R shell elements on a quadrilateral mesh with 10×80 elements. The computed results on both meshes are in excellent agreements with the reference data.

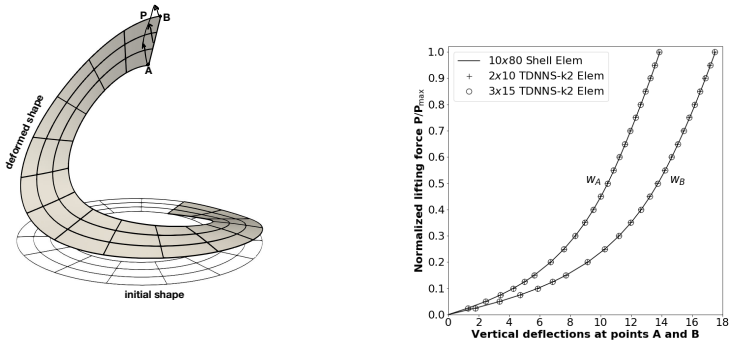

FIGURE 1. **Example 3.1:** Left: The slit plate domain under maximum deformation computed using the reduced TDNNS scheme with $k = 2$ on a 15×3 hexahedral mesh. Right: Vertical deflections w_A and w_B at tips of the slit, A (interior slip tip) and B (exterior slip tip). Reference solution computed with a 10×80 S4R shell elements is also displayed.

5.3.1. Example 3.2: Hemispherical shell subjected to alternating radial forces. The hemispherical shell problem was considered in [84] among others. The domain is a hemispherical shell with an 18° circular cutout at its pole. The material properties considered are $E = 6.825 \times 10^7$, $\nu = 0.3$. The radius of the hemisphere is $R = 10$ and its thickness is $t = 0.04$. The shell is subjected to four alternating radial point forces, whose magnitude are $P_{\max} = 400$ each. Owing to symmetry, one-quarter of the problem is used in the simulation and symmetry boundary conditions are applied on the artificial boundaries; see left of Figure 2. Here the pulling

point force on point A is implemented as a surface traction force concentrated on the exterior bottom left corner quadrilateral surface element, and the pushing point force on point B is implemented as a surface traction force concentrated on the interior bottom right corner quadrilateral surface element. The deformed geometry under maximum load is shown in the middle of Figure 2, and the radial displacements at points A and B are shown in the right of Figure 2 for the reduced TDNNS scheme with $k = 2$ on a coarse mesh with 8×8 hexahedral elements and a fine mesh with 16×16 hexahedral elements, along with reference data from [84] which use the S4R shell elements on a quadrilateral mesh with 16×16 elements. The computed results on both meshes are in good agreements with the reference data. We note that there is a slightly underestimation of the displacement at point B for the results on the coarse 8×8 mesh, which might due to the boundary condition treatment using surface integrals for the point load.

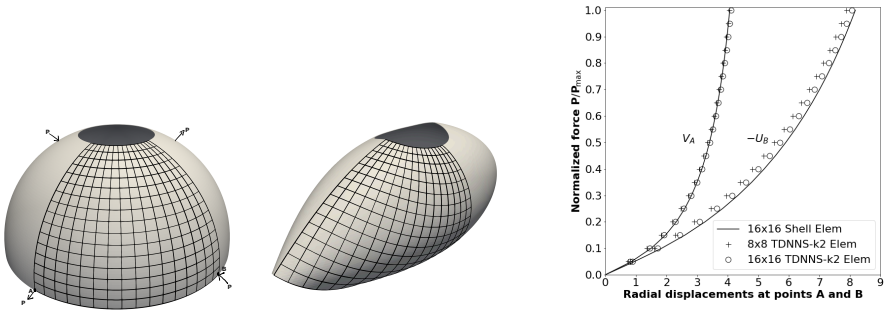

FIGURE 2. **Example 3.2:** Left: The initial hemispherical shell geometry. The one-quarter computational domain is discretized with a 16×16 hexahedral mesh. Middle: The deformed geometry under maximum load $P = P_{\max}$ computed using the reduced TDNNS scheme with $k = 2$ on the 16×16 mesh. Right: Radial displacements at points A and B. Reference solution computed with a 16×16 S4R shell elements is also displayed.

5.3.2. Example 3.3: Pullout of an open-ended cylindrical shell. In our last shell example, we consider an open-ended cylinder being pulled by a pair of symmetric radial forces P whose maximum magnitude are $P_{\max} = 40,000$. The cylinder is of radius $R = 4.953$, length $L = 10.35$, and thickness $t = 0.094$. The material properties considered are $E = 10.5 \times 10^6, \nu = 0.3125$. Owing to symmetries, one-eighth of the problem is used in the simulation and symmetry boundaries are imposed on the artificial boundaries; see left of Figure 3 for the cylinder geometry and a typical structured mesh for one-eighth of the domain. Here, similar to Example 3.2, the pulling force at point A is implemented as a surface traction force concentrated on the exterior top right corner quadrilateral surface element. The deformed geometry under maximum load is shown in the middle of Figure 3, and radial displacements at points A, B, and C are shown in the right of Figure 3 for the reduced TDNNS scheme with $k = 2$ on a coarse mesh with 8×12 hexahedral elements and a fine mesh with 12×18 hexahedral elements, along with reference data from [84] which use the S4R shell elements on a quadrilateral mesh with 24×36

elements. The computed results on both meshes are in good agreements with the reference data.

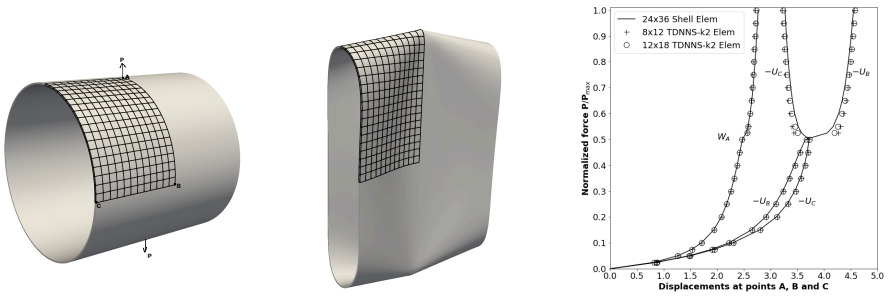

FIGURE 3. **Example 3.3:** Left: The initial cylindrical shell geometry. The one-eighth computational domain is discretized with a 12×18 hexahedral mesh. Middle: The deformed geometry under maximum load $P = P_{\max}$ computed using the reduced TDNNS scheme with $k = 2$ on the 12×18 mesh. Right: Radial displacements at points A, B and C. Reference solution computed with a 24×36 S4R shell elements is also displayed.

5.4. Example 4: Convergence study for the FSI solver. We now numerically verify the approximation errors of the FSI solvers (39). Here we consider a linear FSI model where the nonlinear convection is ignored in the fluid and linear elastodynamics is used in the structure. We consider a 2D fluid domain $\Omega^f = [0, 2\pi] \times [0, 1.5\pi]$ with material parameters $\rho^f = 1, \mu^f = 0.1$, and a structure domain $\Omega^s = [0, 2\pi] \times [1.5\pi, 2\pi]$ with material parameters $\rho^s = 1, \mu^s = 1, \lambda^s = 1$. The interface is located at the horizontal line $y = 1.5\pi$. Periodic boundary conditions are applied in the x-direction, and Dirichlet boundary conditions are applied in the y-direction. We take source terms $\boldsymbol{f}^f$, $\boldsymbol{f}^s$ and initial data such that the manufactured exact solutions are

$$\begin{aligned} \boldsymbol{d}(x, y, t) &= (\cos(x)\sin(y)\sin(t), -\sin(x)\cos(y)\sin(t)), \\ \boldsymbol{u}^f(x, y, t) = \boldsymbol{u}^s(x, y, t) &= (\cos(x)\sin(y)\cos(t), -\sin(x)\cos(y)\cos(t)), \\ p^f(x, y, t) &= \sin(x)\sin(y)\sin(t), \end{aligned}$$

where a source term is also added in (33b) on the interface to account for stress imbalance. We take final time at $t = 0.5$.

We apply the algorithms ALG-M, ALG-SP, and ALG-P using polynomial degree $k \in \{1, 2, 3, 4\}$ along with BDF$[k + 1]$ time stepping on a sequence of structured $2 \times N \times N$ triangular meshes, with $N = 8 \times 2^l$ for $l \in \{0, 1, 2, 3\}$. We take time step size to be $\Delta t = c/N$ with $c > 0$ chosen properly for different algorithms and polynomial degrees for stability considerations.

For polynomial degree $k = 1$ and BDF[2] time stepping, it was observed that taking $\alpha \in [2, 20]$ leads to a stable partitioned algorithm ALG-P for long time simulations under the time step restriction $\Delta t \leq 0.2/N$. In Table 9, we record the history of convergence of L^2-errors at final time $t = 0.5$ for the variables $\boldsymbol{\epsilon}_h^f$, p_h^f, $\boldsymbol{u}_h^f$, $\boldsymbol{P}_{\mathrm{sym},h}$, $\boldsymbol{u}_h^s$, and $\boldsymbol{d}_h$ for the three algorithms with $k = 1$ and $\alpha = 10$,

where the stopping tolerance (42) for ALG-SP is taken to be $\eta = 10^{-4}$. We take $\Delta t = 1/N$ for the three algorithms and also take $\Delta t = 0.2/N$ for ALG-P. We note that, for $\Delta t = 1/N$, both ALG-M and ALG-SP algorithms lead to stable long time simulations, while the ALG-P algorithm leads to instability around time $t = 2.5$. Such instability was not observed yet at $t = 0.5$ where the errors are recorded. From Table 9, we observe optimal second-order (space-time) convergence for the variables $\boldsymbol{\epsilon}_h^f$, $\boldsymbol{u}_h^{f/s}$, and $\boldsymbol{d}_h$, optimal first-order convergence in the pressure approximation p_h^f, and sub-optimal first-order convergence in the structure stress $\boldsymbol{P}_{\mathrm{sym},h}$. The average number of sub-iterations for ALG-SP decreases from 9.3 on the coarsest mesh with $N = 8$ to 1.9 on the finest mesh with $N = 64$, which is expected as the time step size is smaller on the finer mesh where the extrapolated data are more accurate. Moreover, the error magnitudes are similar for ALG-M and ALG-SP with $\Delta t = 1/N$, and for ALG-P with $\Delta t = 0.2/N$. The errors for ALG-P with $\Delta t = 1/N$ are found to be slightly larger than the other methods, which eventually lead to instability as the simulation continues.

TABLE 9. **Example 4:** History of convergence of the L^2-errors at time $t = 0.5$ for ALG-M, ALG-IP2, and ALG-P. Polynomial degree $k = 1$, BDF[2] time stepping. Here e_ϵ, e_p, e_u^f, e_P, e_u^s, and e_d respectively, represents the L^2-errors for the approximations $\boldsymbol{\epsilon}_h^f$, p_h^f, $\boldsymbol{u}_h^f$, $\boldsymbol{P}_{h,\mathrm{sym}}$, $\boldsymbol{u}_h^s$, and $\boldsymbol{d}_h$, respectively.

	e_ϵ		e_p		e_u^f		e_P		e_u^s		e_d	
N	Error	Order	Error	Order	Error	Order	Error	Order	Error	Order	Error	Order
	ALG-M. $k=1, m=2$, $\alpha=10$, $\Delta t = 1/N$.											
8	2.665e-01	–	3.375e-01	–	1.987e-01	–	4.369e-01	–	1.178e-01	–	6.315e-02	–
16	8.178e-02	1.70	1.704e-01	0.99	5.111e-02	1.96	2.468e-01	0.82	2.941e-02	2.00	1.545e-02	2.03
32	2.267e-02	1.85	8.534e-02	1.00	1.292e-02	1.98	1.314e-01	0.91	7.570e-03	1.96	3.805e-03	2.02
64	5.965e-03	1.93	4.268e-02	1.00	3.245e-03	1.99	6.770e-02	0.96	1.924e-03	1.98	9.448e-04	2.01
	ALG-SP with $\eta = 10^{-4}$. $k=1, m=2$, $\alpha=10$, $\Delta t = 1/N$. Avg. # iter.: 9.3 for $N = 8$, 6.6 for $N = 16$, 5.0 for $N = 32$, and 1.9 for $N = 64$.											
8	2.665e-01	–	3.375e-01	–	1.987e-01	–	4.369e-01	–	1.178e-01	–	6.315e-02	–
16	8.179e-02	1.70	1.704e-01	0.99	5.112e-02	1.96	2.468e-01	0.82	2.939e-02	2.00	1.544e-02	2.03
32	2.267e-02	1.85	8.534e-02	1.00	1.292e-02	1.98	1.314e-01	0.91	7.566e-03	1.96	3.804e-03	2.02
64	6.370e-03	1.83	4.268e-02	1.00	3.299e-03	1.97	6.770e-02	0.96	1.903e-03	1.99	9.344e-04	2.03
	ALG-P. $k=1, m=2$, $\alpha=10$, $\Delta t = 1/N$.											
8	3.406e-01	–	3.371e-01	–	1.980e-01	–	4.486e-01	–	1.183e-01	–	6.158e-02	–
16	1.239e-01	1.46	1.704e-01	0.98	5.492e-02	1.85	2.486e-01	0.85	3.326e-02	1.83	1.520e-02	2.02
32	2.905e-02	2.09	8.533e-02	1.00	1.400e-02	1.97	1.318e-01	0.92	9.100e-03	1.87	3.815e-03	1.99
64	7.395e-03	1.97	4.268e-02	1.00	3.498e-03	2.00	6.776e-02	0.96	2.231e-03	2.03	9.569e-04	2.00
	ALG-P. $k=1, m=2$, $\alpha=10$, $\Delta t = 0.2/N$.											
8	2.764e-01	–	3.372e-01	–	2.018e-01	–	5.282e-01	–	1.267e-01	–	5.949e-02	–
16	8.273e-02	1.74	1.706e-01	0.98	5.122e-02	1.98	2.701e-01	0.97	3.026e-02	2.07	1.470e-02	2.02
32	2.267e-02	1.87	8.536e-02	1.00	1.294e-02	1.98	1.374e-01	0.98	7.793e-03	1.96	3.672e-03	2.00
64	6.001e-03	1.92	4.268e-02	1.00	3.252e-03	1.99	6.921e-02	0.99	1.944e-03	2.00	9.189e-04	2.00

For polynomial degree $k = 2$, it was observed that taking $\alpha \in [10, 40]$ leads to a stable partitioned algorithm ALG-P for long time simulations under the time step restriction $\Delta t \leq 0.1/N$. For this case, the monolithic scheme ALG-M is also found to be conditionally stable under the time step restriction $\Delta t \leq 0.1/N$. In Table 10, we record the history of convergence of L^2-errors at final time $t = 0.5$ for the three algorithms with $k = 2$, $\alpha = 20$, and $\Delta t = 0.1/N$, where the stopping tolerance (42) for ALG-SP is taken to be $\eta = 10^{-4}$. From Table 10, we observe optimal third-order (space-time) convergence for the variables $\boldsymbol{u}_h^{f/s}$, and $\boldsymbol{d}_h$, optimal second-order convergence in the pressure approximation p_h^f, sub-optimal 2.74th order of convergence in the fluid strain rate tensor $\boldsymbol{\epsilon}_h^f$ and sub-optimal second-order

convergence in the structure stress $\boldsymbol{P}_{\mathrm{sym},h}$. Moreover, the error magnitudes for the three methods are almost indistinguishable. It is interesting to observe that with stopping tolerance $\eta = 10^{-4}$, the average number of sub-iterations for ALG-SP is 0.0 on the two finer meshes with $N = 32$ and $N = 64$, which indicates that the ALG-P solution is accurate enough for this tolerance.

TABLE 10. **Example 4:** History of convergence of the L^2-errors at time $t = 0.5$ for ALG-M, ALG-IP2, and ALG-P. Polynomial degree $k = 2$, BDF[3] time stepping.

	e_ϵ		e_p		e_u^f		e_P		e_u^s		e_d	
N	Error	Order	Error	Order	Error	Order	Error	Order	Error	Order	Error	Order
	ALG-M. $k = 2, m = 3$, $\alpha = 20$, $\Delta t = 0.1/N$.											
8	4.989e-02	–	5.095e-02	–	2.124e-02	–	7.096e-02	–	1.343e-02	–	6.775e-03	–
16	7.355e-03	2.76	1.292e-02	1.98	2.722e-03	2.96	1.769e-02	2.00	1.617e-03	3.05	8.436e-04	3.01
32	1.098e-03	2.74	3.242e-03	1.99	3.458e-04	2.98	4.422e-03	2.00	1.952e-04	3.05	1.059e-04	2.99
64	1.640e-04	2.74	8.113e-04	2.00	4.364e-05	2.99	1.108e-03	2.00	2.549e-05	2.94	1.318e-05	3.01
	ALG-SP with $\eta = 10^{-4}$. $k = 2, m = 3$, $\alpha = 20$, $\Delta t = 0.1/N$. Avg. # iter.: 1.3 for $N = 8$, 0.2 for $N = 16$, 0.0 for $N = 32$, and 0.0 for $N = 64$.											
8	4.985e-02	–	5.095e-02	–	2.124e-02	–	7.096e-02	–	1.343e-02	–	6.775e-03	–
16	7.346e-03	2.76	1.292e-02	1.98	2.722e-03	2.96	1.769e-02	2.00	1.617e-03	3.05	8.436e-04	3.01
32	1.098e-03	2.74	3.242e-03	1.99	3.458e-04	2.98	4.422e-03	2.00	1.952e-04	3.05	1.059e-04	2.99
64	1.641e-04	2.74	8.113e-04	2.00	4.364e-05	2.99	1.108e-03	2.00	2.549e-05	2.94	1.318e-05	3.01
	ALG-P. $k = 2, m = 3$, $\alpha = 20$, $\Delta t = 0.1/N$.											
8	4.978e-02	–	5.095e-02	–	2.124e-02	–	7.096e-02	–	1.342e-02	–	6.775e-03	–
16	7.346e-03	2.76	1.292e-02	1.98	2.722e-03	2.96	1.769e-02	2.00	1.617e-03	3.05	8.436e-04	3.01
32	1.098e-03	2.74	3.242e-03	1.99	3.458e-04	2.98	4.422e-03	2.00	1.952e-04	3.05	1.059e-04	2.99
64	1.641e-04	2.74	8.113e-04	2.00	4.364e-05	2.99	1.108e-03	2.00	2.549e-05	2.94	1.318e-05	3.01

For polynomial degree $k = 3$, it was observed that a stable partitioned algorithm ALG-P for long time simulations can only be obtained under a very restrictive time step restriction $\Delta t \leq 0.004/N$. The monolithic scheme ALG-M was, however, observed to be conditionally stable under the much milder time step restriction $\Delta t \leq 0.075/N$. In Table 11, we record the history of convergence of L^2-errors at final time $t = 0.5$ for the algorithms ALG-M, ALG-SP with $\eta = 10^{-4}$, and ALG-SP with $\eta = 10^{-7}$, using $k = 3$, $\alpha = 40$, and time step size $\Delta t = 0.075/N$. The algorithm ALG-P immediately leads to solution blow-ups with these choices of parameters, hence the associated results are not recorded. From Table 11, we observe that the schemes ALG-M and ALG-SP with $\eta = 10^{-7}$ produce very similar results both in terms of orders of convergence and error magnitudes, with optimal forth-order (space-time) convergence for the variables $\boldsymbol{u}_h^{f/s}$ and $\boldsymbol{d}_h$, optimal third-order convergence in the pressure approximation p_h^f, sub-optimal 3.7th order of convergence in the fluid strain rate tensor $\boldsymbol{\epsilon}_h^f$ and sub-optimal third-order convergence in the structure stress $\boldsymbol{P}_{\mathrm{sym},h}$. The convergence results for ALG-SP with $\eta = 10^{-4}$ are similar to the other two methods on the first two set of meshes, but that on the finer meshes with $N = 32$ and $N = 64$ are significantly less accurate due to the use of a larger stopping tolerance. It is also interesting to observe that, similar to the $k = 3$ case, the number of sub-iterations for ALG-SP with $\eta = 10^{-7}$ (from 5.7 on the coarsest mesh to 1.4 on the finest mesh) is only slightly larger than that for $\eta = 10^{-4}$ (from 2.2 on the coarsest mesh to 1.2 on the finest mesh).

For polynomial degree $k = 4$, we couldn't find a combination parameter α that would lead to a stable partitioned algorithm ALG-P for long time simulations. For this reason, we again only perform convergence studies for the monolithic scheme ALG-M and the strongly coupled partitioned scheme ALG-SP. In Table 12, we record the history of convergence of L^2-errors at final time $t = 0.5$ for the three algorithms

TABLE 11. **Example 4:** History of convergence of the L^2-errors at time $t = 0.5$ for ALG-M, ALG-IP3, and ALG-IP2. Polynomial degree $k = 3$, BDF[4] time stepping.

	e_ϵ		e_p		e_u^f		e_P		e_u^s		e_d	
N	Error	Order	Error	Order	Error	Order	Error	Order	Error	Order	Error	Order
	ALG-M. $k = 3, m = 4$, $\alpha = 40$, $\Delta t = 0.075/N$.											
8	5.094e-03	–	5.653e-03	–	1.804e-03	–	7.852e-03	–	1.077e-03	–	5.598e-04	–
16	4.039e-04	3.66	7.170e-04	2.98	1.161e-04	3.96	1.047e-03	2.91	7.681e-05	3.81	3.510e-05	4.00
32	3.041e-05	3.73	8.994e-05	2.99	7.413e-06	3.97	1.350e-04	2.96	4.485e-06	4.10	2.256e-06	3.96
64	2.370e-06	3.68	1.125e-05	3.00	4.692e-07	3.98	1.709e-05	2.98	2.953e-07	3.92	1.409e-07	4.00
	ALG-SP with $\eta = 10^{-4}$. $k = 3, m = 4$, $\alpha = 40$, $\Delta t = 0.075/N$. Avg. # iter.: 2.2 for $N = 8$, 1.5 for $N = 16$, 1.3 for $N = 32$, and 1.2 for $N = 64$.											
8	5.140e-03	–	5.653e-03	–	1.804e-03	–	7.853e-03	–	1.087e-03	–	5.596e-04	–
16	4.181e-04	3.62	7.175e-04	2.98	1.160e-04	3.96	1.048e-03	2.91	8.134e-05	3.74	3.514e-05	3.99
32	1.885e-04	1.15	9.245e-05	2.96	7.809e-06	3.89	1.360e-04	2.95	1.120e-05	2.86	2.361e-06	3.90
64	8.099e-05	1.22	1.470e-05	2.65	9.942e-07	2.97	1.772e-05	2.94	1.883e-06	2.57	1.797e-07	3.72
	ALG-SP with $\eta = 10^{-7}$. $k = 3, m = 4$, $\alpha = 40$, $\Delta t = 0.075/N$. Avg. # iter.: 5.7 for $N = 8$, 2.2 for $N = 16$, 1.6 for $N = 32$, and 1.4 for $N = 64$.											
8	5.094e-03	–	5.653e-03	–	1.804e-03	–	7.852e-03	–	1.077e-03	–	5.598e-04	–
16	4.038e-04	3.66	7.170e-04	2.98	1.161e-04	3.96	1.047e-03	2.91	7.681e-05	3.81	3.510e-05	4.00
32	3.041e-05	3.73	8.994e-05	2.99	7.413e-06	3.97	1.350e-04	2.96	4.485e-06	4.10	2.256e-06	3.96
64	2.364e-06	3.69	1.125e-05	3.00	4.692e-07	3.98	1.709e-05	2.98	2.954e-07	3.92	1.409e-07	4.00

ALG-M, ALG-SP with $\eta = 10^{-6}$, and ALG-SP with $\eta = 10^{-8}$, using $k = 4$, $\alpha = 40$, and time step size $\Delta t = 0.075/N$. From Table 12, we observe that ALG-M and ALG-SP with $\eta = 10^{-8}$ produce very similar results both in terms of order of convergence and error magnitudes, with optimal fifth-order (space-time) convergence for the variables $\boldsymbol{u}_h^{f/s}$, and $\boldsymbol{d}_h$, optimal fourth-order convergence in the pressure approximation p_h^f, sub-optimal 4.7th order of convergence in the fluid strain rate tensor $\boldsymbol{\epsilon}_h^f$ and sub-optimal third-order convergence in the structure stress $\boldsymbol{P}_{\text{sym},h}$. The convergence results for ALG-SP with $\eta = 10^{-6}$ are similar to the other two methods on the first two set of meshes, but that on the finer meshes with $N = 32$ and $N = 64$ are less accurate due to the use of a larger stopping tolerance. It is also interesting to observe that the number of sub-iterations for ALG-SP with $\eta = 10^{-8}$ (from 7.6 on the coarsest mesh to 2.8 on the finest mesh) is slightly larger than that for $\eta = 10^{-6}$ (from 4.3 on the coarsest mesh to 2.7 on the finest mesh).

5.5. Example 5: Propagation of a pressure pulse. We consider the following classical benchmark problem that describes the propagation of a pressure pulse in a two-dimensional channel fluid flow interacting with a deformable wall. We follow the setup in [9, Example 2]. The reference domain is $\Omega_0^f = (0, 6) \times (0, 0.5)$ and $\Omega^s = (0, 6) \times (0.5, 0.6)$, with $\Gamma_0 = (0, 6) \times \{y = 0.5\}$ being the interface. The fluid flow is governed by the Navier-Stokes equations (2) with $\rho^f = 1$, $\mu^f = 0.035$, and $\boldsymbol{f}^f = 0$. The elastic wall is governed by a linear elastodynamics model (21) where the stress $\frac{\partial \Psi}{\partial \boldsymbol{F}}$ in (21c) is given by the linear relationship in (47), and an additional damping term $\beta \boldsymbol{d}$ is added to the left hand side of (21b) to act as a spring. The parameters for the structure are $\rho^s = 1.1$, $\mu^s = 5.75 \times 10^5$, $\lambda^s = 1.7 \times 10^6$, $\beta = 4 \times 10^6$, and $\boldsymbol{f}^s = 0$. The following set of boundary conditions are used:

$$
\begin{aligned}
(\boldsymbol{\sigma}^f \boldsymbol{n}) \cdot \boldsymbol{n} &= -p_{in}(t), \quad \mathsf{tng}(\boldsymbol{u}^f) = 0, && \text{on } \Gamma_{in}^f := \{x = 0\} \times (0, 0.5),\\
\boldsymbol{\sigma}^f \boldsymbol{n} &= 0, && \text{on } \Gamma_{out}^f := \{x = 6\} \times (0, 0.5),\\
\mathsf{tng}(\boldsymbol{\sigma}^f \boldsymbol{n}) &= 0, \quad \boldsymbol{u}^f \cdot \boldsymbol{n} = 0, && \text{on } \Gamma_{bot}^f := (0, 6) \times \{y = 0\},\\
\boldsymbol{d} &= 0, && \text{on } \Gamma_{dir}^s := \{x = 0\} \times (0, 0.5) \cup \{x = 6\} \times (0, 0.5),\\
(\boldsymbol{P}\boldsymbol{n}) \cdot \boldsymbol{n} &= 0, \quad \mathsf{tng}(\boldsymbol{d}) = 0, && \text{on } \Gamma_{top}^s := (0, 6) \times \{y = 0.6\},
\end{aligned}
$$

TABLE 12. **Example 4:** History of convergence of the L^2-errors at time $t = 0.5$ for ALG-M, ALG-IP8, and ALG-IP2. Polynomial degree $k = 4$, BDF[5] time stepping.

	e_ϵ		e_p		e_u^f		e_P		e_u^s		e_d	
N	Error	Order	Error	Order	Error	Order	Error	Order	Error	Order	Error	Order
	ALG-M. $k = 4, m = 5$, $\alpha = 40$, $\Delta t = 0.075/N$.											
8	3.703e-04	–	4.944e-04	–	1.283e-04	–	6.784e-04	–	8.026e-05	–	3.923e-05	–
16	1.411e-05	4.71	3.131e-05	3.98	4.132e-06	4.96	4.392e-05	3.95	2.259e-06	5.15	1.215e-06	5.01
32	5.152e-07	4.78	1.964e-06	4.00	1.317e-07	4.97	2.786e-06	3.98	7.680e-08	4.88	3.812e-08	4.99
64	2.017e-08	4.67	1.228e-07	4.00	4.167e-09	4.98	1.755e-07	3.99	2.350e-09	5.03	1.191e-09	5.00
	ALG-SP with $\eta = 10^{-6}$. $k = 4, m = 5$, $\alpha = 40$, $\Delta t = 0.075/N$. Avg. # iter.: 4.3 for $N = 8$, 3.3 for $N = 16$, 3.0 for $N = 32$, and 2.7 for $N = 64$.											
8	3.703e-04	–	4.944e-04	–	1.283e-04	–	6.784e-04	–	8.025e-05	–	3.923e-05	–
16	1.476e-05	4.65	3.131e-05	3.98	4.133e-06	4.96	4.392e-05	3.95	2.266e-06	5.15	1.215e-06	5.01
32	1.599e-06	3.21	1.969e-06	3.99	1.325e-07	4.96	2.787e-06	3.98	9.249e-08	4.61	3.817e-08	4.99
64	1.112e-06	0.52	1.523e-07	3.69	1.428e-08	3.21	1.924e-07	3.86	5.464e-08	0.76	2.920e-09	3.71
	ALG-SP with $\eta = 10^{-8}$. $k = 4, m = 5$, $\alpha = 40$, $\Delta t = 0.075/N$. Avg. # iter.: 7.6 for $N = 8$, 4.1 for $N = 16$, 3.2 for $N = 32$, and 2.8 for $N = 64$.											
8	3.703e-04	–	4.944e-04	–	1.283e-04	–	6.784e-04	–	8.026e-05	–	3.923e-05	–
16	1.411e-05	4.71	3.131e-05	3.98	4.132e-06	4.96	4.392e-05	3.95	2.259e-06	5.15	1.215e-06	5.01
32	5.148e-07	4.78	1.964e-06	4.00	1.317e-07	4.97	2.786e-06	3.98	7.680e-08	4.88	3.812e-08	4.99
64	2.207e-08	4.54	1.228e-07	4.00	4.171e-09	4.98	1.755e-07	3.99	2.445e-09	4.97	1.194e-09	5.00

where the pressure pulse on the inflow boundary Γ_{in}^f is given as follows:

$$p_{in}(t) = \begin{cases} \frac{p_{\max}}{2}\left[1 - \cos(\frac{2\pi t}{t_{\max}})\right] & \text{if } t \le t_{\max}, \\ 0 & \text{if } t > t_{\max}, \end{cases}$$

where $p_{\max} = 1.333 \times 10^4$ and $t_{\max} = 3$ millisecond (ms). Final time of the simulation is $T = 12$ ms.

We apply the three algorithms ALG-M, ALG-SP with one sub-iteration (denoted as ALG-PI1), and ALG-P with polynomial degree $k = 1$ on a structured mesh with mesh size $h = 0.1$ that consists of $2 \times (60 \times 5) = 600$ congruent triangles for the fluid domain and $2 \times (60 \times 1)$ congruent triangles for the structure domain. The time step size is taken to be $\Delta t = 10^{-1}$ ms, and the combination parameter is $\alpha = 1000$. For the temporal discretization, we use BDF2 for ALG-M and ALG-PI1, and BDF1 for ALG-P. The loosely coupled scheme ALG-P is numerically observed to be unstable with BDF2 time stepping, even when the time step size is decreased by a factor of 10. Interestingly, with only one step sub-iteration, ALG-IP1 with BDF2 time stepping produces a stable result. Figure 4 shows the flow rate (2/3 of the horizontal fluid velocity) and mean pressure at bottom line $y = 0$, and interface vertical displacement for the three schemes at times $t = 4, 8, 12$ ms. We observe that the results for the iterative partitioned scheme ALG-IP1 and the monolithic scheme ALG-M, both with BDF2 time stepping, are indistinguishable from each other, while the results for the loosely partitioned scheme ALG-P produces less accurate and more dissipative results due to a larger temporal errors from BDF1 time stepping.

5.6. Example 6: Flow past a cylinder with a flexible bar. In our last example, we test the performance of the proposed FSI solvers on the classical benchmark problem proposed by Turek and Hron [87] where reference data is available in [35].

The problem is a two-dimensional incompressbile channel flow around a rigid cylinder with an attached nonlinearly elastic bar. The domain is depicted in Figure 5.

- The domain dimensions are: length $L = 2.5$, height $H = 0.41$.

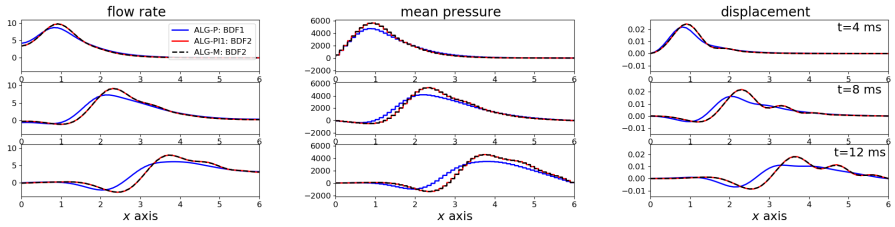

FIGURE 4. **Example 5:** Left: fluid flow rate along the bottom line. Middle: mean pressure along bottom line. Right: vertical displacement along the interface $y = 0.5$. Top row: $t = 4$ ms. Middle row: $t = 8$ ms. Bottom row: $t = 12$ ms. Polynomial degree $k = 1$. Mesh size $h = 0.1$. Time step size $\Delta t = 10^{-1} ms$.

- The circle center is positioned at $C = (0.2, 0.2)$ (measured from the left bottom corner of the channel) and the radius is $r = 0.05$.
- The elastic structure bar has length $l = 0.35$ and height $h = 0.02$, the right bottom corner is positioned at $(0.6, 0.19)$, and the left end is fully attached to the fixed cylinder.
- The control point is $A(t)$, fixed with the structure with $A(0) = (0.6, 0.2)$.

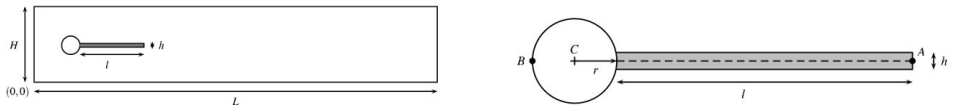

FIGURE 5. **Example 6:** The domain for the FSI problem [87].

The fluid region is governed by the Navier-Stokes equations (8) with $\boldsymbol{f}^f = 0$, and the elastic structure is governed by the equations for hyperelasticity (21) with $\boldsymbol{f}^s = 0$. The coupling conditions (32a)–(32b) are used on the fluid-structure interface Γ_t, and the following boundary conditions are used:

- A parabolic velocity profile is prescribed at the left channel inflow

$$\boldsymbol{u}^f(0, y, t) = \begin{cases} \boldsymbol{u}^f(0, y) \frac{1-\cos(\frac{\pi}{2}t)}{2} & \text{if } t < 2, \\ \boldsymbol{u}^f(0, y) & \text{otherwise,} \end{cases}$$

  where $\boldsymbol{u}^f(0, y) = 1.5\bar{U}\frac{y(H-y)}{(H/2)^2} = 61.5\bar{U}\frac{4.0}{0.1681}y(0.41 - y)$.
- The stress-free boundary condition $\boldsymbol{\sigma}^f \boldsymbol{n} = 0$ is prescribed at the outflow.
- The no-slip condition ($\boldsymbol{u}^f = 0$, or $\boldsymbol{d} = \boldsymbol{u}^s = 0$) is prescribed on all the other boundary parts.

Two test cases resulting in time periodic solutions are considered, which are denoted as FSI2 and FSI3 in [87]. The associated material parameters are listed in Table 13.

TABLE 13. **Example 6:** Parameter settings for the two test cases.

parameter	$\rho^s[10^3 \frac{\text{kg}}{\text{m}^3}]$	$\lambda^s[10^6 \frac{\text{kg}}{\text{ms}^2}]$	$\mu^s[10^6 \frac{\text{kg}}{\text{ms}^2}]$	$\rho^f[10^3 \frac{\text{kg}}{\text{m}^3}]$	$\mu^f[\frac{\text{kg}}{\text{ms}}]$	$\bar{U}[\frac{\text{m}}{\text{s}}]$
FSI2	10	2.0	0.5	1	1	1
FSI3	1	8.0	2.0	1	1	2

Quantities of interest are

- The displacement of the control point A at the end of the beam structure (see Figure 5).
- The lift and drag forces acting on the cylinder and the beam structure:

$$(F_D, F_L) = \int_S \boldsymbol{\sigma}^f \boldsymbol{n} \, \mathrm{ds},$$

  where S denotes the boundary between the fluid domain and the cylinder together with the elastic structure.

We compare the computational results with the reference data provided in [35] after a fully developed periodic flow is formed.

We apply ALG-M and ALG-SP with polynomial degree $k = 3$, BDF[2] time stepping, and a combination parameter $\alpha = 5 \times 10^4$. The stopping tolerance for ALG-SP is taken to be $\eta = 5 \times 10^{-5}$. For ALG-SP we replace the convection velocity $\boldsymbol{u}_h^{f,n}$ in the flow solver (39a) with the explicit extrapolation $\boldsymbol{u}_h^{f,n,*}$, which leads to a linear scheme for the fluid and further saves the computational cost. Two set of meshes are used in the simulation. The coarse mesh, which contains 495 triangular elements, is generated automatically from the geometry by NETGEN [77]. Curved elements with polynomial degree $k = 3$ are used for elements near the cylinder. The fine mesh is obtained from the coarse mesh by a uniform refinement; see Figure 6.

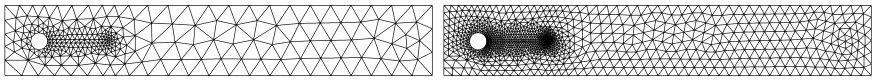

FIGURE 6. The computational meshes. Left: coarse mesh with 495 elements. Right: fine mesh with 1980 elements. Curved elements with polynomial degree 3 are used near the cylinder.

For the FSI2 problem, we use two different time step sizes, a coarse time step size $\Delta t = 4 \times 10^{-3}$ and a fine time step size $\Delta t = 2 \times 10^{-3}$, and stop the simulation at time $T = 15$. For the FSI3 problem, due to a larger fluid velocity magnitude, we use two smaller time step sizes, a coarse time step size $\Delta t = 2 \times 10^{-3}$ and a fine time step size $\Delta t = 1 \times 10^{-3}$, and stop the simulation at time $T = 10$. The average number of iterations for ALG-SP are recorded in Table 14, which are around 10 for all the cases. The nonlinear systems are solved via the Newton's method with a stopping residual tolerance of 10^{-8}, and a sparse direct solver is used for the linear system in each Newton iterations. It was observed that the average number of Newton iterations for all cases are around 4. The total run time for the partitioned scheme ALG-SP is observed to be about 2–4 times more than that for the monolithic scheme ALG-M using the same mesh and time step size.

TABLE 14. **Example 6:** Average number of iterations for ALG-SP with $k = 3$, BDF[2] time stepping, $\alpha = 5 \times 10^4$, and $\eta = 5 \times 10^{-5}$.

	Δt	coarse mesh	fine mesh
FSI2	4×10^{-3}	9.2	9.2
	2×10^{-3}	7.4	7.4
FSI3	2×10^{-3}	13.1	13.4
	1×10^{-3}	11.1	11.3

For the FSI2 problem, a fully developed periodic flow is observed starting around time $t = 10$; see Figure 7 for the quantities of interest computed on the fine mesh with the fine time step size $\Delta t = 2 \times 10^{-3}$, which also shows that ALG-M and ALG-SP with $\eta = 5 \times 10^{-5}$ produces qualitatively similar results. The results for

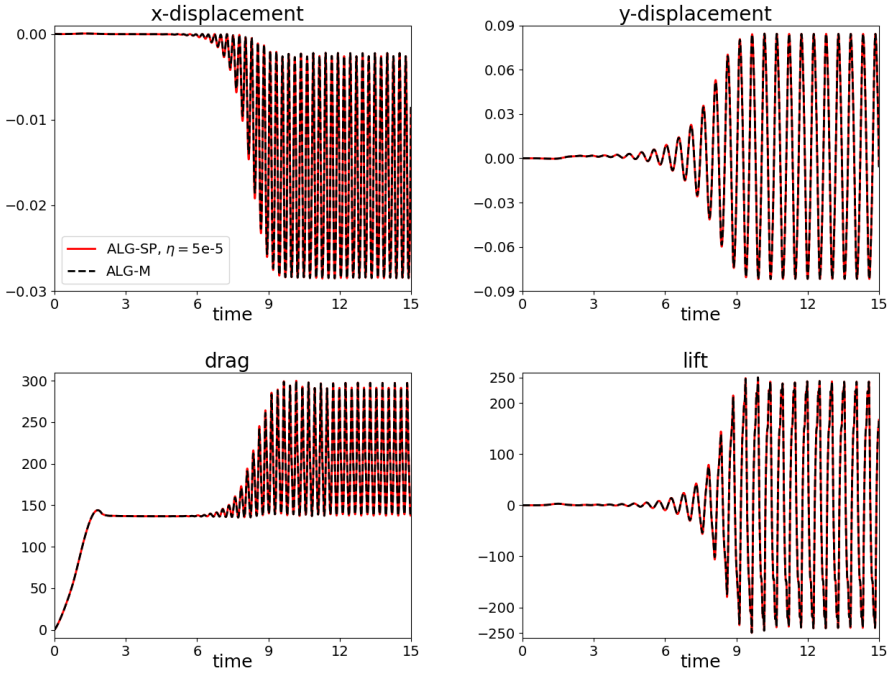

FIGURE 7. **Example 6:** Time evolution of the quantities of interest for FSI2. Discretization: ALG-M and ALG-SP with $k = 3$ and BDF[2] time stepping on the fine mesh with $\Delta t = 4 \times 10^{-3}$. Top left: x-component of displacement at point A; Top right: y-component of displacement at point A; Bottom left: drag force; Bottom right: lift force.

the fully developed flow are recorded in Table 15, which are observed to be in good match with reference data from [35]. In particular, the results on a fixed mesh for ALG-M and ALG-SP using the two different time step sizes are very close to each other.

In Figure 8, we plot the quantities of interest of the computed solution for $t \in [13.85, 14.55]$, where the flow has been fully developed, along with the reference data provided in [35]. Here we again observe that the results for ALG-M (first row) and ALG-SP (second row) are very close to each when the same discretization parameters (mesh size and time step size) are used. Moreover, we also observe a small phase error comparing with the reference data for the results on the fine mesh (blue and magenta lines), and a slightly phase shift for the results on the coarse mesh (red and green lines). Let us now briefly compare our results in Figure 8 with those in [81], which proposed the first HDG-based monolithlic FSI solver. The most accurate FSI2 result reported in [81] was shown in Figure 10 therein, which used an HDG scheme with $Q2$ elements and BDF2 time stepping on a quadrilaterial mesh with 4364 elements and 112277 global DOFs (the time step size was not

TABLE 15. **Example 6**: Results for FSI2 in the fully developed flow regime ($t \geq 10$).

ALG-M

mesh	ndof	Δt	x-disp.[A]	y-disp.[A]	drag	lift
coarse	5972	4×10^{-3}	-1.567e-2±1.351e-2	1.461e-3±8.387e-2	2.177e2±8.111e1	1.119e0±2.397e2
		2×10^{-3}	-1.566e-2±1.335e-2	1.444e-3±8.410e-2	2.201e2±8.394e1	-1.903e0±2.505e2
fine	23392	4×10^{-3}	-1.537e-2±1.328e-2	1.274e-3±8.287e-2	2.163e2±7.884e1	1.476e0±2.369e2
		2×10^{-3}	-1.536e-2±1.316e-2	1.255e-3±8.313e-2	2.184e2±8.137e1	-1.303e0±2.443e2

ALG-SP with $\eta = 5 \times 10^{-5}$

mesh	ndof	Δt	x-disp.[A]	y-disp.[A]	drag	lift
coarse	5972	4×10^{-3}	-1.572e-2±1.354e-2	1.468e-3±8.400e-2	2.179e2±8.138e1	1.154e0±2.401e2
		2×10^{-3}	-1.567e-2±1.337e-2	1.455e-3±8.414e-2	2.201e2±8.399e1	-1.876e0±2.502e2
fine	23392	4×10^{-3}	-1.542e-2±1.331e-2	1.271e-3±8.302e-2	2.166e2±7.916e1	1.424e0±2.374e2
		2×10^{-3}	-1.537e-2±1.317e-2	1.257e-3±8.317e-2	2.185e2±8.144e1	-1.121e0±2.442e2
ref[35]	76672	1×10^{-3}	-1.454e-2±1.248e-2	1.25e-3±8.07e-2	2.131e2±7.576e1	8.5e-1±2.344e2
	304128	5×10^{-4}	-1.485e-2±1.270e-2	1.30e-3±8.16e-2	2.151e2±7.765e1	6.1e-1±2.378e2

reported therein). The results in [81, Figure 10] showed a maximal amplitude error of 7% in the x-displacement and drag force, comparing with the reference data in [35]. They also reported that their results were sensitive to the stabilization parameter **S** used in the HDG discretizations. Our results on the fine mesh in Figure 8, which contains 1980 triangular elements and 23392 global DOFs, are closer to the reference data than those in [81, Figure 10] and have less than 5% error (calculated from Table 15) in the x-displacement and drag force. Hence we achieve better accuracy using less global DOFs, which is partly due to our use of higher order spatial discretization with polynomial degree $k = 3$, the divergence-free fluid velocity approximation, and a TDNNS structure solver without (sensitive) tunable HDG stabilization parameters.

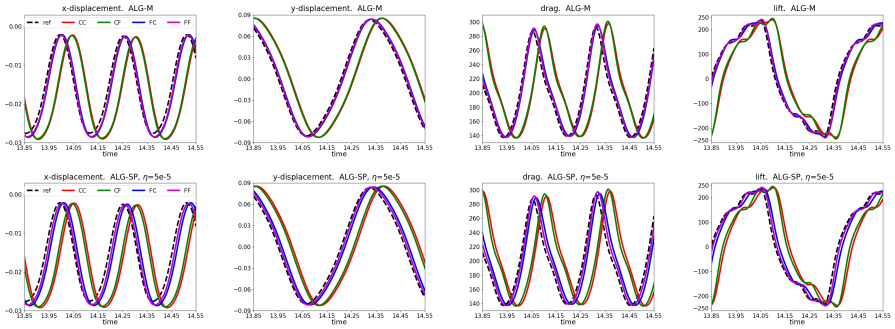

FIGURE 8. **Example 6:** The quantities of interest for FSI2 in the fully developed flow regime for $t \in [13.85, 14.55]$. CC: coarse mesh with coarse time step size, CF: coarse mesh with fine time step size, FC: fine mesh with coarse time step size, FF: fine mesh with fine time step size. Top row: ALG-M with $k = 3$ and BDF[2] time stepping. Bottom row: ALG-SP with $k = 3$, BDF[2] time stepping, and $\eta = 5 \times 10^{-5}$. Dashed black line: reference solution from [35].

For the FSI3 problem, a fully developed periodic flow is observed starting around time $t = 5$; see Figure 9 for the quantities of interest for $t \in [0, 6]$ computed on

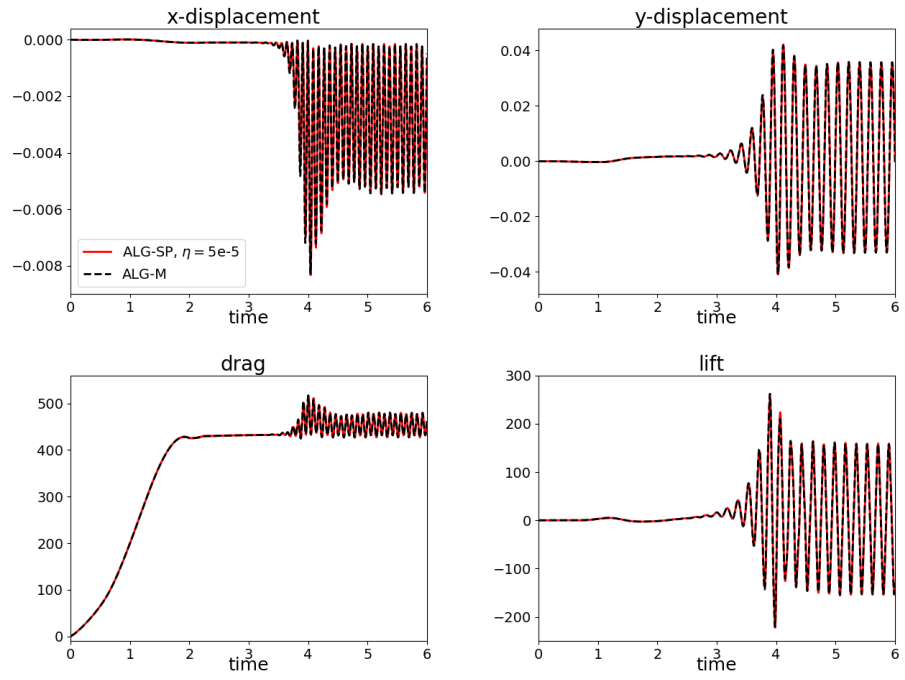

FIGURE 9. **Example 6:** Time evolution of the quantities of interest for FSI3 for $t \in [0, 6]$. Discretization: ALG-M and ALG-SP with $k = 3$ and BDF[2] time stepping on the fine mesh with $\Delta t = 2 \times 10^{-3}$. Top left: x-component of displacement at point A; Top right: y-component of displacement at point A; Bottom left: drag force; Bottom right: lift force.

the fine mesh with the fine time step size $\Delta t = 1 \times 10^{-3}$. The results for the fully developed flow are recorded in Table 16, where those on the fine mesh are observed to be in good match with reference data from [35], and those on the coarse mesh are slightly off which suggests a relative large spatial approximation errors on the coarse mesh.

In Figure 10, we plot the quantities of interest of the computed solution for $t \in [5.75, 6]$, where the flow has been fully developed, along with the reference data provided in [35]. Here, surprisingly, we observe that the phase errors for both schemes on the coarse mesh (red and green lines), comparing with the reference data, are smaller than those on the fine mesh (blue and magenta lines). This finding seems to contradict with the results in Table 16, which clearly suggest the superior of fine mesh results in terms of the amplitude and mean values. Below we give a brief explanation of this discrepancy. In Figure 11, we plot the evolution of y-component of the displacement at point A for the monolithic scheme ALG-M on the coarse and fine meshes for both FSI2 and FSI3. It is clearly observed that the results for FSI2 on coarse and fine meshes are very close to each other, and are also consistent with the reference data. However, for FSI3 on the lower panel of Figure 11, we observe a very large difference for the coarse and fine mesh solutions especially in the transition region when $3 \leq t \leq 5$. The fine mesh solution starts visible oscillation about 0.3 time unit earlier than the coarse mesh solution.

TABLE 16. **Example 6**: Results for FSI3 in the fully developed flow regime ($t \geq 5$).

ALG-M

mesh	ndof	Δt	x-disp.[A]	y-disp.[A]	drag	lift
coarse	5972	2×10^{-3}	-3.259e-3± 3.081e-3	1.296e-3± 3.745e-2	4.637e2± 3.084e1	5.510e0± 1.522e2
		1×10^{-3}	-3.247e-3± 3.071e-3	1.300e-3± 3.742e-2	4.636e2± 3.115e1	5.193e0± 1.537e2
fine	23392	2×10^{-3}	-2.792e-3± 2.640e-3	1.390e-3± 3.440e-2	4.535e2± 2.620e1	2.532e0± 1.553e2
		1×10^{-3}	-2.787e-3± 2.636e-3	1.399e-3± 3.439e-2	4.534e2± 2.649e1	2.465e0± 1.567e2

ALG-SP with $\eta = 5 \times 10^{-5}$

mesh	ndof	Δt	x-disp.[A]	y-disp.[A]	drag	lift
coarse	5972	2×10^{-3}	-3.253e-3± 3.079e-3	1.294e-3± 3.743e-2	4.635e2± 3.112e1	5.268e0± 1.540e2
		1×10^{-3}	-3.247e-3± 3.072e-3	1.300e-3± 3.742e-2	4.636e2± 3.131e1	5.201e0± 1.543e2
fine	23392	2×10^{-3}	-2.788e-3± 2.639e-3	1.402e-3± 3.438e-2	4.533e2± 2.653e1	2.499e0± 1.565e2
		1×10^{-3}	-2.792e-3± 2.641e-3	1.369e-3± 3.443e-2	4.534e2± 2.662e1	2.413e0± 1.5702
ref[35]	76672	5×10^{-4}	-2.78e-3± 2.62e-3	1.44e-3± 3.435e-2	4.591e2± 2.662e1	2.39e0± 1.507e2
	304128	2.5×10^{-4}	-2.88e-3± 2.72e-3	1.47e-3± 3.499e-2	4.605e2± 2.774e1	2.50e0± 1.539e2

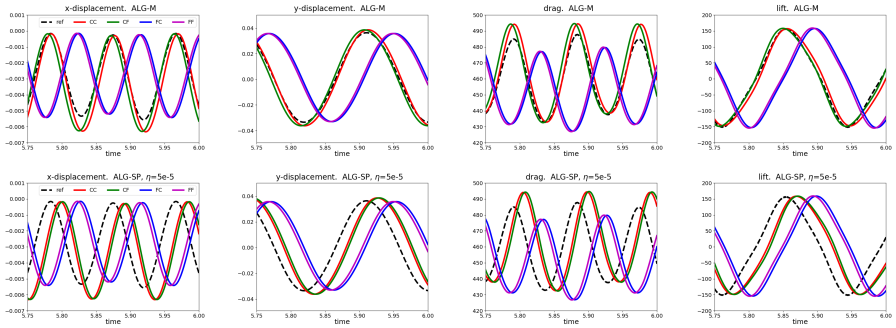

FIGURE 10. **Example 6:** The quantities of interest for FSI3 in the fully developed flow regime for $t \in [6, 6.25]$. CC: coarse mesh with coarse time step size, CF: coarse mesh with fine time step size, FC: fine mesh with coarse time step size, FF: fine mesh with fine time step size. Top row: ALG-M with $k = 3$ and BDF[2] time stepping. Bottom row: ALG-SP with $k = 3$, BDF[2] time stepping, and $\eta = 5 \times 10^{-5}$. Dashed black line: reference solution from [35].

We note that FSI3 is a very challenging test case, and there is no recorded time-accurate data that includes the transition time solution in the literature yet. The reference data provided in [35] only recorded results from time $t = 5$ to $t = 6.44$. On the other hand, since the fine mesh solution matches better with the reference data in terms of the amplitude and mean values in Figure 11 (and in Table 16), we believe our fine mesh results may be more reliable than the coarse mesh results, which is partially confirmed by an additional mesh refinement study as shown in Figure 12. In Figure 12, we present the time evolution of the y-component of the displacement at point A and the lift force on a finer mesh obtained from a uniform refinement of the fine mesh, together with those on the coarse and fine meshes. We clearly observe that the results on the fine and finer meshes are on top of each other while those on the coarse mesh is less accurate, which indicates a mesh convergence might be reached on the fine mesh. A more compressive study of FSI3 including the transition time accuracy will be investigated in our future work.

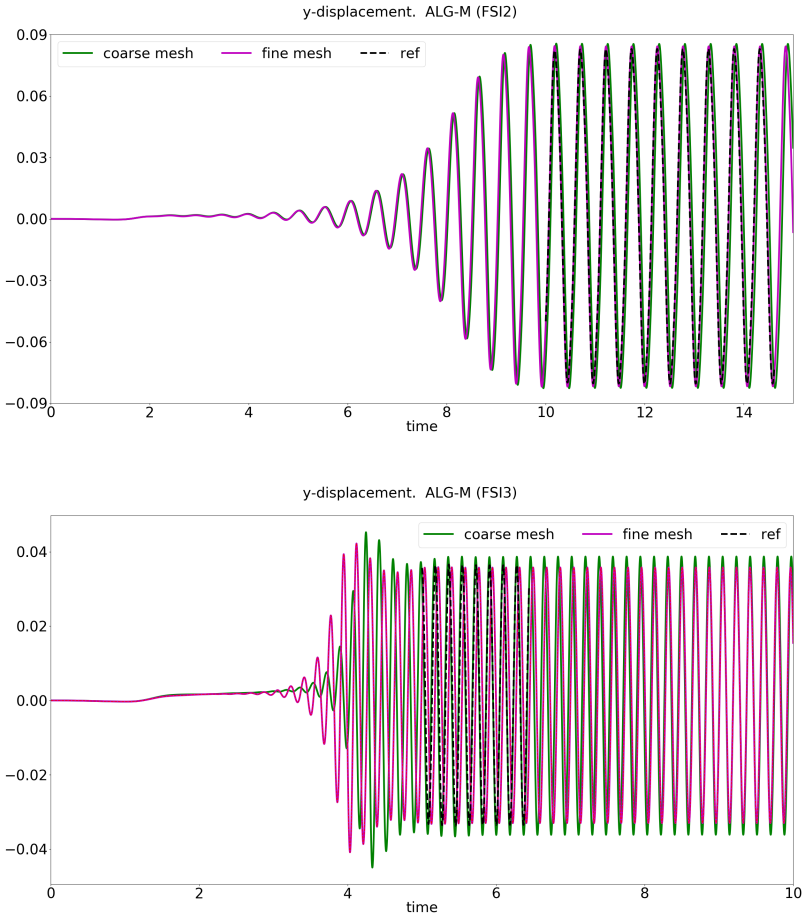

FIGURE 11. **Example 6:** Evolution of y-displacement at point A for FSI2 (top) and FSI3 (bottom). The time step size is $\Delta t = 2e{-}3$ for FSI2 and $\Delta t = 1e - 3$ for FSI3.

In conclusion, we observe that both the monolithic scheme ALG-M and the strongly coupled partitioned scheme ALG-SP produce qualitatively good results for the two benchmark tests.

6. Conclusion

We have presented high-order FSI solvers based on an ALE divergence-free HDG discretization for the fluid sub-problem, a TDNNS discretization for the structure sub-problem, and a generalized Robin interface treatment. Both monolithic and strongly coupled partitioned schemes are obtained, which are numerically verified to enjoy good stability properties. Numerical results showed that the proposed methods meet the design order of accuracy both in space and time, and also showed good performance of the methods for several two-dimensional benchmark examples.

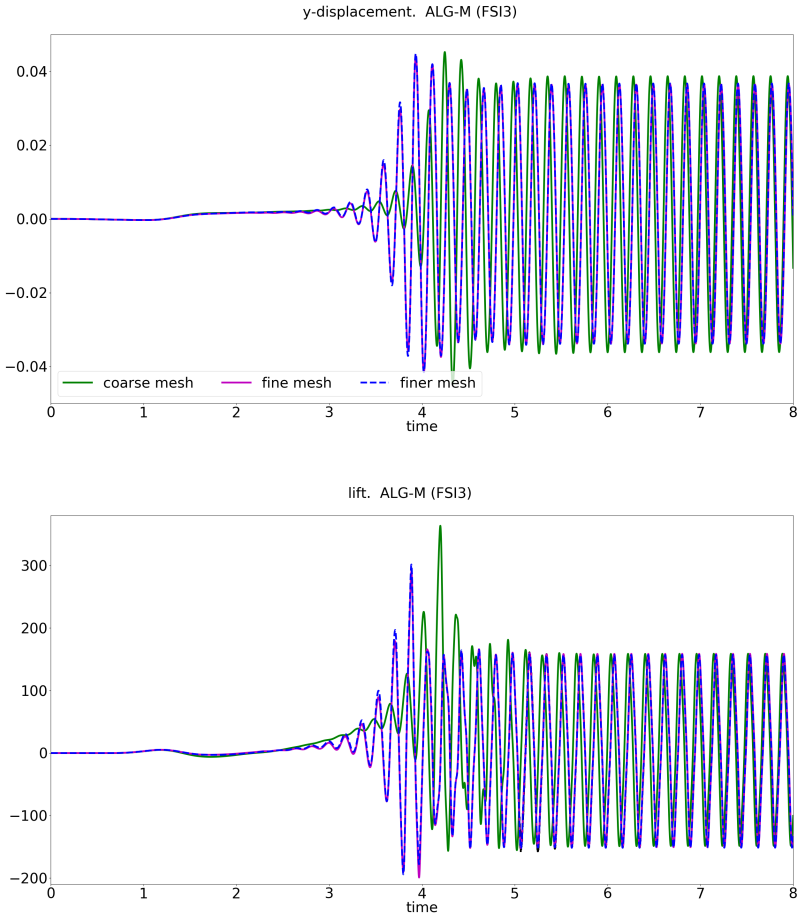

FIGURE 12. **Example 6:** Mesh refinement study for the time evolution of the y-component of displacement at point A and the lift force for FSI3. The finer mesh is obtained from the fine mesh in Figure 6 by a uniform refinement. Discretization: ALG-M with k = 3 and BDF[2] time stepping with $\Delta t = 1e-3$.

Acknowledgments

We would like to thank Martina Bukač from University of Notre Dame for helpful discussions on the generalized Robin interface treatment. We acknowledge the partial support of this work from U.S. National Science Foundation through grant DMS-2012031.

References

[1] S. BADIA, F. NOBILE, AND C. VERGARA, Robin-Robin preconditioned Krylov methods for fluid-structure interaction problems, Comput. Methods Appl. Mech. Engrg., 198 (2009), pp. 2768–2784.

[2] M. BALÁZSOVÁ, M. FEISTAUER, J. HORÁČEK, M. HADRAVA, AND A. KOSÍK, Space-time discontinuous Galerkin method for the solution of fluid-structure interaction, Appl. Math., 63 (2018), pp. 739–764.

[3] J. W. Banks, W. D. Henshaw, A. K. Kapila, and D. W. Schwendeman, An added-mass partition algorithm for fluid–structure interactions of compressible fluids and nonlinear solids, J. Comput. Phys., 305 (2016), pp. 1037–1064.
[4] J. W. Banks, W. D. Henshaw, and D. W. Schwendeman, An analysis of a new stable partitioned algorithm for FSI problems. Part I: Incompressible flow and elastic solids, J. Comput. Phys., 269 (2014), pp. 108–137.
[5] Y. Bazilevs, V. M. Calo, Y. Zhang, and T. J. R. Hughes, Isogeometric fluid-structure interaction analysis with applications to arterial blood flow, Comput. Mech., 38 (2006), pp. 310–322. 13th International Conference on Finite Elements for Flow Problems, Swansea, WALES, APR 04-06, 2005.
[6] Y. Bazilevs, K. Takizawa, and T. E. Tezduyar, Computational Fluid–Structure Interaction: Methods and Applications, Wiley, 2013.
[7] D. Boffi, F. Brezzi, and M. Fortin, Mixed finite element methods and applications, vol. 44 of Springer Series in Computational Mathematics, Springer, Heidelberg, 2013.
[8] M. Bukač, A. Seboldt, and C. Trenchea, Refactorization of Cauchy's method: a second-order partitioned method for fluid-thick structure interaction problems, J. Math. Fluid Mech., 23 (2021), pp. Paper No. 64, 25.
[9] M. Bukač, S. Čanić, R. Glowinski, B. Muha, and A. Quaini, A modular, operator-splitting scheme for fluid-structure interaction problems with thick structures, Internat. J. Numer. Methods Fluids, 74 (2014), pp. 577–604.
[10] M. Bukač, S. Čanić, R. Glowinski, J. Tambača, and A. Quaini, Fluid-structure interaction in blood flow capturing non-zero longitudinal structure displacement, J. Comput. Phys., 235 (2013), pp. 515–541.
[11] H.-J. Bungartz and M. Schäfer, eds., Fluid Structure Interaction: Modelling, Simulation, Optimization, Lecture Notes in Computational Science and Engineering, Vol. 53, Springer, 2006.
[12] M. M. S. M. Bungartz, H.-J., ed., Fluid Structure Interaction II: Modelling, Simulation, Optimization, Lecture Notes in Computational Science and Engineering, Vol. 73, Springer, 2010.
[13] E. Burman, R. Durst, M. A. Fernández, and J. Guzmán, Fully discrete loosely coupled Robin-Robin scheme for incompressible fluid-structure interaction: stability and error analysis , arXiv:2007.03846 [math.NA].
[14] E. Burman and M. A. Fernández, Stabilization of explicit coupling in fluid-structure interaction involving fluid incompressibility, Comput. Methods Appl. Mech. Engrg., 198 (2009), pp. 766–784.
[15] E. Burman and M. A. Fernández, Explicit strategies for incompressible fluid-structure interaction problems: Nitsche type mortaring versus Robin-Robin coupling, Internat. J. Numer. Methods Engrg., 97 (2014), pp. 739–758.
[16] H. Casquero, Y. J. Zhang, C. Bona-Casas, L. Dalcin, and H. Gomez, Non-body-fitted fluid-structure interaction: divergence-conforming B-splines, fully-implicit dynamics, and variational formulation, J. Comput. Phys., 374 (2018), pp. 625–653.
[17] P. Causin, J. Gerbeau, and F. Nobile, Added-mass effect in the design of partitioned algorithms for fluid-structure problems, Comput. Methods Appl. Mech. Engrg., 194 (2005), pp. 4506–4527.
[18] S. K. Chakrabarti, Numerical models in fluid-structure interaction, WIT, 2005.
[19] J. Chessa and T. Belytschko, An extended finite element method for two-phase fluids, Trans. ASME J. Appl. Mech., 70 (2003), pp. 10–17.
[20] B. Cockburn, Static condensation, hybridization, and the devising of the HDG methods, in Building bridges: connections and challenges in modern approaches to numerical partial differential equations, vol. 114 of Lect. Notes Comput. Sci. Eng., Springer, [Cham], 2016, pp. 129–177.
[21] ———, Discontinuous Galerkin Methods for Computational Fluid Dynamics, in Encyclopedia of Computational Mechanics Second Edition, Part 1 Fluids, E. Stein, R. De Borst, and T. J. R. Hughes, eds., John Wiley & Sons, 2018.
[22] B. Cockburn and G. Fu, Devising superconvergent HDG methods with symmetric approximate stresses for linear elasticity by M-decompositions, IMA J. Numer. Anal., 38 (2018), pp. 566–604.
[23] B. Cockburn, G. Fu, and W. Qiu, A note on the devising of superconvergent HDG methods for Stokes flow by M-decompositions, IMA J. Numer. Anal., 37 (2017), pp. 730–749.

[24] B. Cockburn, G. Fu, and F. J. Sayas, Superconvergence by M-decompositions. Part I: General theory for HDG methods for diffusion, Math. Comp., 86 (2017), pp. 1609–1641.
[25] B. Cockburn, J. Gopalakrishnan, and R. Lazarov, Unified hybridization of discontinuous Galerkin, mixed and continuous Galerkin methods for second order elliptic problems, SIAM J. Numer. Anal., 47 (2009), pp. 1319–1365.
[26] B. Cockburn, G. Kanschat, and D. Schötzau, A note on discontinuous Galerkin divergence-free solutions of the Navier-Stokes equations, J. Sci. Comput., 31 (2007), pp. 61–73.
[27] B. Cockburn, G. E. Karniadakis, and C.-W. Shu, eds., Discontinuous Galerkin methods: Theory, computation and applications, Lecture Notes in Computational Science and Engineering, 11. Springer-Verlag, Berlin, 2000.
[28] B. Cockburn and F.-J. Sayas, Divergence-conforming HDG methods for Stokes flows, Math. Comp., 83 (2014), pp. 1571–1598.
[29] B. Cockburn and C.-W. Shu, Runge-Kutta discontinuous Galerkin methods for convection-dominated problems, J. Sci. Comput., 16 (2001), pp. 173–261.
[30] J. Degroote, P. Bruggeman, R. Haelterman, and J. Vierendeels, Stability of a coupling technique for partitioned solvers in FSI applications, Comput. & Struct., 86 (2008), pp. 2224–2234.
[31] J. Donea, A. Huerta, J.-P. Ponthot, and A. Rodriguez-Ferran, Arbitrary Lagrangian-Eulerian Methods, in Encyclopedia of Computational Mechanics, Volume 1: Fundamentals, chapter 14, E. Stein, R. De Borst, and T. J. R. Hughes, eds., John Wiley & Sons, 2004.
[32] E. H. Dowell and K. C. Hall, Modeling of fluid-structure interaction, Annual review of fluid mechanics, 33 (2001), pp. 445–490.
[33] E. Emmrich, Stability and error of the variable two-step BDF for semilinear parabolic problems, J. Appl. Math. Comput., 19 (2005), pp. 33–55.
[34] C. Farhat, K. G. van der Zee, and P. Geuzaine, Provably second-order time-accurate loosely-coupled solution algorithms for transient nonlinear computational aeroelasticity, Comput. Methods Appl. Mech. Engrg., 195 (2006), pp. 1973–2001.
[35] FEATFLOW, Finite element software for the incompressible navier-stokes equations, www.featflow.de.
[36] N. Fehn, J. Heinz, W. Wall, and M. Kronbichler, High-order arbitrary Lagrangian–Eulerian discontinuous Galerkin methods for the incompressible Navier–Stokes equations , J Comput. Phys., 430 (2021), p. 110040.
[37] M. Feistauer, J. Hasnedlová-Prokopová, J. Horáček, A. Kosík, and V. Kučera, DGFEM for dynamical systems describing interaction of compressible fluid and structures, J. Comput. Appl. Math., 254 (2013), pp. 17–30.
[38] M. Feistauer, V. Kučera, and J. Prokopová, Discontinuous Galerkin solution of compressible flow in time-dependent domains, Math. Comput. Simulation, 80 (2010), pp. 1612–1623.
[39] M. A. Fernández, Incremental displacement-correction schemes for incompressible fluid-structure interaction: stability and convergence analysis, Numer. Math., 123 (2012), pp. 210–65.
[40] A. Figueroa, I. Vignon-Clementel, K. Jansen, T. Hughes, and C. Taylor, A coupled momentum method for modeling blood flow in three-dimensional deformable arteries, Comput. Methods Appl. Mech. Engrg., 195 (2006), pp. 5685–5706.
[41] T.-P. Fries and T. Belytschko, The extended/generalized finite element method: an overview of the method and its applications, Internat. J. Numer. Methods Engrg., 84 (2010), pp. 253–304.
[42] B. Froehle and P.-O. Persson, A high-order discontinuous Galerkin method for fluid-structure interaction with efficient implicit-explicit time stepping, J. Comput. Phys., 272 (2014), pp. 455–470.
[43] G. Fu, Arbitrary Lagrangian–Eulerian hybridizable discontinuous Galerkin methods for incompressible flow with moving boundaries and interfaces, Comput. Methods Appl. Mech. Engrg., 367 (2020), p. 113158.
[44] G. Fu, B. Cockburn, and H. Stolarski, Analysis of an HDG method for linear elasticity, Internat. J. Numer. Methods Engrg., 102 (2015), pp. 551–575.
[45] G. Fu, Y. Jin, and W. Qiu, Parameter-free superconvergent $H(\mathrm{div})$-conforming HDG methods for the Brinkman equations, IMA J. Numer. Anal., 39 (2019), pp. 957–982.

[46] R. Glowinski, T. W. Pan, T. I. Hesla, D. D. Joseph, and J. Périaux, A fictitious domain approach to the direct numerical simulation of incompressible viscous flow past moving rigid bodies: application to particulate flow, J. Comput. Phys., 169 (2001), pp. 363–426.
[47] E. Hairer and G. Wanner, Solving ordinary differential equations. II, vol. 14 of Springer Series in Computational Mathematics, Springer-Verlag, Berlin, 2010.
[48] G. Hou, J. Wang, and A. Layton, Numerical methods for fluid-structure interaction—a review, Communications in Computational Physics, 12 (2012), pp. 337–377.
[49] J. Hron and S. Turek, A monolithic FEM/multigrid solver for an ALE formulation of fluid-structure interaction with applications in biomechanics, in Fluid-structure interaction, vol. 53 of Lect. Notes Comput. Sci. Eng., Springer, Berlin, 2006, pp. 146–170.
[50] T. J. R. Hughes, W. K. Liu, and T. K. Zimmermann, Lagrangian-Eulerian finite element formulation for incompressible viscous flows, Comput. Methods Appl. Mech. Engrg., 29 (1981), pp. 329–349.
[51] V. John, A. Linke, C. Merdon, M. Neilan, and L. G. Rebholz, On the divergence constraint in mixed finite element methods for incompressible flows, SIAM Rev., 59 (2017), pp. 492–544.
[52] D. Kamensky, M.-C. Hsu, Y. Yu, J. A. Evans, M. S. Sacks, and T. J. R. Hughes, Immersogeometric cardiovascular fluid-structure interaction analysis with divergence-conforming B-splines, Comput. Methods Appl. Mech. Engrg., 314 (2017), pp. 408–472.
[53] R. Kirby, S. Sherwin, and B. Cockburn, To CG or to HDG: a comparative study, J. Sci. Comput., 51 (2012), pp. 183–212.
[54] A. Kosík, M. Feistauer, M. Hadrava, and J. Horáček, Numerical simulation of the interaction between a nonlinear elastic structure and compressible flow by the discontinuous Galerkin method, Appl. Math. Comput., 267 (2015), pp. 382–396.
[55] A. La Spina, M. Kronbichler, M. Giacomini, W. A. Wall, and A. Huerta, A weakly compressible hybridizable discontinuous Galerkin formulation for fluid-structure interaction problems, Comput. Methods Appl. Mech. Engrg., 372 (2020), pp. 113392, 36.
[56] C. Lehrenfeld and J. Schöberl, High order exactly divergence-free hybrid discontinuous Galerkin methods for unsteady incompressible flows, Comput. Methods Appl. Mech. Engrg., 307 (2016), pp. 339–361.
[57] Z. Li, The immersed interface method using a finite element formulation, Appl. Numer. Math., 27 (1998), pp. 253–267.
[58] I. Lomtev, R. M. Kirby, and G. E. Karniadakis, A discontinuous Galerkin ALE method for compressible viscous flows in moving domains, J. Comput. Phys., 155 (1999), pp. 128–159.
[59] A. Masud and T. J. R. Hughes, A space-time Galerkin/least-squares finite element formulation of the Navier-Stokes equations for moving domain problems, Comput. Methods Appl. Mech. Engrg., 146 (1997), pp. 91–126.
[60] R. Mittal and G. Iaccarino, Immersed boundary methods, Annu. Rev. Fluid Mech., 37 (2005), pp. 239–261.
[61] M. Neunteufel, Advanced Numerical Methods for Fluid Structure Interaction. Diploma Thesis, TU Wien, 2017.
[62] M. Neunteufel, A. S. Pechstein, and J. Schöberl, Three-field mixed finite element methods for nonlinear elasticity, Comput. Methods Appl. Mech. Engrg., 382 (2021), pp. Paper No. 113857, 26.
[63] M. Neunteufel and J. Schöberl, Fluid-structure interaction with h(div)-conforming finite elements, Computers & Structures, 243 (2021), p. 106402.
[64] N. C. Nguyen and J. Peraire, Hybridizable discontinuous Galerkin methods for partial differential equations in continuum mechanics, J. Comput. Phys., 231 (2012), pp. 5955–5988.
[65] F. Nobile, Numerical approximation of fluid-structure interaction problems with application to haemodynamics, PhD thesis, École polytechnique fédérale de Lausanne, 2001.
[66] F. Nobile and C. Vergara, An effective fluid-structure interaction formulation for vascular dynamics by generalized Robin conditions, SIAM J. Sci. Comput., 30 (2008), pp. 731–763.
[67] A. Pechstein and J. Schöberl, Tangential-displacement and normal-normal-stress continuous mixed finite elements for elasticity, Math. Models Methods Appl. Sci., 21 (2011), pp. 1761–1782.
[68] ———, Anisotropic mixed finite elements for elasticity, Internat. J. Numer. Methods Engrg., 90 (2012), pp. 196–217.
[69] A. S. Pechstein and J. Schöberl, An analysis of the TDNNS method using natural norms, Numer. Math., 139 (2018), pp. 93–120.

[70] P.-O. Persson, J. Bonet, and J. Peraire, Discontinuous Galerkin solution of the Navier–Stokes equations on deformable domains , Comput. Methods Appl. Mech. Engrg., 198 (17-20) (1585–1595).
[71] P.-O. Persson, J. Peraire, and J. Bonet, A high order discontinuous galerkin method for fluid-structure interaction, in: 18th AIAA Computational Fluid Dynamics Conference, Miami, Florida, 2007, AIAA-2007-4327.
[72] C. S. Peskin, The immersed boundary method, Acta Numer., 11 (2002), pp. 479–517.
[73] O. Pironneau, Numerical study of a monolithic fluid-structure formulation, in Variational analysis and aerospace engineering, vol. 116 of Springer Optim. Appl., Springer, Cham, 2016, pp. 401–420.
[74] W. Qiu, J. Shen, and K. Shi, An HDG method for linear elasticity with strong symmetric stresses, Math. Comp., 87 (2018), pp. 69–93.
[75] A. Quaini, Algorithms for Fluid-Structure Interaction Problems Arising in Hemodynamics, PhD thesis, École polytechnique fédérale de Lausanne, 2009.
[76] T. Richter, Fluid-structure interactions: models, analysis and finite elements, vol. 118, Springer, 2017.
[77] J. Schöberl, NETGEN An advancing front 2D/3D-mesh generator based on abstract rules, Comput Visual Sci, 1 (1997), pp. 41–52.
[78] J. Schöberl, C++11 Implementation of Finite Elements in NGSolve, 2014. ASC Report 30/2014, Institute for Analysis and Scientific Computing, Vienna University of Technology.
[79] A. Seboldt and M. Bukač, A non-iterative domain decomposition method for the interaction between a fluid and a thick structure, Numer. Methods Partial Differential Equations, 37 (2021), pp. 2803–2832.
[80] A. Shamanskiy and B. Simeon, Mesh moving techniques in fluid-structure interaction: robustness, accumulated distortion and computational efficiency, Computational Mechanics, 67 (2021), pp. 583–600.
[81] J. Sheldon, S. Miller, and J. Pitt, A hybridizable discontinuous Galerkin method for modeling fluid-structure interaction, J. Comput. Phys., 326 (2016), pp. 91–114.
[82] ———, An improved formulation for hybridizable discontinuous Galerkin fluid-structure interaction modeling with reduced computational expense, Commun. Comput. Phys., 24 (2018), pp. 1279–1299.
[83] A. Sinwel, A new family of mixed finite elements for elasticity, 2009. Ph.D. thesis, Johannes Kepler University Linz.
[84] K. Sze, X. Liu, and S. Lo, Popular benchmark problems for geometric nonlinear analysis of shells , Finite Elem. Anal. Des., 40 (11) (2004), p. 1551–1569.
[85] T. E. Tezduyar, M. Behr, and J. Liou, A new strategy for finite element computations involving moving boundaries and interfaces—the deforming-spatial-domain/space-time procedure. I. The concept and the preliminary numerical tests, Comput. Methods Appl. Mech. Engrg., 94 (1992), pp. 339–351.
[86] T. E. Tezduyar, K. Takizawa, and Y. Bazilevs, Fluid-Structure Interaction and Flows with Moving Boundaries and Interfaces, in Encyclopedia of Computational Mechanics Second Edition, Part 2 Fluids, E. Stein, R. De Borst, and T. J. R. Hughes, eds., John Wiley & Sons, 2018.
[87] S. Turek and J. Hron, Proposal for numerical benchmarking of fluid-structure interaction between an elastic object and laminar incompressible flow, in Fluid-structure interaction, vol. 53 of Lect. Notes Comput. Sci. Eng., Springer, Berlin, 2006, pp. 371–385.
[88] K. Ulrich and W. Wall, Fixed-point fluid–structure interaction solvers with dynamic relaxation, Comput. Mech., 43 (2008), pp. 61–72.
[89] J. J. W. van der Vegt and J. J. Sudirham, A space-time discontinuous Galerkin method for the time-dependent Oseen equations, Appl. Numer. Math., 58 (2008), pp. 1892–1917.
[90] Y. Wang, A. Quaini, and S. Čanić, A higher-order discontinuous Galerkin/arbitrary Lagrangian Eulerian partitioned approach to solving fluid-structure interaction problems with incompressible, viscous fluids and elastic structures, J. Sci. Comput., 76 (2018), pp. 481–520.
[91] K. Washizu, Variational methods in elasticity and plasticity, Pergamon Press, Oxford-New York-Toronto, Ont., second ed., 1975. With a foreword by R. L. Bisplinghoff, International Series of Monographs in Aeronautics and Astronautics, Division I: Solid and Structural Mechanics, Vol. 9.
[92] T. Wick, Fluid-structure interactions using different mesh motion techniques, Comput. Struct., 89 (2011), pp. 1456–1467.

[93] S. Yakovlev, D. Moxey, R. Kirby, and S. Sherwin, To CG or to HDG: a comparative study in 3D, J. Sci. Comput., 67 (2016), pp. 192–220.
[94] L. Zhang, A. Gerstenberger, X. Wang, and W. K. Liu, Immersed finite element method, Comput. Methods Appl. Mech. Engrg., 193 (2004), pp. 2051–2067.
[95] S. Zhao, X. Xu, and M. Collins, The numerical analysis of fluid-solid interactions for blood flow in arterial structures - Part 2: development of coupled fluid-solid algorithms, Proceedings of the Institution of Mechanical Engineers, Part H: Journal of Engineering in Medicine, 212 (1998), pp. 241–252.

Department of Applied and Computational Mathematics and Statistics, University of Notre Dame, USA.
E-mail: gfu@nd.edu